Surface Instabilities for Adhesion Control

Item Type	dissertation
Authors	Davis, Chelsea Simone
DOI	10.7275/61vg-ge23
Download date	2024-11-23 11:44:33
Link to Item	https://hdl.handle.net/20.500.14394/38993

SURFACE INSTABILITIES FOR ADHESION CONTROL

A Dissertation Presented

by

CHELSEA SIMONE DAVIS

Submitted to the Graduate School of the
University of Massachusetts Amherst in partial fulfillment
of the requirements for the degree of

DOCTOR OF PHILOSOPHY

May 2012

Polymer Science and Engineering

SURFFACE INSTABILITIES FOR
ADHESION CONTROL

A Dissertation Presented

by

CHELSEA SIMONE DAVIS

Approved as to style and content by:

_____

Alfred J. Crosby, Chair

_____

Ryan C. Hayward, Member

_____

Ashwin Ramasubramaniam, Member

_____

David A. Hoagland, Department Head

Polymer Science and Engineering

For Mom, my rock

ACKNOWLEDGEMENTS

deeply into the fundamental phenomena behind my results and analysis. This thesis has more depth as a result of Ryan's inquisitive nature. Ashwin has brought fresh ideas and comments to my thesis. Through the eyes of a theorist, he has viewed my work in a different light and forced me to explain my results and conclusions more clearly and precisely. As committee members, both Ashwin and Ryan have that rare ability to ask really "simple" questions that, when unpacked, drive right to the central part of the problem. I admire and respect you both as brilliant scientists and hope to follow in your footsteps.

I have loved being a member of the Crosby Research Group. Graduate school has definitely been more fruitful and more fun because of the group members, past and present, that have made attending meetings and going to lab enjoyable and productive. I want to acknowledge all of the group members that came before me: Jong-Young, Edwin, CJ, Jess, Doug, and Derek. These guys taught me how to use just about every piece of equipment in lab and how to "do" grad school. Doug and Edwin were incredible mentors when I first joined the group and Derek and Jess were ready and willing to take a coffee break whenever I needed to get out of Conte.

Thanks to the present group members: Yuri, Sam, Jun, Hyun-Suk, Mike, Cheol, Sami, Yujie, Marcos, Jon, Dan, and Yu-Cheng. You guys have put up with my cranky "old grad student" self since I was a third year and I appreciate your tolerance. I especially want to thank Yuri and Mike for their insight and willingness to drop everything and discuss my research whenever I asked. You guys have been great friends and I will keep in touch with you, no matter where we end up. I have also learned from the postdocs that have passed through Al's group: Kyriaki, Santanu, Guillaume, Andrew,

Dinesh, Aline, and Dong Yun. I look forward to continuing all of the relationships, both professionally and socially, that I have formed here in the Crosby group.

My PSE classmates and friends have kept me sane. Ian, Joe, Felicia, Shilpi, JP, Sinan, Jeff, and Rachel have been great friends, coworkers, and colleagues and I thank you all for your help and support throughout grad school. Jess and Rach are tied for best roommate ever. We have shared a lot of fun memories on Summer Street like Desperate Housewife dinners, cookie parties, pumpkin carving, and cookouts. I also have to acknowledge the PSE softball teams: the Spare Parts and the Valley Radicals. Summers in Amherst were a lot more fun thanks to un-umpired, co-ed, beer-league softball.

Reaching out to the community and teaching the public about polymers has been a passion of mine throughout grad school. Greg Dabkowski has allowed me to participate in all aspects of PSE Outreach. Sabra Dickson has helped me figure out how to manage groups of crazy high school students. Both Greg and Sabra have encouraged me to participate in outreach and as an ambassador for science. I thank you both very much for the time that you have taken to share your knowledge with me.

During my graduate career, I have had the opportunity to travel abroad several times. I want to thank Professor Kilwon Cho and his research group (especially Dong Yun and Yun Joo) for the amazing research experience I had at POSTECH in Pohong, Korea. I also want to acknowledge my collaborators, Professor Costantino Creton, Professor Anke Lindner, and David Martina at ESPCI in Paris, France with whom I will be working next as a postdoc.

Financial support for this project has come from several centers and programs sponsored by the National Science Foundation. I acknowledge the NSF-IGERT

in me has never wavered and I can't express my gratitude to you. This thesis is dedicated

to you.

ABSTRACT

SURFACE INSTABILITIES FOR ADHESION CONTROL

MAY 2012

CHELSEA SIMONE DAVIS, B.S., NORTH CAROLINA STATE UNIVERSITY

M.S., UNIVERSITY OF MASSACHUSETTS AMHERST

Ph.D., UNIVERSITY OF MASSACHUSETTS AMHERST

Directed by: Professor Alfred J. Crosby

Controlling the specific adhesive properties of surfaces is a technologically complex challenge that has piqued the interest of many research groups around the world. While many scientists have used complex topographic and chemically altered surfaces to tune adhesion, others have shown that naturally occurring phenomena, such as elastic instabilities, can impact adhesion. We provide a thorough investigation into the effects of periodic surface buckling instabilities, or wrinkles, on adhesion. Wrinkles are an attractive surface patterning alternative as they form spontaneously over large areas and their dimensions, namely wavelength and amplitude, can be controlled on length scales relevant for adhesion control. We focus on the development of fundamental relationships that relate wrinkle adhesion to materials properties and topographic feature geometry. To accomplish this goal, we first investigate the separation of a flat rigid punch from a single elastic cylinder, which models the separation of a single wrinkle. The knowledge gained from this study is then utilized to develop a scaling expression relating adherence force to wrinkle geometry, materials properties, and testing geometry. This scaling theory is validated by varying these parameters systematically in a series of model wrinkle adhesion experiments. Added complexity in the form of varied crosslinker density, which alters the ratio of storage to loss moduli, and geometric confinement effects on wrinkle

adhesion are then studied. Finally, a novel technique for fabricating biaxial wrinkles with two independently-adjusted wavelengths is developed, adding an additional parameter which can be tuned to further control adhesion.

A single elastic cylinder was probed with a finite rigid flat probe, allowing the separation mechanism of a single "macro" scale wrinkle to be determined. Rather than a long cylinder contact mechanism, which has been utilized in describing wrinkle adhesion mechanisms in the past, an elliptical contact area approximation was found to more appropriately describe the single cylinder adhesion data.

To consider the impact of an array of cylinders on adhesion, a model wrinkle system comprised of an elastomeric foundation and chemically-simple polymer film was developed. The wrinkle wavelength, amplitude, substrate modulus, and probe radius were varied, and the normal adhesive response of each aligned wrinkled surface was determined. Overall, wrinkles were found to decrease the separation force relative to a smooth surface and the separation force varied inversely with the square root of a wrinkle dimension, either wavelength or amplitude.

The effects of viscoelasticity on the adhesion of a wrinkled substrate that is geometrically confined was studied. Wrinkled surface features were molded onto the surface of a rigid cylindrical probe, and the normal adhesion of these probes contacting thin elastomeric films fabricated with varying crosslinker concentrations was measured. The materials-defined length scale relating adhesion energy and modulus controlled the wrinkle feature sizes that impacted the adhesive response of each smooth film. In the most highly crosslinked films, small wrinkles increased both the separation force and

adhesion energy of the interface two-fold, while large wrinkles reduced adhesion to almost nothing.

Capitalizing on knowledge gained in the fabrication of many wrinkled surfaces, a novel technique for fabricating biaxial wrinkles was developed. Aligned wrinkles were formed on a partially crosslinked substrate, the modulus of the substrate was increased by allowing the material to crosslink completely, and a mechanical compressive strain was then imposed orthogonal to the primary wrinkle direction. This process resulted in the formation of biaxial wrinkled surfaces with two distinct, independently controlled lateral dimensions or wavelengths.

The results obtained through these experiments form a knowledge base from which precisely-controlled adhesive surfaces can be designed. The fundamental mechanics governing the adhesion of wrinkled surfaces are presented here.

TABLE OF CONTENTS

LIST OF TABLES

LIST OF FIGURES

LIST OF SYMBOLS

a ~ half contact width or radius

a_c ~ critical half contact width or radius

a_c^{JKR} ~ critical half contact radius of sphere

a_e ~ effective half contact width or radius

A ~ contact area

A_c ~ critical contact area

b ~ amplitude

c ~ probe radius

δ ~ vertical displacement

ϵ ~ strain

$\bar{E}_i$ ~ plane strain modulus of *ith* material

E_i' ~ storage modulus of *ith* material

E_i'' ~ loss modulus of *ith* material

E_i^* ~ complex modulus of *ith* material

E_f ~ film Young's modulus

E_s ~ substrate Young's modulus

γ ~ surface tension

G_c ~ critical strain energy release rate

G ~ strain energy release rate

h ~ substrate thickness

K ~ stiffness

K_I ~ stress intensity factor

λ ~ wavelength

l_{avg} ~ average feature length

l_i ~ individual length of *ith* feature

l_o ~ initial length

M_n ~ number average molecular weight

ν_i ~ Poisson's ratio of *ith* material

n ~ number of surface features contacting probe

$P \sim$ normal force at interface

$P' \sim$ Hertzian normal force at interface

$P_i \sim$ normal force at interface upon initial contact

$\bar{P}_c^{cyl} \sim$ maximum separation force per unit length of cylinder

$P_f \sim$ maximum separation force of flat surface

$\bar{P}_i \sim$ maximum separation force per unit length of single feature

$P_m \sim$ maximum compression force

$P_c \sim$ maximum separation force

$P_c^{ell} \sim$ maximum separation force of elliptical contact

$R_e \sim$ effective radius of curvature

$R_i \sim$ radius of curvature of *ith* object

$T \sim$ temperature

$t \sim$ film thickness

$\theta \sim$ angle

$U \sim$ energy

$U_b \sim$ bending energy

$U_s \sim$ stretching energy

$U_t \sim$ total energy

$U_{t,\lambda} \sim$ total wrinkle energy

$U_{t,c} \sim$ compression energy

$U_{adh} \sim$ adhesion energy

$V \sim$ velocity or displacement rate

$\omega \sim$ angular frequency

$w_{adh} \sim$ work of adhesion

CHAPTER 1

INTRODUCTION AND BACKGROUND

1.1 Project Motivation

Researchers have observed that a common pest insect, the coddling moth, has a unique evolutionary characteristic that allows it to control its adhesion to plant surfaces.[1] Each of the coddling moth's legs end in an inflatable pad covered in ridges or wrinkles. By controlling the pressure inside these pads, the moth alters the geometry of the wrinkles and underlying material properties of its feet, drastically affecting its ability to adhere.
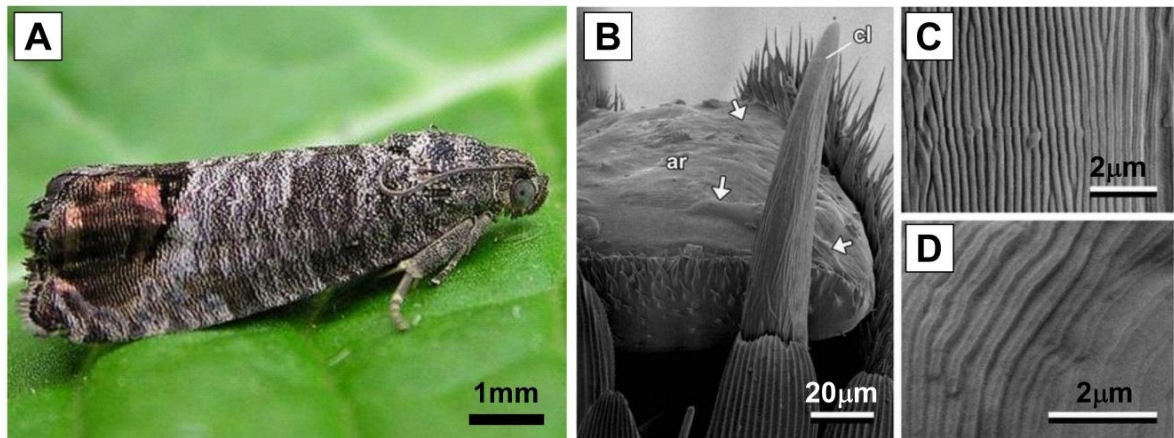
Figure 1.1: Coddling moth. (A) Coddling moth on an apple leaf. (B) SEM of the tip of the leg of a coddling moth showing a fully inflated foot pad or arolium ("ar").[1] Ridges on arolium surface when deflated (C) and inflated (D) demonstrating change in geometry of surface features. Used with permission: J. Insect Phys. 2009.

The common earwig is another insect that takes advantage of wrinkles to control adhesion.[2] This bug has an array of tiny hairs or spatulae covering the tips of its feet. One side of each spatula is unpatterned and enhances the adhesion of the insect to surfaces, while the back side of each feature is covered with ridges or wrinkles that prevent the pads of the spatulae from sticking to one another.

Even in our own fingerprints, the effects of wrinkles on adhesion can be observed. Fingerprints are a result of the differential growth between the dermis and basal layers of our skin during development in utero.[3] The ridges of fingerprints affect the frictional adhesion of our grip, changing how humans grasp smooth objects.[4] It has been shown
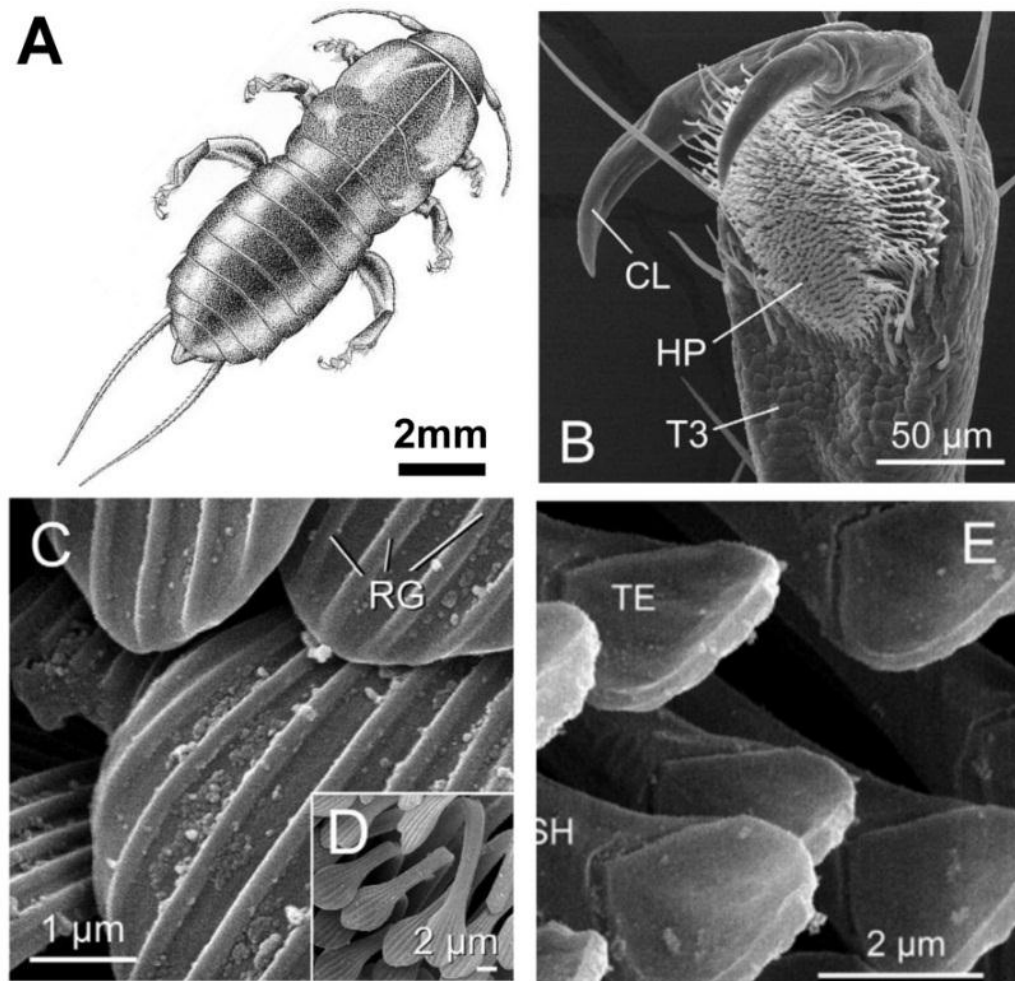
Figure 1.2: Earwig. (A) Schematic representation of an earwig. (B) Scanning electron micrograph of the leg of an earwig. Spatulae on foot of earwig showing nonadhesive (C-D) and adhesive (E) sides of microscopic features.[2] Used with permission: Arthropod 2004.

recently that the ridges on our fingertips allow skin to deform more laterally upon deformation, altering the amount of contact area between a finger and the surface, thus changing its frictional properties.[5,6]
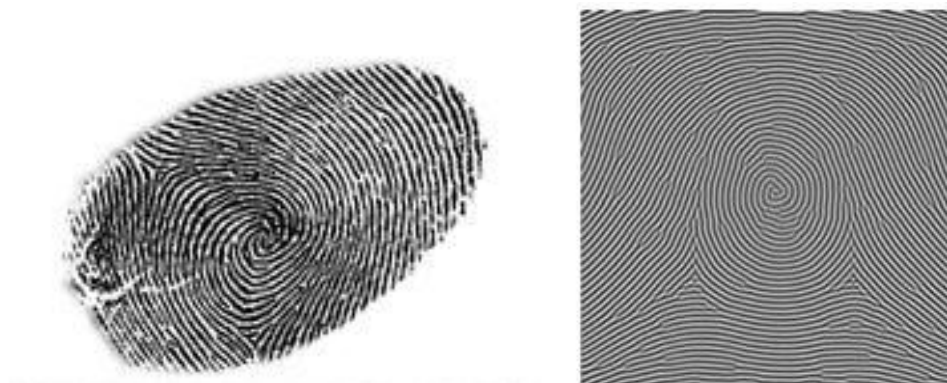
Figure 1.3: Fingerprint and wrinkle pattern simulation of wrinkling on curved surface.[3] Used with permission: J. Theor. Bio. 2005.

1.2 Introduction

Motivated by these examples from nature, the work presented here focuses on understanding the relationship between the characteristics of buckled surfaces and contact adhesion. Wrinkling is a patterning mechanism that shows significant industrial advantages such as facile, large area coverage; spontaneous formation; and feature sizes that can be tuned over a wide range of dimensions.[7–9] Utilizing the ability of wrinkling to affect surface adhesion, the research presented here extends the knowledge of wrinkled surfaces on contact adhesion. The normal adhesion of wrinkled surfaces has been studied in detail. Also, the development of novel biaxial wrinkle morphologies with two characteristic wavelengths has led to new wrinkle surfaces, which could allow further adhesion control. The overarching goal of this work is to develop a deeper understanding of the impact of surface instabilities on adhesion so that a wrinkled surface with specific adhesive properties can be engineered.

The ultimate application or motivation of this study is the ability to tune or control adhesion through simple scalable processes for many materials. Development of a scaling relationship that describes wrinkle adhesion will allow pattern-controlled adhesive

surfaces to be engineered on an industrial scale with relative ease. Additionally, by understanding the impact of patterned surfaces on adhesion, the principles used here can be applied to the study and characterization of a wide variety of natural adhesive systems that serve as inspiration to many scientists.

1.2.1   Project Overview

This thesis is divided into an introductory section and four main experimental projects. The introduction provides information on wrinkle morphology and the adhesive properties of wrinkled surfaces. The four experimental sections focus on 1) the adhesion of a single cylinder to a finite circular plate, 2) the mechanics of wrinkled surface adhesion for a "model" wrinkled surface, 3) the impact of viscoelasticity on wrinkle adhesion, and 4) the formation of unique wrinkle morphologies through the sequential application of orthogonal uniaxial strains. Each of the experimental project chapters includes background, an experimental approach, results, analysis, and discussion.

1.3   Wrinkle Formation and Morphology

Instabilities in the form of wrinkles or buckles occur frequently in nature and have been the focus of study for both their insight into fundamental structural mechanics as well as more applied uses of surface patterning. The formation of surface buckling instabilities occurs as a result of a lateral compression acting on an elastic plate that deforms out of plane to relieve the compressive stress.[10] This buckling is analogous to classic Euler buckling of a rod under uniaxial compression. In the case of wrinkles, the compressive stress can be applied in a number of ways, resulting in distinct, geometrically and materials properties-defined wrinkle morphologies.[11] Uniaxial

compression results in aligned wrinkle morphologies, while equibiaxial stress results in an array of morphologies ranging from dimples to labyrinth to herringbones.[12]
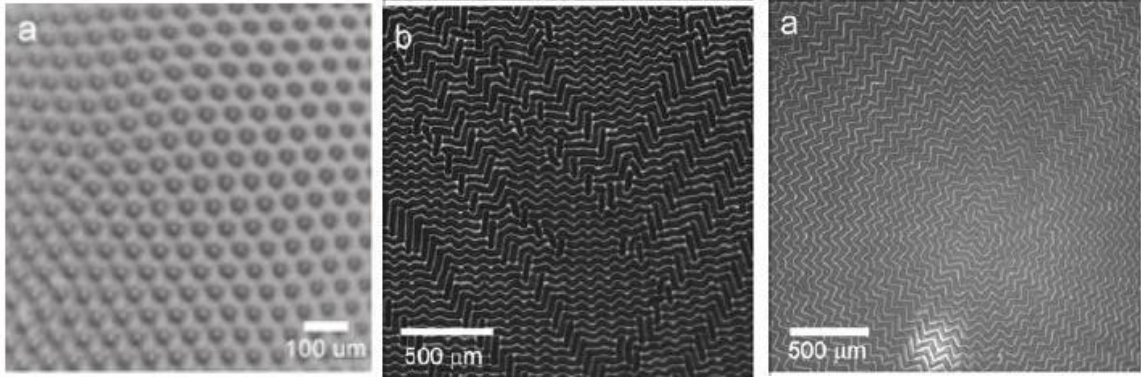
Figure 1.4: Wrinkle morphologies showing hexagonally packed dimples and two long ridge herringbone morphologies.[13]

1.3.1 Buckling Mechanics

One of the most common experimental sample geometries employed to study wrinkle morphology incorporates a thin rigid film fixed to a thick elastic substrate as shown in Figure 1.5. Allen's work on structural sandwich panels treats this case analytically and has become the fundamental work in the study of wrinkle mechanics.[14] When a composite or layered geometry is placed in lateral compression (whether uniaxial or biaxial), a competition exists between the deformation mode of the stiff plate which buckles out of plane (Figure 1.5aiii) and the in-plane, isotropic deformation mode inherent to the softer elastic substrate (Figure 1.5aii).

A characteristic wavelength, λ of the wrinkles can be calculated by minimizing the total energy per unit area, U_t. This total energy is a combination of the bending energy of the film and stretching energy involved in deforming the substrate (assuming "perfect" interfacial attachment) into the buckled profile of the film when the bilayer is
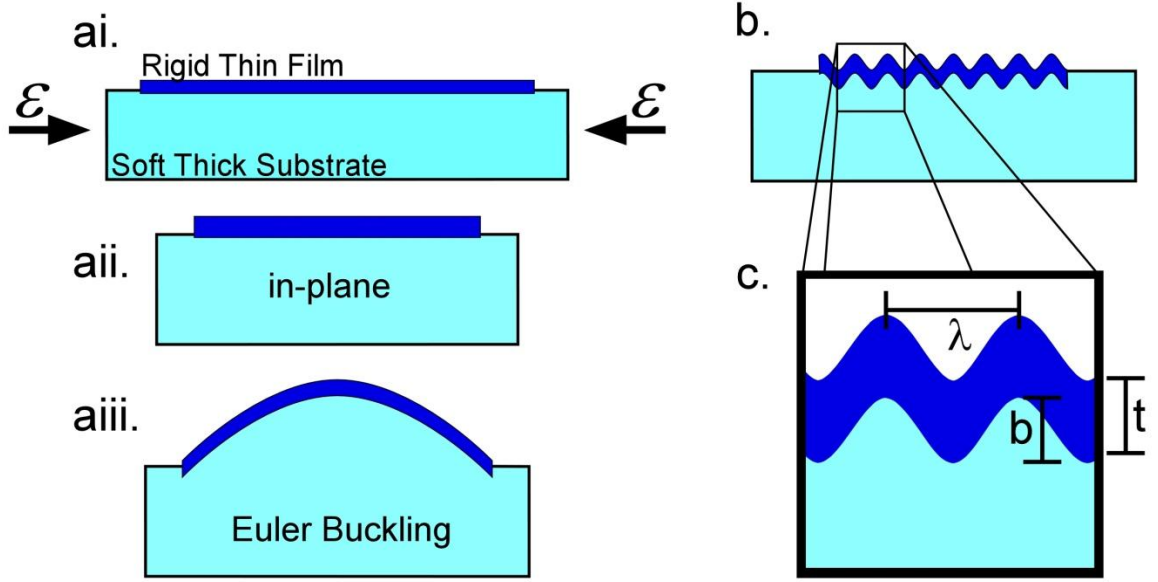
Figure 1.5: Schematic illustration of the mechanics of wrinkle formation. (ai) Rigid thin film attached to a soft thick substrate under compressive strain (uniaxial in this case). (aii) Simple in-plane deformation of film and substrate. (aiii) Out-of-plane deformation of film and subsequent deformation of substrate. (b) Periodic surface buckling or wrinkling. (c) Inset of a few wrinkles illustrating sinusoidal profile and various geometric parameters utilized throughout this work.

placed in compression. The bending energy of the film per unit area can be expressed as:[15]

$$\frac{U_b}{A} = \frac{\pi^4 t^3 \bar{E}_f b^2}{3\lambda^4}$$

(1.1)

where A is the area of the film, t is the film thickness, $\bar{E}_f$ is the plane strain modulus of the film ($\bar{E}_f = E_f/(1 - v_f^2)$ with v_f being the Poisson's ratio and E_f the Young's modulus of the film), b is the wrinkle amplitude, and λ is the wrinkle wavelength. The stretching or deformation energy per unit area is:[15]

$$\frac{U_s}{A} = \frac{\pi \bar{E}_s b^2}{4\lambda}$$

(1.2)

where $\bar{E}_s$ is the plane strain modulus of the substrate. U_s describes the energy required to deform or displace the substrate surface to conform to the bent or buckled profile of the

film. In the limit of small strains ($b \ll \lambda$), the compressive strain (ϵ) can be expressed as a ratio of the wrinkle amplitude and wavelength where:

$$\epsilon \sim \left(\frac{\pi b}{\lambda}\right)^2 \tag{1.3}$$

Utilizing this substitution, an expression for the total energy per unit area can then be written as:

$$\frac{U_t}{A} = \frac{U_s}{A} + \frac{U_b}{A} = \frac{\epsilon}{3}\left(\frac{3\lambda \bar{E}_s}{4\pi} + \frac{\pi^2 t^3 \bar{E}_f}{\lambda^2}\right) \tag{1.4}$$

By minimizing this total energy term with respect to the wavenumber ($\sim 1/\lambda$), a characteristic or preferred wrinkle wavelength can be calculated that is independent of ϵ. This characteristic wavelength is proportional to the film thickness and is represented by the expression now ubiquitous in wrinkling literature:[14,16,17]

$$\lambda = 2\pi t \left(\frac{\bar{E}_f}{3\bar{E}_s}\right)^{\frac{1}{3}} \tag{1.5}$$

The characteristic wavelength of a wrinkled system is shown to be a function of both the system geometry (t) as well as materials properties ($\bar{E}_f, \bar{E}_s$). However, the wrinkle amplitude is independent of geometry and depends only on the ratio of the two moduli, commonly referred to as the modulus mismatch and the amount of compressive strain applied to the composite system. The critical buckling strain threshold can be determined through an energy balance comparing the energy of a wrinkled surface with that of a surface compressing in-plane. The total energy of a wrinkled surface per unit area is:

$$\frac{U_{t,\lambda}}{A} = \frac{3t\bar{E}_s}{4}\left(\frac{\bar{E}_f}{3\bar{E}_s}\right)^{\frac{1}{3}} \epsilon \tag{1.6}$$

while the total energy of the compressed film deforming in-plane is:

$$\frac{U_{t,c}}{A} = \frac{t\bar{E}_f}{2}\epsilon^2 \qquad (1.7)$$

By setting $U_{t,\lambda} = U_{t,c}$ and solving for strain, the critical buckling strain (ϵ_c) for a uniaxially compressed system can be determined. The critical buckling strain is:

$$\epsilon_c = \frac{1}{2}\left(\frac{3\bar{E}_s}{\bar{E}_f}\right)^{\frac{2}{3}} \qquad (1.8)$$

The prefactors may vary slightly depending on the strain conditions and the analysis techniques used to develop this calculation.[7,18]

Once the applied strain reaches or exceeds this critical buckling strain threshold, low aspect ratio wrinkles form over the entire strained surface. The wrinkle amplitude increases as additional strain is applied to the system according to:

$$b = t\left(\frac{\epsilon}{\epsilon_c} - 1\right)^{\frac{1}{2}} \qquad (1.9)$$

Through this analysis, the onset of wrinkling can be calculated and compared with experimental observations. Also, wrinkled surfaces with specified wavelengths and amplitudes can be designed by tuning materials properties, sample geometry and strain conditions. The ability to control the feature size of wrinkles is essential if these surface instabilities are to be used as an industrial surface patterning technique. The simple mechanics relationships presented above will enable a range of wavelengths and amplitudes to be fabricated and the resulting normal adhesion to be characterized.

1.3.2   Compressive Strain Application

Wrinkles develop on the surface of a material that is placed in a state of lateral compression.[7,11] The most obvious method of applying a compressive strain to a layered composite material system is to simply impose a mechanical strain. Mechanical strain can be applied either by directly compressing the system or placing the substrate in tension

prior to application of the rigid film and relying on Poisson effects to compress the sample orthogonal to the applied tensile force upon release of this "prestrain".

Often in literature, a tensile prestrain is applied to the elastomeric substrate, the film is placed on the strained sample and then the tensile strain is released.[19] Through this method, wrinkles form upon the release of the tensile prestrain as restoring forces in the elastomeric substrate cause the substrate to contract, placing a compressive strain on the film transferred through the interface between film and substrate. This prestrain technique is an attractive way to form wrinkles since the wrinkle morphology is preserved on the sample surface after the prestrain is removed, allowing for facile surface characterization and sample manipulation. However, practical difficulties arise at high prestrain values as Poisson effects in the elastomer result in a tensile strain acting on the film parallel to the wrinkles. For rigid polymer films, undesirable cracks[20] and crazes[21] often form as a result of this orthogonal strain.

An additional technique made popular by the work of Harrison and coworkers,[22] takes advantage of Poisson effects to form aligned wrinkles. The SIEBIMM (strain induced elastic buckling instability modulus measurement)[17] process involves placing a thin film on an unstrained substrate, applying a uniaxial tensile strain to the substrate, and allowing the contraction of the substrate orthogonal to the applied strain (due to Poisson effects) to compress the film. The SIEBIMM technique results in aligned wrinkles formed parallel to the strain direction. Since the film and substrate have identical original strain states, releasing the applied strain results in recovery of a flat, unwrinkled surface.

Mechanical strain allows very precise control of the amount and direction of the applied strain. However, uniaxial mechanical strain tends to lead to the development of

defects in the aligned wrinkle pattern and experimental difficulties can arise from misalignment and complex boundary conditions.

Another form of strain that can result in wrinkling is thermal compression. In one of the first reports of wrinkle formation, wrinkles formed as a result of the thermal expansion mismatch of the composite materials.[16] Bowden and Whitesides deposited a thin film of metal on a thermally-expanded substrate and wrinkles developed upon cooling as the substrate contracted to a greater extent than the metal film and applied a compressive strain to the film. Thermal compression is advantageous in the formation of wrinkles as it can apply an isotropic or equibiaxial compression that results in uniform, biaxial wrinkle morphologies. However, a severe limitation of this technique is the reliance on the mismatch of the thermal expansion behaviors of the film and substrate, greatly restricting the materials that can be wrinkled using this application of strain as well as the amount of strain that can be applied.

A third method of applying a compressive strain to a system to form wrinkles is swelling of the film, substrate, or both. When a soft material is attached to a rigid substrate and swollen, the confinement of the surface opposes the lateral expansion of the material and results in surface instabilities ranging from wrinkles up to more highly strained instabilities such as creases and folds.[23,24] This method has been utilized to create wrinkled surfaces for previous wrinkle adhesion studies, which are reviewed in the following section.[25] While swelling is an effective technique to form wrinkles, experimental disadvantages include the need for very careful material/solvent materials selection as well as rapid drying and evaporation of solvent that complicates characterization of the wrinkled surfaces.

The new dipcoating wrinkle technique developed by Miquelard-Garnier and coworkers is a form of mechanical compression.[26] However, strain is applied to the sample in such a way that a local deformation occurs at the surface as one wrinkle at a time is formed. For traditional mechanical strain applications, the bulk substrate is compressed. Also, by forming each wrinkle individually, the number of dislocations and defects in the resulting aligned wrinkle pattern is greatly reduced over more conventional mechanical techniques.

1.3.3 Wrinkle Morphology

Wrinkle morphology or orientation has been studied in detail over the past few decades and researchers have demonstrated the ability to control wrinkle patterns to a large extent by altering boundary conditions and constraint scenarios.[8,12] Under uniaxial compression, aligned wrinkles form orthogonal to the compressive strain direction. Aligned wrinkles have also been observed in areas where sample geometry is constrained or confined (i.e. at the edge of a film), leading to areas of local uniaxial compression even under conditions of global biaxial strain. Aligned wrinkles will be used for the wrinkle adhesion experiments proposed here since they are easily modeled and can be formed reproducibly.

More complex and varied wrinkle morphologies form under biaxial compression. These wrinkle morphologies tend to fall in to two general categories: 1) dimples and bumps and 2) long ridges.[27] Biaxial compressive strains have been applied in a number of ways to form wrinkles, the three most common being thermal,[28,29] mechanical,[17,30] or osmotic[13,23] (swelling with liquid or vapor). Biaxially-strained wrinkle systems yield a variety of morphologies, many of which have been modeled through theoretical and

11

numerical analyses as well as observed experimentally.[27] Under equilibrium conditions (infinitesimally small strains and perfectly equibiaxial strain), certain morphologies have been predicted and observed repeatedly. Most notably, the square or hexagonally packed bumps or dimples at very low strains just above the critical buckling strain and a long ridge herringbone pattern at higher strains.[27]

Several groups have recently investigated the formation of wrinkles and the resulting morphologies that arise when biaxial strain is applied to a composite system but strains in the two primary directions are applied sequentially rather than simultaneously.[19,31,32] Ohzono and coworkers have conducted experiments on thin metal layers deposited on siloxane substrates.[31,33] The metal deposition process occurs at elevated temperatures so that upon cooling of the sample after applying the metal film, the mismatch in the thermal expansion properties of the metal and polymer result in a compressive strain that biaxially wrinkles the metal films.[31] These wrinkled samples are then subjected to a second, uniaxial mechanical strain and wrinkles were shown to rearrange and align perpendicular to the compression direction. The rearrangement was chiefly reversible with a small amount of hysteresis resulting from plastic deformation of the metal film.[33]

Two other notable studies on the impact of biaxial compression on wrinkle patterning were accomplished by the groups of Yang[19] and Stafford.[32] A study by Yang's group took advantage of Poisson's effects by applying an equibiaxial tensile strain to a siloxane rubber, oxidizing the surface, and releasing the strain in one direction to develop aligned wrinkles and then in the orthogonal direction to achieve well-ordered herringbone morphologies.[19] Alternatively, Stafford and coworkers relied on templating and molding

wrinkles into unstrained rubber, developing a checkerboard wrinkle morphology resulting from two sets of aligned wrinkles oriented perpendicular to one another.[32]

1.4 **Wrinkled Surface Adhesion**

Inspired by wrinkles used in nature to modify the adhesion of surfaces, wrinkling is an attractive surface patterning method to control adhesion. There are a couple of key advantages to note regarding wrinkle-based adhesive systems. First, the relative independence by which the lateral and height dimensions of these patterned surfaces can be controlled yields an extremely large parameter space and degree of control over the surface topography.[17] Second, since wrinkles form spontaneously as a result of a compressive strain, these surface patterns can be considered self-assembling.[25] Self-assembly inherently leads to facile pattern formation and also can be applied over a large area with relative ease, leading to obvious advantages in terms of industrial scale-up. Overall, wrinkled surfaces can be easily engineered to a specific wavelength, amplitude, and orientation and these features can be formed in a simple, inexpensive manner over extensive surface areas leading to precise control of the resulting adhesion.

Historically, considerations of periodically rough surfaces have been developed which are closely related to recent wrinkle adhesion studies.[34–39] Periodic roughness refers to asperities that have a uniform spatial distribution and uniform height. The uniform heights allow each asperity to act simultaneously and independently when contacting an opposing smooth surface.[36]

Johnson has considered low aspect ratio undulations on a surface that change the adherence force over that of a perfectly flat interface.[36,37] The undulations he considered had a sinusoidal profile and were shown to have an impact on the pressure distribution at

the interface. These periodically rough surfaces were of particular interest to Johnson and his contemporaries in the field of contact mechanics as they introduced periodic or controlled crack initiation sites from which cracks were shown to propagate in mathematically defined ways. The primary difference between this rich set of theory and current wrinkle adhesion literature is the aspect ratio of Johnson's structures. For the mechanical relationships presented in these references, the aspect ratios of the surface roughness or wrinkles are several orders of magnitude smaller than the wrinkles used in the study proposed here. In most of the periodic surface roughness adhesion works, full contact is achieved between thee smooth and rough surfaces.

1.4.1   Prior Wrinkle Adhesion Literature

Studies have been conducted on the adhesion of wrinkled surfaces over the last few years. The most notable studies have been performed by the Crosby group[23,40] and by Yang and Jagota.[30,41] These studies form the majority of prior wrinkle adhesion literature available. In these works, wrinkles have been shown to affect adhesion, either increasing or decreasing the overall force required to separate the interface over that of a smooth surface. Additionally, the size of the wrinkle feature geometry (amplitude and/or wavelength) can be changed to control the adhesive force.

These studies have shown the potential of wrinkles to control surface adhesion; however, each has limitations which call for further study to more completely understand the physical mechanisms that govern wrinkle adhesion. The wrinkle adhesion study presented here provides a more model wrinkled surface and testing geometry that can be generalized to other wrinkle systems. We present a complete study incorporating many

parameters that have an impact on wrinkle adhesion rather than focusing on only one or two variables.

In 2008, Chan and coworkers demonstrated enhanced adhesion using a flat, cylindrical punch and a swollen acrylate biaxial wrinkle system with a very low effective modulus and large critical strain energy release rate (G_c).[23] In their study, the separation stress or separation force per unit projected area increased with decreasing wavelength. The inverse relationship between adhesion and wavelength was attributed to the increased contact perimeter resulting from separating the area of contact into multiple smaller contacts. While their study was the first to demonstrate the importance of wrinkle feature size on separation force, it had a critical limitation. The material system employed had a large viscous or dissipative component that greatly increased the measured adhesion. Enhanced adhesion was a stated goal of this work, but the viscoelasticity of the acrylate system led to a complex separation mechanism that is difficult to model and develop predictions from. The work here concentrates first on fully elastic systems, removing complications arising from any viscoelastic effects before reintroducing dissipative material effects into the adhesion problems.

Lin and coworkers investigated the adhesion of aligned wrinkles using an oxidized siloxane materials system under mechanical compression and a spherical indenter.[30] Their work also showed an inverse relationship between the separation force and wrinkle feature size, though the amplitude rather than wavelength was used to measure wrinkle size. The use of an oxidized elastomer for this study leads to an inherently unknown chemical structure and material properties in the oxidized film. For conversion of polydimethyl siloxane (PDMS) to an oxide through the use of an

ultraviolet/ozone surface treatment, the thickness of the "rigid film" layer is difficult to

measure directly as is the Young's modulus of the layer as there is higher conversion to a

silica-like chemical structure on the near surface than in the sub-surface region. This

gradient in chemical and mechanical properties imparts a degree of uncertainty to the

interface and complicates analysis of the wrinkled structure formation. An additional

aspect of this study is the use of a spherical indenter to measure the separation force of a

wrinkled surface, which complicates the testing geometry, leading to a more complex

separation mechanism. Characterizing and modeling the separation of a spherical
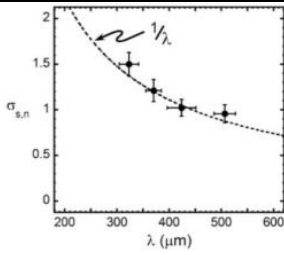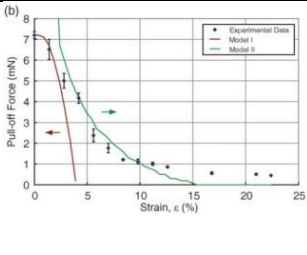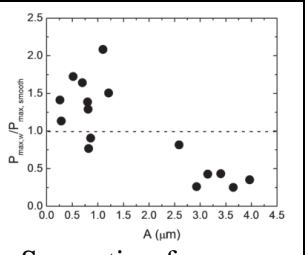
Reference	Chan (2008)	Lin (2008)	Kundu (2011)
Test geometry	Flat cylindrical punch	Sphere	Sphere
Material system	Viscoelastic acrylate	Oxidized, elastic siloxane	Oxidized, elastic siloxane
Wavelength (μm)	300-500	0.8-3.0	30-70
Amplitude (μm)	60-1005	0.05-0.15	0.3-5.0
Wrinkle Formation	Swelling-induced wrinkling, UV crosslinking, molding	UV oxidation, mechanical strain	UV oxidation, swelling-induced wrinkling, molding
Data	Adhesion strength vs. wavelength	Separation force vs. strain (amplitude)	Separation force vs. amplitude
Reported Relationship	$P_c \sim \dfrac{1}{wavelength}$	$P_c \sim \dfrac{1}{amplitude}$	$P_c \sim \dfrac{1}{wavelength}$ $P_c \sim \dfrac{1}{amplitude}$

Table 1.1: Summary of results and analysis from previous wrinkle adhesion studies.[23,30,40]
Used with permission: Adv. Mat. 2008; J. Poly. Sci. B. 2011.

indenter from a patterned surface is difficult since only the surface features near the perimeter of the projected contact exert an adhesive force on the probe upon separation. By utilizing a flat punch to study wrinkle adhesion, the work presented here improves on this study and offers additional insight into the adhesive properties of wrinkled surfaces.

A third, more recent study performed on biaxially strained wrinkles formed by vapor-phase swelling of a spherical cap of oxidized siloxane rubber demonstrated a similar dependence of adherence force on wrinkle feature size.[40] This study measured both the wavelength and amplitude of the wrinkles and showed a dependence of adherence forces on both dimensions. The same caveat of the spherical indenter testing geometry applies as for the Lin study. Table 1.1 summarizes the testing conditions and principle findings of each of these studies.

1.5 Project Aims and Goals

Prior wrinkle adhesion studies have shown that changing the size scale of wrinkle geometry can have a significant impact on the adhesive separation force of a patterned interface. However, the relationship between feature size (either wavelength or amplitude) and adhesive response is not a linear function and it is important to identify this scaling relationship, which has yet to be done quantitatively.

Also, each of these prior studies employed a complicated materials system, whether it is viscoelastic, unknown or inconsistent surface properties (PDMS surfaces are known to have varying concentrations of exposed hydroxyl and methyl functional groups as well as free siloxane oligomers that complicate the chemistry at the interface).[42] The wrinkle adhesion study presented here overcomes these experimental limitations by first utilizing elastic materials and a chemically symmetric interface of a high molecular

17

weight, low polydispersity index, amorphous glassy polymer (atactic polystyrene) so that the chemistry of the interface is well controlled.

By using a discrete capping film as the rigid layer rather than oxidizing the surface of the elastomer, the film thickness will be consistent and characterized to within a few nanometers and independent contact mechanics modulus measurements will be used to independently determine the modulus of the elastomeric substrate as well. Measuring the geometry and properties of the individual components of the bilayer system lends an added degree of certainty to the study presented here. By improving on these prior wrinkle adhesion experiments, our research on the mechanics of aligned wrinkle adhesion furthers the existing knowledge of wrinkle adhesion by developing a model system to allow more precise adhesion measurement and providing a scaling relationship that combines many significant factors such as testing probe geometry, materials properties, and wrinkle geometry.

1.6   Governing Questions and Overarching Approach

1.   How does a cylinder separate from a flat surface of finite area?

   a.   Form elastic cylinders of varying radii of curvature (R)

   b.   Characterize sample geometry and materials properties

   c.   Measure adhesion of cylinders with varying probe radii (c)

   d.   Develop scaling relationship relating separation force to cylinder and probe radius: $P_c \sim f(R, c)$

2.   How do wrinkles impact adhesion?

   a.   Fabricate wrinkled surfaces

   b.   Prepare symmetric interface

18

c. Reduce residual stress in wrinkles

d. Characterize sample geometry and materials properties

e. Measure adhesion of wrinkled surfaces

f. Relate separation force to wrinkle features, materials properties, and testing geometry: $P_c \sim f(\lambda, b, \bar{E}, G_c, c)$

3. What is the impact of viscoelasticity on the adhesion of wrinkled surfaces?

a. Fabricate rigid wrinkled surfaces

b. Characterize sample geometry and materials properties

c. Measure adhesion of wrinkled surfaces

d. Relate separation force to wrinkle features, material properties, and testing geometry: $P_c \sim f(\lambda, b, E')$

4. How can biaxial wrinkles with two discrete wavelengths be formed?

a. Fabricate uniaxial aligned wrinkles, alter modulus of substrate, apply secondary strain

b. Characterize primary and secondary substrate modulus

c. Observe and quantify resulting structures

d. Verify surface buckling mechanics relationships

CHAPTER 2

CYLINDER ADHESION

2.1 Introduction

The contact of a long rigid cylinder contacting a soft elastomeric surface along its axis is a classical mechanics problem that has been considered for decades.[43–45] The work of Barquins[46] and Chaudhury[47,48] has focused extensively on the theoretical and experimental aspects of the adhesion of a cylinder to a flat surface. In such fields as microelectronics and microbiology, the contact between a cylinder and a flat substrate must be controlled in order to develop appropriate processing conditions and engineering solutions.
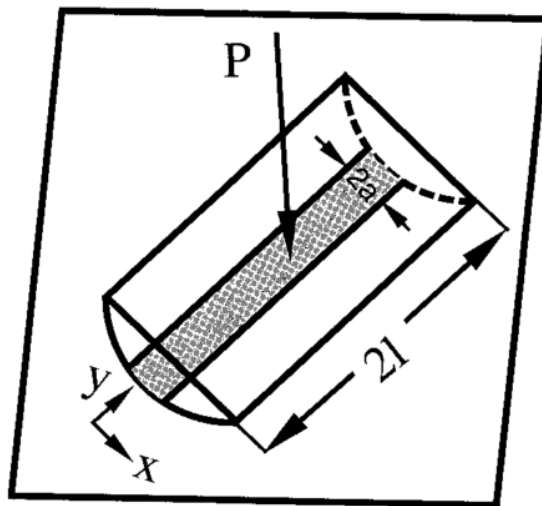
Figure 2.1: Schematic of topdown view of cylinder contact scenario.[47] Dark region represents contact area. Used with permission: J. App. Physics 1996.

Cylinder adhesion plays a key role in the attachment of round microwires in flexible electronics such as in the transfer of an array of gold wires from one substrate to another.[49] Additionally, in the micro and nanomanipulation of a nanoparticle,[50] the shape and adhesive properties of the cylindrical manipulators utilized for positioning purposes

are a critical design parameter that requires a thorough understanding of the adhesion and contact mechanics of cylinders.

The assembly, adhesion, and release of rod-like particles, either artificial or biological, are also dictated by the contact mechanics of cylinders. The contact behavior of bacilli, specifically common contaminants like Escherichia coli (E. coli), has been studied to develop new methods of abatement.[51] However, particularly in the case of contact models for E. coli and other fairly low aspect ratio, short cylinders, the relationships developed by Barquins[45] and confirmed by Chaudhury[47] may not be as valid since these models have been developed for long cylinders, neglecting the impact of the short ends of the contact.

In the context of the thesis presented here, specifically the adhesion of periodically rough or wrinkled surfaces, the contact and separation mechanism governing the adhesion of an individual cylinder must be determined. Here, the contact mechanism of a single elastic cylinder with a finite, circular flat punch will be investigated in order to account for the effects of the probe edges. The experiments presented in this chapter investigate the separation mechanism of cylinders that are short relative to their radius of curvature. The determination of the separation mechanism of these short cylinders will allow wrinkled surfaces to be modeled as arrays of short cylinders in subsequent chapters.

2.1.1   Background

To determine the separation mechanism of a cylinder of finite length, it is important to briefly review the more classic contact scenario of a rigid, infinite cylinder contacting an elastic halfspace. Using the approach presented by Johnson, Kendall, and

Roberts in the now famous JKR Adhesion theory paper, Barquins has developed the adhesion relationships for a rigid, infinite cylinder contacting a smooth, elastic halfspace.[45] (Note: here and throughout, P represents a normal force while $\bar{P}$ denotes normal force per unit length of a cylinder, wrinkle, or wrinkle array.)

Beginning with a contact scenario in the absence of adhesion, the contact area formed upon compression of a semicylinder on a flat surface (illustrated in Figure 2.1) is rectangular and the half contact width, a, increases as

$$a = \left(\frac{4\bar{P}'R(1-v^2)}{\pi E}\right)^{\frac{1}{2}} \tag{2.1}$$

where $\bar{P}'$ is the normal force per unit length in the absence of Van der Waals interactions (refered to as the Hertzian force), R is the radius of curvature, v is the Poisson's ratio, and E is the Young's modulus of the elastomeric substrate.[45] However, since there is substantial adhesion between the rigid cylinder and soft substrate, surface energy must be accounted for in determining the actual contact width observed at a given $\bar{P}$. Holding the contact width constant at $2a$ and increasing the surface energy, the Hertzian force, $\bar{P}'$, can be reduced to the actual force, $\bar{P}$. By considering the contact area to be formed by a rectangular flat punch of length l, and width $2a$, rather than a cylinder on a flat surface, fracture mechanics can simply be applied to determine the stress intensity factor, K_I along the long edges:[45,52]

$$K_I = \frac{(\bar{P}'-\bar{P})}{(\pi a)^{1/2}} \tag{2.2}$$

The well-known relationship taken from linear elastic fracture mechanics dictates that for a mode I crack opening geometry, the strain energy release rate, G is related to K_I by:[44]

$$G = \frac{K_I^2(1-v^2)}{E} \qquad (2.3)$$

Combining equations 2.2 and 2.3:

$$G = \frac{(\bar{P}'-\bar{P})^2(1-v^2)}{2\pi Ea} \qquad (2.4)$$

To determine the critical separation force, $\bar{P}_c$ and critical half contact width, a_c, we first solve equation 2.2 for $\bar{P}'$, substitute the resulting expression into equation 2.4, and solve for $\bar{P}$:

$$\bar{P} = \frac{\pi Ea^2}{4R(1-v^2)} - \left(\frac{2\pi EGa}{(1-v^2)}\right)^{\frac{1}{2}} \qquad (2.5)$$

At thermodynamic equilibrium, the critical strain energy release rate is equivalent to the work of adhesion, $G_c = w_{adh}$. The critical separation force and contact width are calculated by determining the load at $(\partial G/\partial A)_P = (\partial G/\partial a)_P = 0$:[53]

$$a_c = \left(\frac{2G_c R^2(1-v^2)}{\pi E}\right)^{\frac{1}{3}} \qquad (2.6)$$

$$\bar{P}_c = -3\left(\frac{\pi EG_c^2 R}{16(1-v^2)}\right)^{\frac{1}{3}} \qquad (2.7)$$

The critical separation force and half contact width correspond to the point at which the contact becomes unstable and two cracks propagate from the long edges of the contact area inward towards the center without any additional energy (in the form of a tensile load) being added to the system. These relationships are valid for long cylinders where the effects of the ends of the cylinder are neglected.

To compare our experimental results with these theoretical predictions, it is convenient to obtain an expression in terms of separation force, P_c^{cyl} rather than separation force per unit length. By multiplying both sides of equation 2.7 by cylinder

length, defined here by the diameter of the probe, $2c$, an expression for the critical separation force of a long cylinder is:

$$P_c^{cyl} = 3c \left(\frac{\pi \bar{E} G_c^2 R}{2} \right)^{\frac{1}{3}}$$

(2.8)

where $\bar{E}$ is the plane strain modulus given by $\bar{E} = E/(1 - v^2)$. A simple rearrangement of this separation force relationship yields an expression that normalizes the separation force by the materials properties (modulus and adhesion energy) to account for variations in crosslinking density and surface energy of the cylinders and probes respectively:

$$\frac{P_c^{cyl}}{\left(\bar{E} G_c^2 \right)^{1/3}} \sim c R^{\frac{1}{3}}$$

(2.9)

2.2 Experimental

2.2.1 Objective

The relationship between the contact geometry and materials properties of a long cylinder contacting a flat substrate is well understood. However, the impact of the cylinder ends or edges of the contact area on the separation mechanism have been widely neglected. Johnson includes a short description of the stress concentrations that can develop at the ends of a cylinder in his seminal work, *Contact Mechanics*.[44] However, the need still exists to determine the extent to which cylinder ends impact the separation mechanism, if at all, and if necessary, to develop an appropriate relationship accounting for these effects.

These experiments characterize the adhesion of elastomeric cylinders contacted with flat, axisymmetric probes. The radii of the cylinders, R and probes, c are varied so that the ratio between the two varies from $0.04 \leq c/R \leq 1.91$.

2.2.2 Cylinder Preparation

Rather than test the impact of short, rigid cylinders contacting an infinite, soft surface, the contact geometry is inverted so that rigid, flat probes with a finite circular face are utilized to probe long elastomeric cylinders as shown in Figure 2.2. In this way, the length of the contact, l (along the cylinder axis) is defined by the probe radius, c rather than the length of the cylinder. This inversion of the contact geometry is selected as it is a more direct analog to the wrinkle adhesion experiments that will be presented in Chapters 3 and 4. More practically, the selected geometry also greatly simplifies the cylinder fabrication and adhesion testing processes.
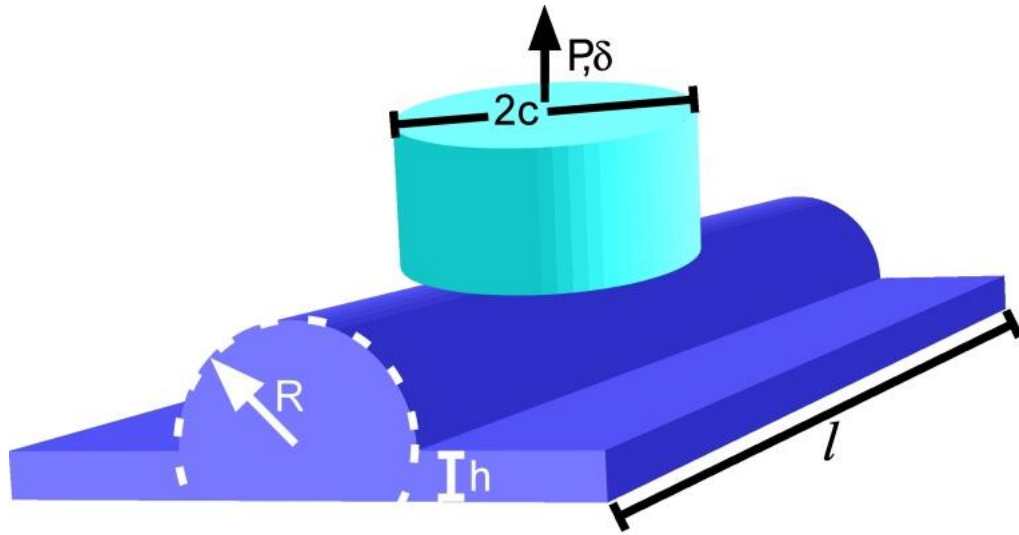
Figure 2.2: Contact geometry schematic of cylinder adhesion experiments.

For these tests, elastomeric cylinders are formed by molding polydimethyl-siloxane (PDMS) (Dow Corning Sylgard 184) in optically smooth glass tubes of varying inner radii (R=0.95, 3.00, 7.94, 10.94mm). The cylinders are cast from a mixture of 10:1 oligomer to curing agent by weight, degassed for 30 minutes, and cured at 130°C for two hours. Upon removal from the oven, thermal contraction of the elastomer is much greater than that of the tubular glass molds, enabling easy removal of the PDMS cylinders

without damaging their surfaces. After curing, the cylinders are cut in half lengthwise and affixed to a glass slide by attaching the flat side of the hemi-cylinder to a 1mm thick coating of uncured PDMS. The cylinder/substrate samples are placed in an oven for an additional 12 hours (T=130°C) to ensure complete crosslinking of all of the PDMS. A schematic of the final testing geometry is presented in Figure 2.2. For more details on the chemistry and crosslinking of PDMS, see the Appendix.

The radius of curvature of each cylinder is quantified through optical profilometry (Zygo NewView 7300). Several scans are taken of three different locations on each cylinder and the average radius of curvature determined. The range of these measurements for each cylinder was less than 5% of the average radius value.

2.2.3 Cylinder Adhesion Characterization

The normal adhesion of each cylinder is measured with a custom-built contact mechanics testing device.[23] A rigid cylindrical probe is mounted on a load cell which is subsequently attached to a piezo-controlled linear actuator (Burleigh Inchworm Nanopositioner) over the objective of an inverted microscope (Zeiss Axiovert 200M). The sample is then placed between the testing equipment and the microscope. All three components of the test are controlled simultaneously using a custom computer program (National Instruments Labview 8.5). Figure 2.3 is a schematic of the experimental setup. This testing method allows for the vertical displacement (δ) of the probe, the normal force (P), and the area (A) of the interface to be monitored over the course of a test.
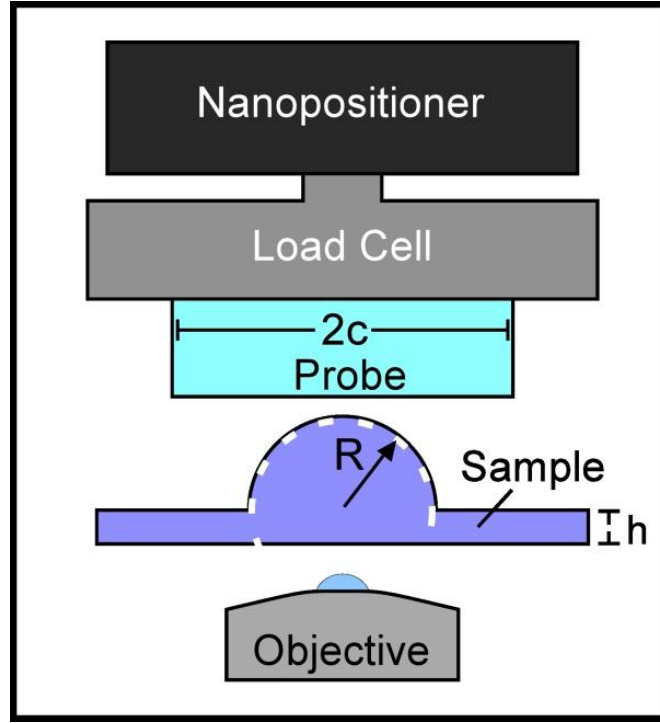
Figure 2.3: Schematic of contact adhesion setup.

Two probes are used for the cylinder adhesion experiments reported here. The size and material of the probes vary (see Table 2.1), and the surface energy of each probe is measured independently by contacting a smooth elastomeric substrate.

Probe	Radius, c (mm)	Material	Critical Strain Energy Release Rate, G_c (N/m^2)
1	0.50	Aluminosilicate, Al_2SiO_5	0.083
2	1.25	Sapphire, Al_2O_3	0.021

Table 2.1: Properties of rigid probes utilized for cylinder adhesion experiments.

An adhesion test consists of the probe being brought into contact with the sample, compressed at a fixed displacement rate until a specified, arbitrary maximum compressive force is achieved, and then the displacement is reversed until separation occurs. The contact area and force exerted on the probe are recorded throughout the test. In this study, tests have been performed at displacement velocities, V ranging from 0.1 to

1.0 μm/s and maximum compressive force values of P_m=-3mN to P_m=-50mN. However, within these ranges, little variation is observed in the value of the maximum separation force, or adherence force, P_c (Figure 2.4). Therefore, all cylinder adhesion data reported here are for P_m=-10mN and V=1.0μm/s.

Both probes have an RMS surface roughness of approximately 15nm over a lateral distance of 1mm, measured using optical profilometry (Zygo NewView 7300) over the entire face of the probe. Optical positioning equipment (Newport) is employed to ensure good parallel alignment between the face of the probe and the cylinder prior to each test.
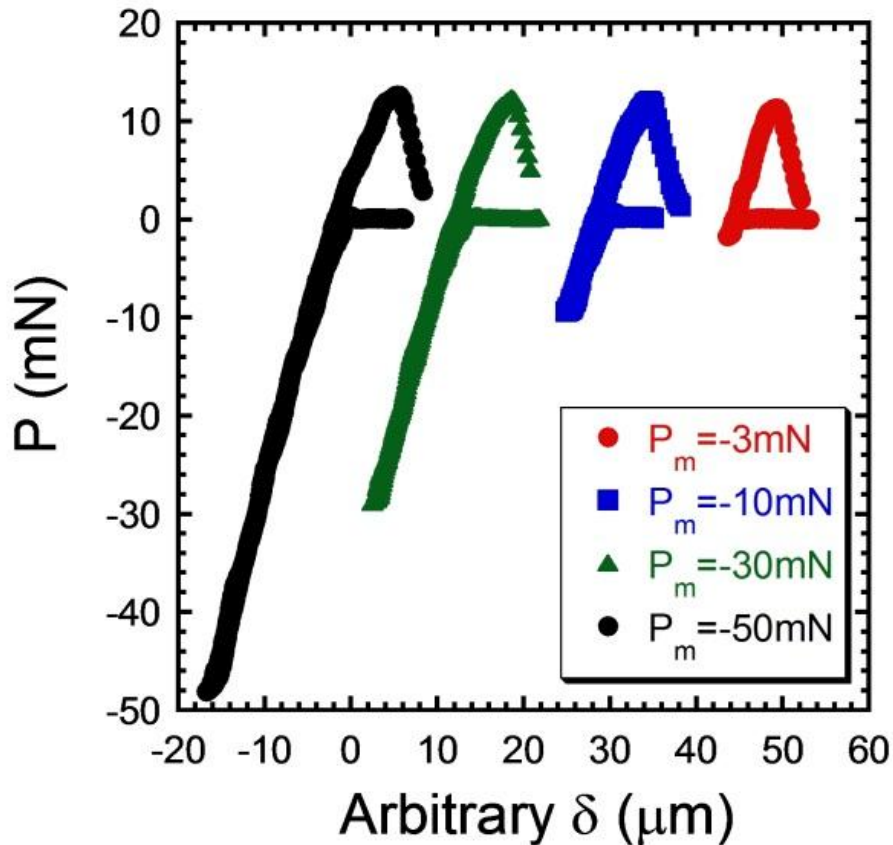
Figure 2.4 Force versus displacement data varying maximum compressive force (P_m). Tests performed with the same probe (probe 1) on the same cylinder (R=7.94mm, $\bar{E}$=4.0MPa, V =1.0μm/s).
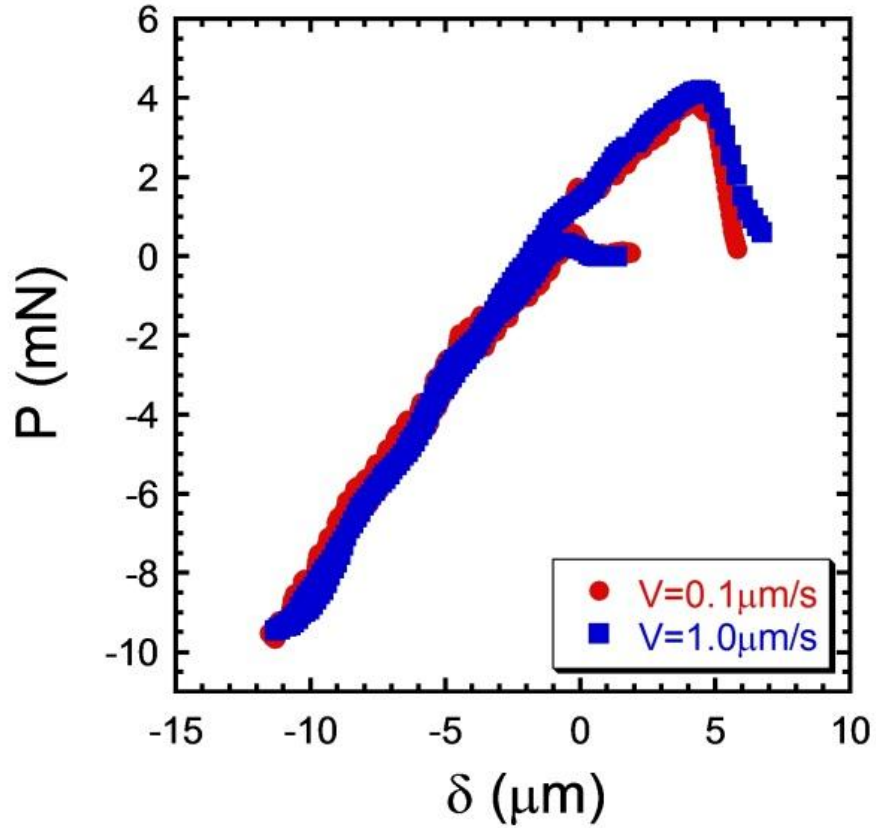
Figure 2.5 Force versus displacement data varying displacement rates. Tests performed with probe 1 on the same cylinder (R=0.65mm, $\bar{E}$=4.0MPa, P_m =-10mN).

2.2.4 Determination of G_c and $\bar{E}$

The critical strain energy release rate, G_c is a measure of adhesion energy and is related to both the materials properties of the two contacting surfaces, specifically their surface energy, modulus, and viscoelastic properties. G_c is defined as the amount of energy per unit width required to propagate a crack a specified distance.[52] In this work, G_c is used as an adhesion descriptor and typically considered a constant materials property.

Though crack propagation velocity can impact G_c, the tests presented here are performed relatively slowly and G_c is taken as a constant.[54] This assumption is supported by the relative testing rate independence of P_c measured here (Figure 2.5). By performing
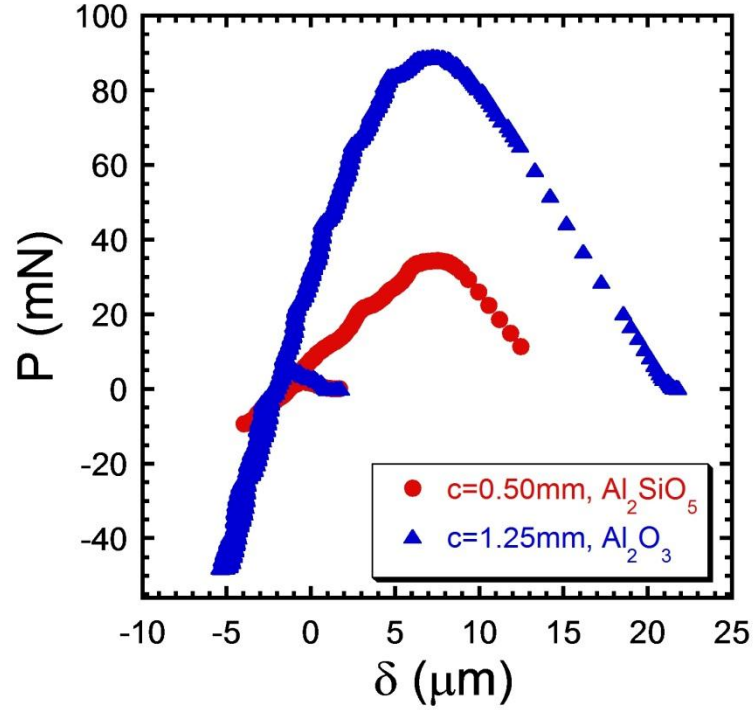
Figure 2.6: Representative force versus displacement plots for smooth probe contacting a smooth PDMS substrate.

contact adhesion tests on the smooth, unpatterned portion of each PDMS cylindrical sample with both probes, G_c is determined for each interface.

In order to measure the G_c of the interface, we employ the relationship of P_c, $\bar{E}$, and c to G_c given by Johnson for a flat circular punch.[44]

$$G_c = \frac{P_c^2}{8\pi\bar{E}c^3} \qquad (2.10)$$

This equation assumes that at the point of separation, the interface is at thermodynamic equilibrium (implying that the entire interface separates instantaneously at P_c). The two

tests shown here yield values of G_c=75mN/m and G_c=20mN/m, respectively (the average values of several tests are given in Table 2.1).

The modulus ($\bar{E}$) for each substrate is determined independently through contact adhesion measurements on a flat portion of the PDMS substrate. In these experiments, $\bar{E}$ is calculated from the stiffness ($K=dP/d\delta$) of the elastomer according to classical contact mechanics:[23]

$$\bar{E} = \left(\frac{1}{2c}\right)\frac{\partial P}{\partial \delta} \qquad (2.11)$$

2.3 Cylinder Adhesion

Contact images of the various probe and cylinder size combinations are shown in Figure 2.7b. Qualitatively, for testing geometries where $2c{\sim}R$, the contact areas are roughly rectangular and the width of the contact line changes as a function of the vertical displacement between the two contacting surfaces. However, for the contact geometries where the effective cylinder length is much smaller than R ($2c{<<}R$), the contact area is more elliptical and upon retraction of the probe, both the length and width of the contact area are observed to decrease. Additionally, the flat probes used here are circular; therefore, the "short" ends of the contact area have a noticeable curvature and the overall shape of the contact area can be approximated more closely by an ellipse than a rectangle.

The cylinder adhesion relationship presented in equation 2.9 is based on a fracture mechanics argument where two mode I fractures occur simultaneously along the long sides of the inward rectangular contact between the cylinder and the flat surface. Effectively, two peel events occur at the same time and propagate toward the center of the contact area upon separation. This argument works well for long cylinders on flat
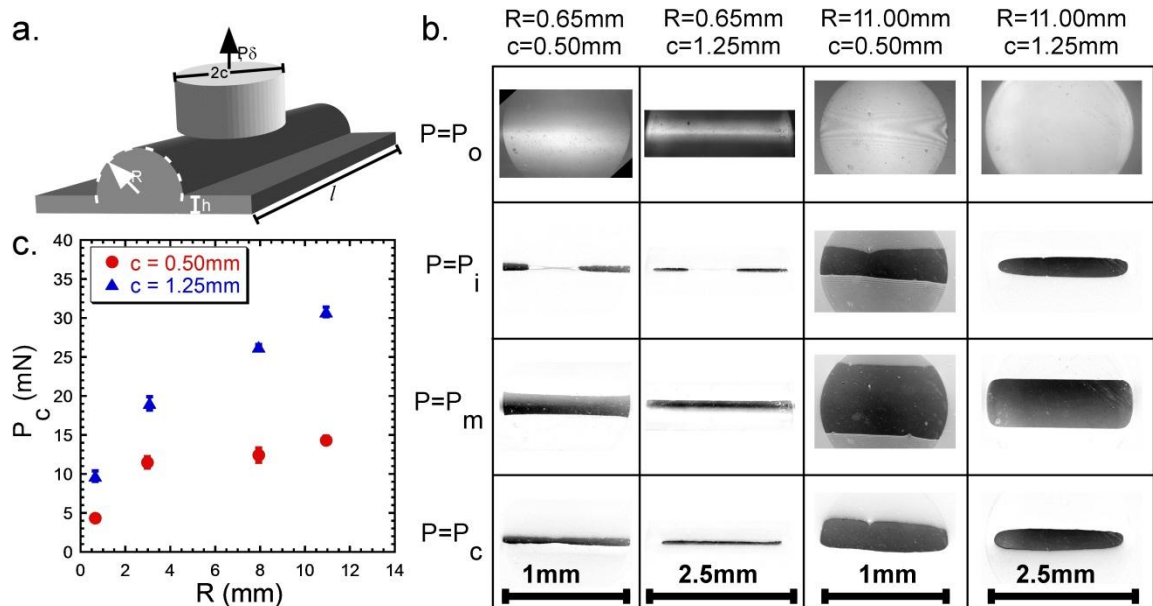
Figure 2.7: Single cylinder adhesion experimental results with finite cylindrical punch probes.[55] (a) Schematic of the testing geometry. (b) Optical micrographs of contact for several adhesion experiments of various probe and cylinder dimensions. The bottom three rows of images have been smoothed and subtracted from their respective background or reference images shown in the first row using ImageJ image processing software to allow the contact areas to be more easily seen. The scale bars apply to each column respectively. (c) Cylinder adhesion experimental results of separation force as a function of the cylinder radius of curvature for two different probe radii (c). Used with permission: Soft Mat. 2011.

surfaces. However, for cylinders of finite length, a similar relationship has not been proposed. Therefore, these cylinder adhesion experiments explore the separation behavior for a geometry where $2c \leq R$.

2.4 Determination of Separation Mechanism

2.4.1 Long Cylinder Separation Mechanism

The separation mechanism of a cylinder from a flat surface has classically been described by contact mechanics work performed by Barquins over the past three decades.[45,46,53] In utilizing the theories of Hertz[43] and Johnson and coworkers (JKR),[56] the relationships given in equations 2.8 and 2.9 have been presented previously. However in

the regime where the length and radius of the cylinder are on the same order, the validity of these relationships has not been proven.
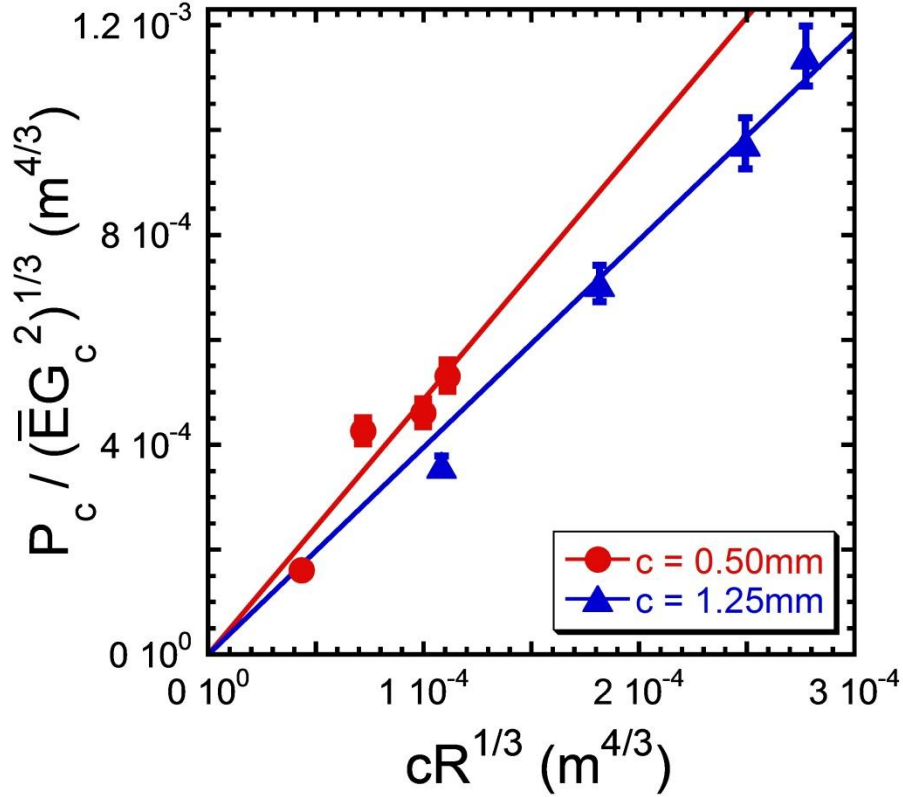
Figure 2.8: Single cylinder adhesion results using the contact mechanics relationships for an infinitely long cylinder contacting a flat substrate.

Equation 2.9 contains the geometric length scales of both independent variables (the probe and cylinder radii) on the right hand side of the scaling relationship. Plotting the cylinder separation force data as a function of these geometric terms allows for a quantitative test of the validity of this scaling relationship. In Figure 2.8, all of the data should collapse onto a single line with a constant slope if the long cylinder model is an appropriate way to describe the cylinder adhesion geometry of this study. The presence of two distinctly different slopes indicates that a better model should be developed to describe this data set.

33

2.4.2 Elliptical Contact Separation Mechanism

The most probable explanation for the deviation of our data from the long cylinder separation mechanism is the enhanced influence of cylinder end effects that could predominate or significantly impact the separation mechanism of short cylinders. As seen in the contact images presented in Figure 2.7b, upon separation the contact area decreases not only in the contact width direction but also along the axis of the cylinder. Here we present a new scaling theory that accounts for the decrease in contact in both directions simultaneously by developing a modified elliptical contact separation mechanism.
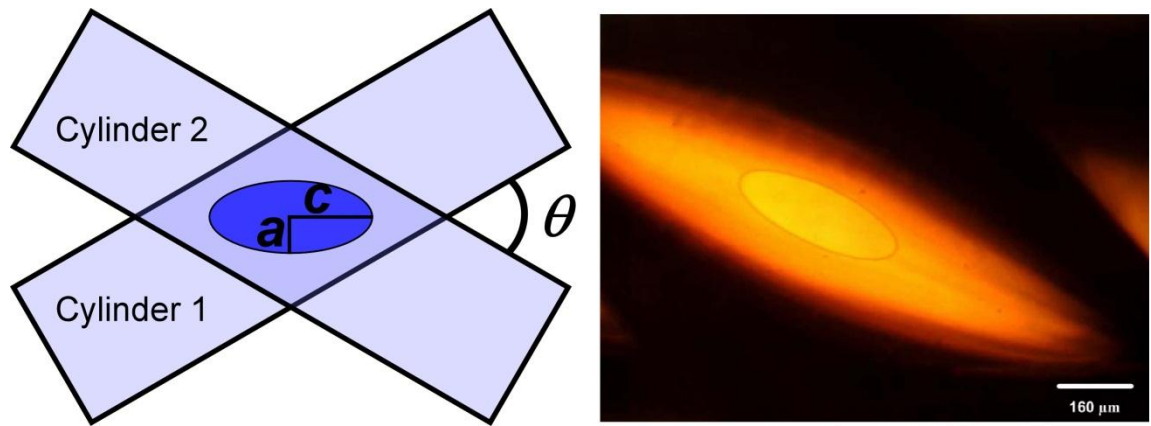
Figure 2.9: Crossed cylinder experiments of Sitti et al. Left: schematic showing top view of elliptical contact area (dark oval) formed from contact of two crossed cylinders adapted from Sümer et al.[57] Right: contact image (small light ellipse) resulting from two crossed PDMS cylinders.[57] Used with permission: J. App. Physics 2010.

Johnson has explored elliptical contact areas, specifically force, displacement and contact radius relationships by considering the contact of two identical crossed cylinders.[44] By varying the angle, θ formed between the axes of the two cylinders as shown in Figure 2.9, elliptical contact areas of varying eccentricities can be achieved.[57]

The Hertzian contact relationships for a rigid sphere contacting a flat elastic half-space in the presence of adhesion can be applied to this crossed cylinder contact scenario

by introducing a few simple geometric approximations. An effective contact radius, a_e and effective sphere radius of curvature, R_e are defined as:

$$a_e = (ac)^{\frac{1}{2}} \qquad (2.12)$$

$$R_e = (R_1 R_2)^{\frac{1}{2}} \qquad (2.13)$$

where R_1 and R_2 are the relative radii of curvature of the two crossed cylinders. The angle formed between the two cylinders affects these relative radii of curvature such that R_1 and R_2 can be determined by $R_1 = R/(1 - \cos\theta)$ and $R_2 = R/(1 + \cos\theta)$ respectively. When the cylinders are perpendicular to one another, $R_1 = R_2 = R$ and the classic Hertz contact mechanics relationships are recovered.[43]

This substitution leads to a slight underestimation of the contact area, resulting in an error of slightly less than 10%.[44] Assuming that this approximation is "good enough", we use the same equivalent contact radius and radii of curvature approximations in developing a scaling relationship for the separation force in the presence of adhesion.[44]

The force required to separate a rigid sphere from an elastic substrate is:[56]

$$P_c^{JKR} = \frac{3}{2}\pi G_c R \qquad (2.14)$$

Additionally, we know that the contact radius of the resulting circular contact area, a_c^{JKR} at the point of separation is:

$$a_c^{JKR} = \left(\frac{9\pi G_c R^2}{8\bar{E}}\right)^{\frac{1}{3}} \qquad (2.15)$$

Solving equation 2.15 for R:

$$R = \left(\frac{8\bar{E}a_c^3}{9\pi G_c}\right)^{\frac{1}{2}}$$

(2.16)

By substituting this result into the JKR separation force prediction (equation 2.14), a relationship between the separation force of a sphere from a flat substrate in terms of materials properties and contact width or radius is obtained:

$$P_c^{JKR} = (2\pi G_c \bar{E} a^3)^{\frac{1}{2}}$$

(2.17)

For an elliptical contact, $a = a_e$:

$$P_c^{ell} = (2\pi G_c \bar{E})^{\frac{1}{2}}(ac)^{\frac{3}{4}}$$

(2.18)

To get P_c in terms of G_c, $\bar{E}$, c and R, the contact width of the elliptical contact must be obtained. Using image analysis software (ImageJ, NIH), the width of the contact over the course of each cylinder adhesion test is measured. These contact width values tracked fairly well with the contact width predicted by the long cylinder scaling. Thus, Barquins' long cylinder separation width (equation 2.6) is substituted into equation 2.18 for a resulting in the relationship for the elliptical contact mechanism separation force:

$$P_c^{ell} = (2\pi G_c^3 \bar{E} R^2)^{\frac{1}{4}}c^{\frac{3}{4}}$$

(2.19)

Once again, we rearrange this relationship to normalize the separation force by materials properties and present P_c^{ell} as a function of probe and cylinder radii:

$$\frac{P_c^{ell}}{(\bar{E}G_c^3)^{\frac{1}{4}}} \sim (c^3 R^2)^{\frac{1}{4}}$$

(2.20)

Figure 2.10 shows the relationship given in equation 2.20 for both size probes. The slopes of the two lines are the same, indicating an elliptical contact separation mechanism is a more appropriate model to use for the short cylinders tested here. It is important to note that this ellipsoidal separation force scaling relationship has been developed for the

36

parameter space where $0.01 \leq c/R \leq 10$. For the two extreme contact geometry cases where R is very small or very large relative to c, different contact relationships would be expected. For $c/R \rightarrow 0$, the separation mechanism would approximate a flat, circular punch contacting a flat surface such that:

$$P_f = (8\pi \bar{E} G_c c^3)^{\frac{1}{2}} \qquad (2.21)$$
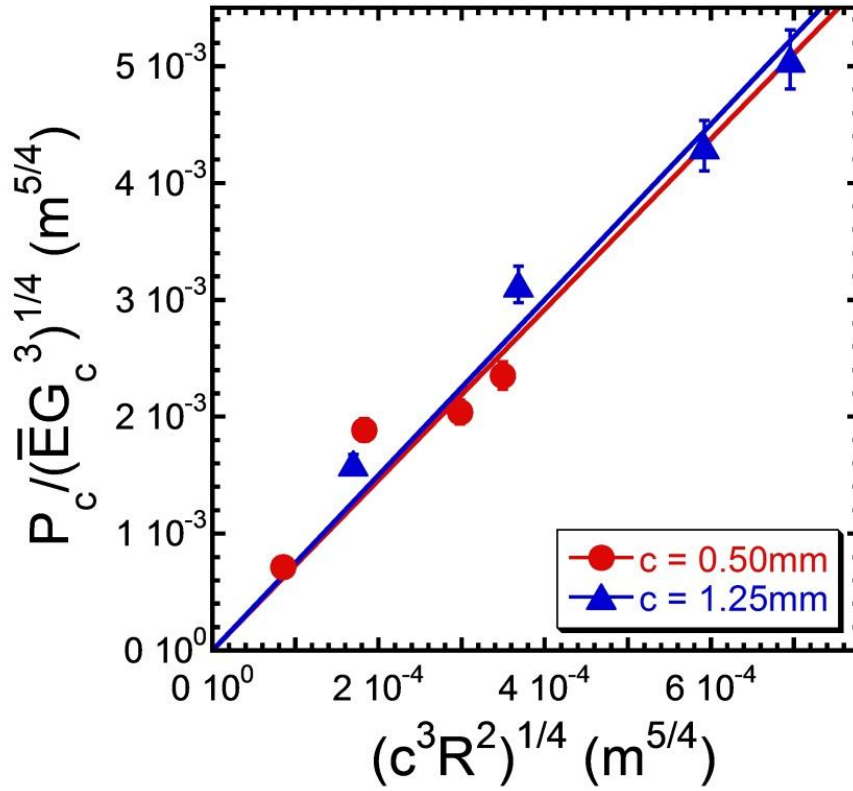
Figure 2.10: Single cylinder adhesion results using the contact mechanics relationships for an elliptical contact area resulting from contacting an ellipsoid with a flat substrate.

This relationship for the separation force is independent of the radius of curvature of the cylinder and the contact area will be circular in shape and have a radius determined by the size of the probe. For $c/R \rightarrow \infty$, the separation force relationship returns to the

solution found by Barquins and presented in equation 2.8 for a long cylinder contacting a flat surface.

2.5   **Conclusions**

The modified elliptical contact separation mechanism scaling derived in equation 2.20 is a robust, appropriate model that can be applied to cylinder-on-flat contact adhesion scenarios where the length of the cylinder is on the order of the radius of curvature of the cylinder $(c \sim R)$. Such applications could include rod-like nanoparticle assemblies[58] and the adhesion of bacilli or capsule-shaped bacteria such as E. coli.[51] In Chapter 3, the separation force relationship for a short cylinder separating from a finite circular probe presented in equation 2.19 will be used to develop a scaling prediction for the force required to separate a flat probe from a surface of aligned wrinkles.

CHAPTER 3

MECHANICS OF WRINKLED SURFACE ADHESION

3.1 Introduction

The adhesive properties of wrinkled surfaces are investigated here. We develop a surface of aligned wrinkles on a relatively thick elastomeric substrate and then measure the normal adhesion properties, specifically the separation force required to remove a flat circular punch from the wrinkled surface. The elliptical contact separation mechanism of a single short cylindrical contact investigated and described in Chapter 2 is utilized to develop a relationship between the wrinkle geometry, materials properties and testing geometry and the separation force.

3.2 Background

Control of surface properties through patterns is commonly found in nature. Arachnids, insects, and several types of reptiles including skinks and geckos use patterns on their feet to tune adhesion.[1,59,60] Plants, such as the Sacred Lotus, use periodic surface roughness to control the wetting properties of their leaves.[61] Inspired by these examples, patterns have been used to fine tune the surface properties of various synthetic materials. Whether the patterns consist of chemical variations or topographic features, the effects on the wetting, friction, and adhesive properties of engineered surfaces have been characterized and studied.[62,63]

In most instances, complex and expensive fabrication techniques ranging from lithography to carbon nanotube processes have been used to create these synthetic analogs to naturally-occurring surfaces.[64,65] However, wrinkled surfaces (which are

spontaneous or self-forming and attractive for large scale, inexpensive pattern production) have recently been explored as an alternative patterning method to these more conventional patterning techniques. Wrinkles are caused by a compressive strain on a surface. By altering the strain conditions through materials properties, system geometry, and processing conditions, researchers have been able to demonstrate great control over wrinkle wavelength (λ), amplitude (b), and orientation over large areas.[7]

As control over wrinkle morphology has progressed, groups have studied the ability to use these structures to control surface properties, such as friction and adhesion.[40,66,67] Lin and coworkers have shown that wrinkle aspect ratios (b/λ) can be used to control the maximum separation force of a rigid sphere on a wrinkled surface.[30] Further, Chan and coworkers have shown that decreases in wrinkle wavelength can lead to enhanced adhesion of a rigid, flat punch on a wrinkled surface.[23] More recently, the impact of both wavelength and amplitude on the adhesion of a curved surface has been reported.[40] A summary of these studies and their primary findings is presented in Table 1.1. These works have demonstrated the impact of wrinkle topography on the apparent adhesion of a surface; however, there are still many fundamental questions of wrinkle adhesion that have yet to be understood.

In this chapter, we investigate the adhesion of aligned wrinkles consisting of a glassy polymer film attached to an elastomeric substrate using a rigid, flat punch under normal adhesion conditions. Since surface buckling instabilities are developed by the application of a compressive strain to a confined surface, stored energy is inherently present in each sample. Taking advantage of the curing kinetics of the elastomeric substrate, we utilize wrinkles where the residual stress or stored energy of the system is

diminished, allowing the wrinkle geometry effects to be studied independently from the impact of residual stress. Furthermore, we choose materials with known elastic moduli and interfacial properties to allow us to develop a confirmed scaling relationship between the adherence force, materials properties, and wrinkle geometry.[17,68]
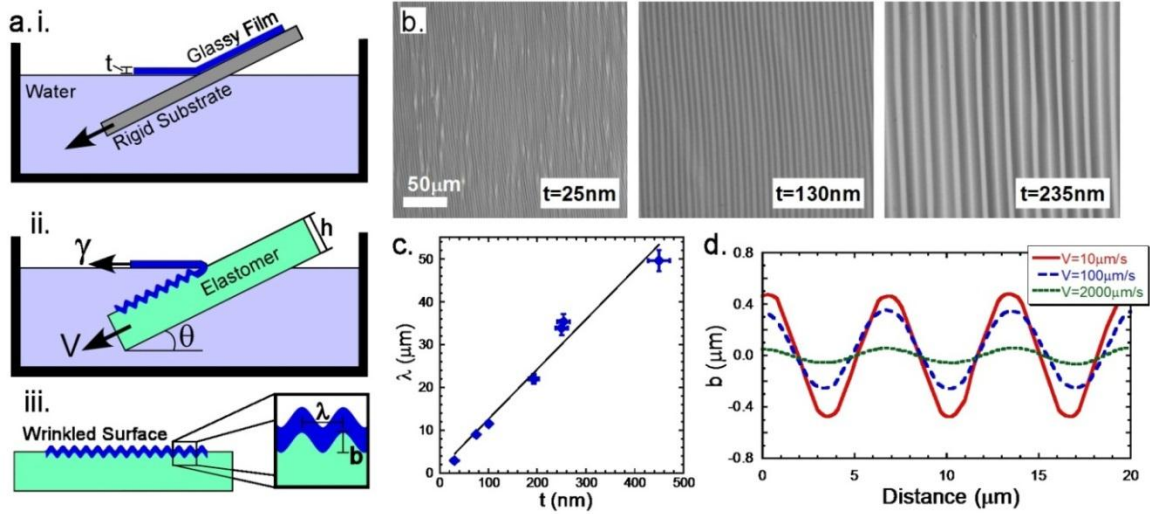
Figure 3.1: Aligned wrinkle fabrication. (a) Schematic of wrinkle fabrication technique.[55] (b) Optical micrographs of samples created by the wrinkle fabrication technique. Glassy films of varying thicknesses (*t=25, 130, 235nm*) have been applied to the same elastomeric substrate. The scale is the same for all three images. (c) Linear relationship of measured wrinkle wavelength (λ) as a function of film thickness. (d) Optical profilometry surface profile traces of wrinkled samples cast at different velocities on the same substrate with the same film (*t=50nm*). Used with permission: Soft Mat. 2011.

3.3 Experimental

3.3.1 Wrinkle Formation

The process used to form wrinkles on the surface of the smooth elastomeric substrates yields uniform, aligned wrinkles with an almost perfectly sinusoidal cross-sectional profile (Figure 3.1d). This technique has been reported previously by Miquelard-Garnier and coworkers.[26] Figure 3.1a contains a schematic of this process.

For the study reported here, the glassy thin films are high molecular weight, atactic polystyrene (PS) (M_n=1,100kg/mol, PDI = 1.15, Polymer Source, Inc.) spincoated

from toluene (Fisher Scientific) onto ultraviolet/ozone (Jelight 342 UVO system) treated silicon wafers (University Wafer). By varying the concentration and spin speed, film thicknesses, t, ranging from 20nm to 300nm as measured by white light interferometry (Filmetrics) are obtained. The substrates are polydimethyl siloxane (PDMS) (Dow Corning Sylgard 184) prepared using an oligomer to curing agent ratio of 10:1 by weight. The PDMS mixtures are degassed in a reduced pressure environment for 30 minutes, poured into glass molds measuring 30x50mm to form a flat layer approximately 3mm thick, and cured at 70°C for 20 minutes (resulting in a tacky, partially cured rubber).[55] The modulus of each partially crosslinked substrate is determined independently using the custom built contact mechanics device described in Section 3.3.2.

After wrinkling the PS film on the PDMS, the samples are allowed to finish curing either in a 70°C oven for 24 hours or at room temperature (25°C) for 120 hours. Wrinkle wavelength, amplitude, and substrate modulus are monitored over the course of the curing process using optical profilometry (Zygo NewView 7300) and contact mechanics testing (see Section 3.3.2). While the wrinkle geometry does not change as a result of the curing process, the substrate modulus increases as expected until a final, consistent modulus value of $\bar{E}_s = 1.25MPa$ (120 hours at 25°C) or $\bar{E}_s = 2.00MPa$ (24 hours at 70°C) is reached as shown in Figure 3.2. Details of the PDMS crosslinking process are provided in the Appendix.

This wrinkle fabrication technique covers large areas (several cm^2) with well-aligned wrinkles over the course of a few minutes. Figure 3.1b contains optical micrographs of three different samples prepared with films of increasing thickness,

showing the wrinkle alignment and giving some sense of the long range order achievable with this method.
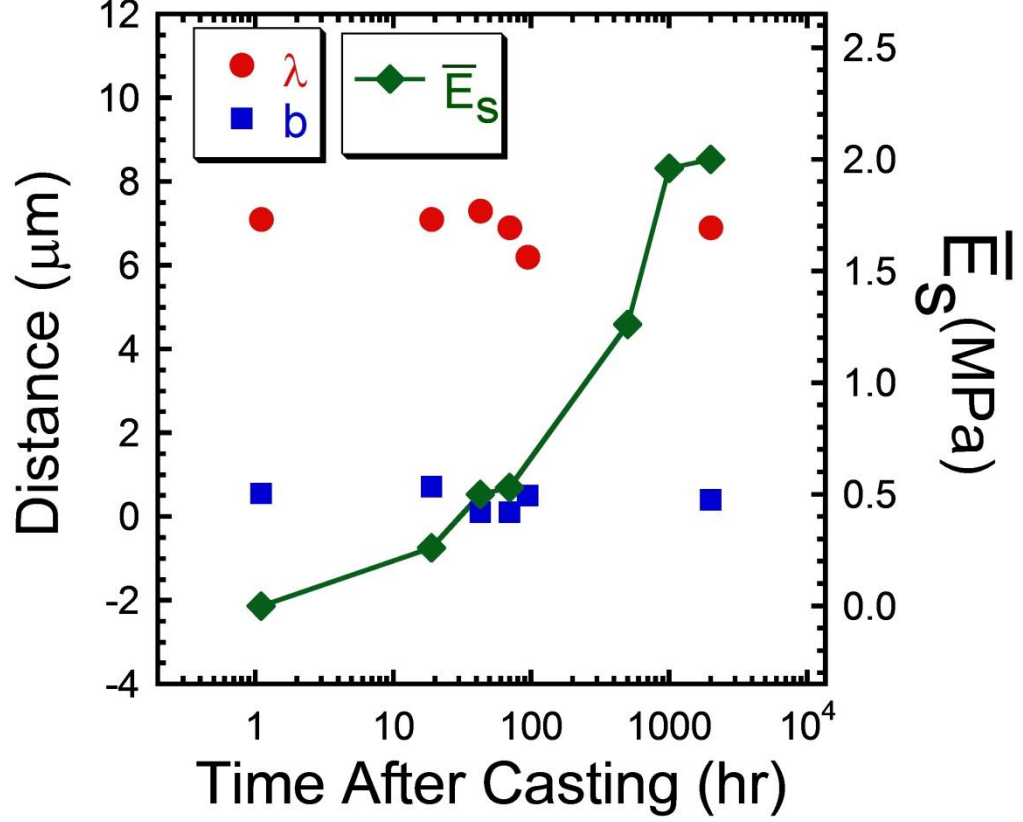
Figure 3.2: Wavelength, amplitude, and substrate modulus as a function of curing time. Created from a substrate with a 10:1 oligomer: curing agent mixture of PDMS and cured at room temperature (25°C) and a PS film with t=18nm.

Wrinkle wavelength and amplitude can be controlled independently through materials properties, sample geometry, and process parameters. The wavelength of each wrinkled surface is determined by the elastic modulus mismatch between the stiff film and soft substrate $(\bar{E}_f/\bar{E}_s)$ and the thickness of the film (t) according to:[14,16,17]

$$\lambda = 2\pi t \left(\frac{\bar{E}_f}{3\bar{E}_s}\right)^{\frac{1}{3}}$$

(3.1)

In the present study, the glassy film and elastic substrate are held constant and the wavelength is tuned by controlling the film thickness. The modulus of the film is constant

for all samples ($\bar{E}_f = 3.00GPa$). Figure 3.1c shows the linear wavelength dependence on film thickness, with the slope of the line representing the modulus mismatch and yielding a plane strain modulus value of $\bar{E}_s = 0.43MPa$ for the partially-cured PDMS substrate. This modulus value is in good agreement with the results of the contact mechanics measurements performed on this partially-cured elastomeric sample.

While the wrinkle wavelength is controlled through materials properties and film geometry, the wrinkle amplitude is determined by the processing parameters, specifically the processing velocity utilized during wrinkle formation. Details on the effect of velocity on the amplitude have been published previously[26] and are shown in Figure 3.1d. Essentially, the slower the processing velocity, the larger the strain (ϵ) applied to the substrate during the formation of the wrinkles, resulting in higher wrinkle amplitudes through the relationship:

$$\frac{b}{\lambda} \sim \sqrt{\epsilon} \qquad\qquad (3.2)$$

Additional parameters that impact the applied strain are the surface tension (γ), and the adhesion energy between the glassy film and soft substrate. In Figure 3.1d, it can be seen that changing the processing velocity by an order of magnitude results in a marked change in the amplitude of the wrinkled structures with minimal effects on the wavelength.

By applying the film prior to final curing of the substrate, the wrinkled surfaces have lower residual stress states than surfaces with films applied to fully crosslinked substrates. A more practical advantage of the two step curing process is that after crosslinking the substrate, the film can be removed by dissolving it away with an appropriate solvent, allowing the wrinkled substrate to be characterized with or without

the capping layer. Removal of the film from the wrinkled substrates processed in two thermal curing steps does not have any impact on the aspect ratio of the surface patterns; the wrinkles remain the same size and shape. For wrinkles created on fully crosslinked substrates, removal of the flat films results in relaxation of the surface and disappearance of the wrinkles.

3.3.2 Adhesion Characterization

The normal adhesion of each wrinkled surface is measured with a custom-built contact mechanics testing device.[23] A PS-coated rigid flat punch with a circular face is used as the probe. This probe is mounted on a load cell which is subsequently attached to a piezo-controlled linear actuator (Burleigh Inchworm Nanopositioner) over the objective of an inverted microscope (Zeiss Axiovert 200M) equipped with a CCD camera (Pixelfly). The sample is then placed between the testing equipment and the microscope. All three components of the test are controlled simultaneously using a custom computer program (National Instruments Labview 8.5). Figure 3.3a is a schematic of the experimental setup. This testing method allows for the simultaneous measurement of the vertical displacement (δ) of the probe, the normal force (P), and the area (A) of the interface over the course of a test.

An adhesion test consists of the probe being brought into contact with the sample, compressed at a fixed displacement rate until a specified, arbitrary maximum compressive force is achieved, and then the displacement is reversed until separation occurs. The contact area and force exerted on the probe are recorded throughout the test. In this study, tests have been performed at crosshead velocities ranging from 0.1 to 1.0μm/s and maximum compressive force values of P_m=-10mN to P_m=-50mN. However,
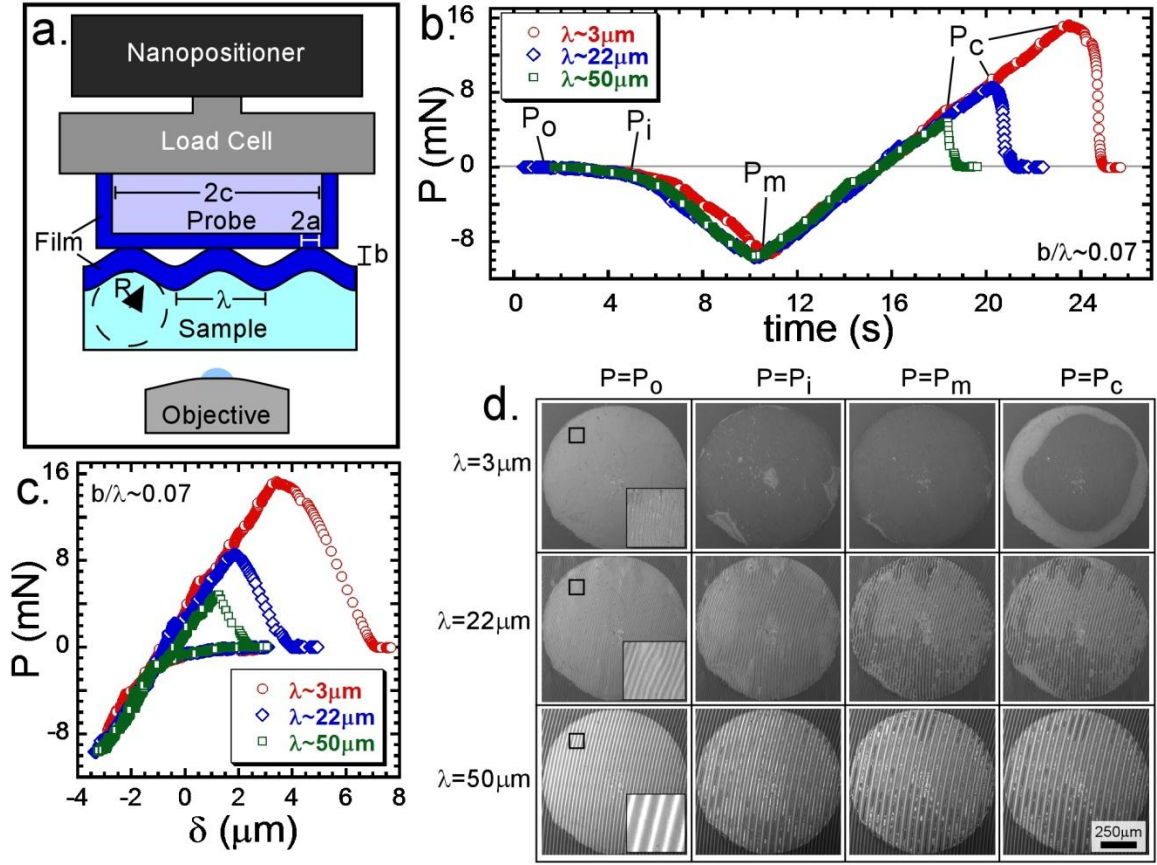
Figure 3.3: Adhesion testing procedure and initial results.[55] (a) Schematic of the contact adhesion measurement setup. (b) Force (P) as a function of time with significant points labeled corresponding to: P_o, before the probe contacts the sample surface; P_i, initial contact; P_m, maximum compression; and P_c, separation. (c) Typical force versus displacement (d) plots where $P<0$ is compression and $P>0$ is tension. (d) Optical micrographs of the contact areas for wrinkled samples of various wavelengths throughout an adhesion test. Insets are 100x100μm. All results presented here are for wrinkles with an aspect ratio of $b/\lambda\sim0.07$ and approach and retract velocities are 1.0μm/s. Used with permission: Soft Mat. 2011.

within these ranges, little variation was observed in the value of maximum separation force, or adherence force, P_c (Figure 3.4). Therefore, all wrinkle adhesion data reported here are for P_m=-10mN and V=1.0μm/s. Each data point represents an average of three tests.

For all tests, unless otherwise stated, a cylindrical probe with a radius (c) of 500μm is used. The flat, circular face of this probe is coated with a 250nm PS film and

46

annealed at 160°C for 5 minutes to ensure conformal contact and prevent delamination between the cylindrical probe surface and the film during testing. The PS coated probe
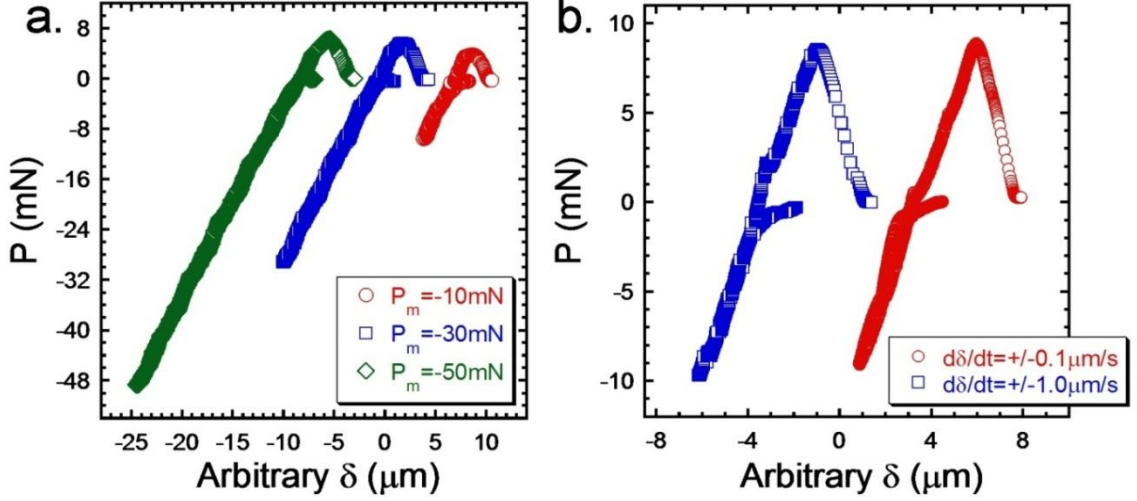
Figure 3.4: Wrinkle adhesion force versus displacement. Adhesion tests performed at (a) various maximum compressive force (P_m) values on the same wrinkled substrate (λ=22.0μm, b=2.92μm, $\bar{E}_s = 1.25 MPa$) and (b) various displacement rates on the same wrinkled substrate (λ=21.9μm, b=1.53μm, $\bar{E}_s = 2.00 MPa$).[55] Used with permission: Soft Mat. 2011.

has an RMS surface roughness of approximately 15nm over a lateral distance of 1mm, measured using optical profilometry over the entire face of the probe. Optical positioning equipment (Newport) is employed to ensure good parallel alignment between the face of the probe and the sample surface prior to each test.

The same polystyrene film is used to coat both the surface of the wrinkled samples and the probe used for adhesion testing. Since both surfaces have identical chemistry, the work of adhesion, w_{adh}=2γ where γ is the surface energy of each contacting surface.[53] At equilibrium, w_{adh}=G_c, the critical strain energy release rate, as modeled using linear elastic fracture mechanics.[69]

Though crack propagation velocity can impact G_c, the tests presented here are performed relatively slowly and G_c is taken as a constant.[54] This assumption is supported

47

by the relative testing rate independence of P_c measured here (Figure 3.4b). By performing contact adhesion tests on smooth, unpatterned PS films attached to a PDMS substrate with the PS-coated cylindrical probe, G_c has been measured and is found to be 48 mN/m for the PS-PS interface. This value for the critical strain energy release rate is in good agreement with values from literature.[70]
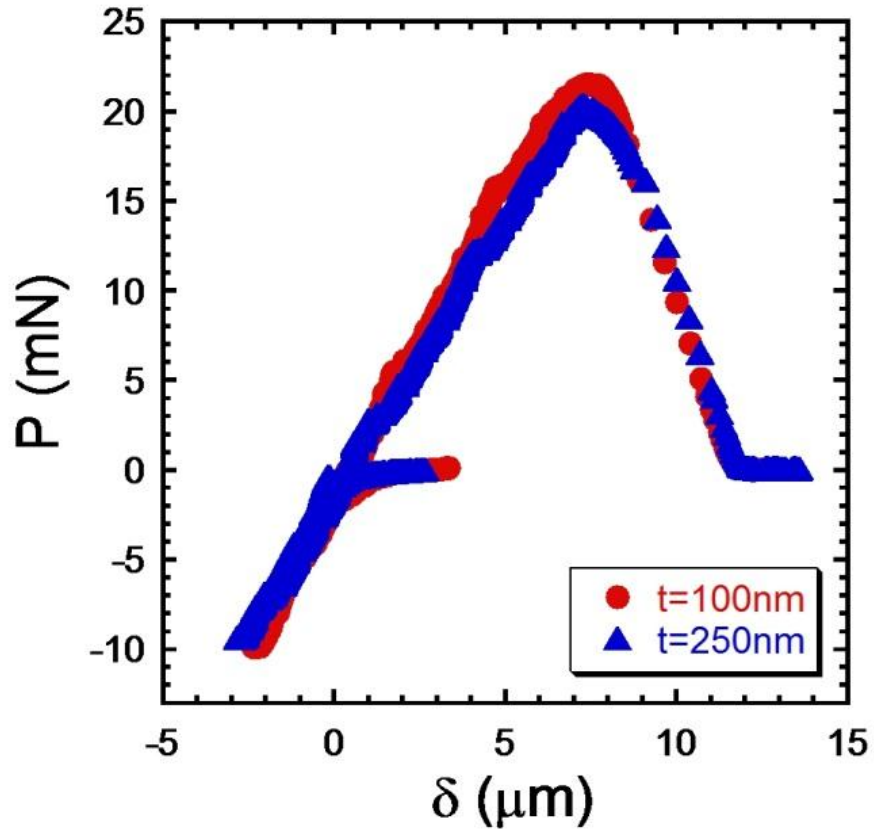
Figure 3.5: Representative force versus displacement plots for smooth-smooth contact. Flat probe contacted a smooth PS film supported on a PDMS substrate for two different film thicknesses.

In order to measure the G_c of the PS-PS interface, we employed the relationship of P_f, $\bar{E}$, and c to G_c:[44]

48

$$G_c = \frac{P_f^2}{8\pi\bar{E}c^3} \qquad (3.3)$$

This equation assumes that at the point of separation, the interface is at thermodynamic equilibrium (implying that the entire interface separates instantaneously at P_f) so that $G=G_c$. The two tests shown in Figure 3.5 yield values of G_c=49mN/m and G_c=44mN/m, respectively.

The plane strain modulus ($\bar{E}_s$) for each substrate is determined independently through contact adhesion measurements on a flat, non-wrinkled portion of the PDMS substrate. In these experiments, $\bar{E}_s$ is calculated from the stiffness ($K=dP/d\delta$) of the elastomer according to classical contact mechanics:[44]

$$\bar{E} = \left(\frac{1}{2c}\right)\frac{\partial P}{\partial \delta} \qquad (3.4)$$

where $\bar{E}$ is the plane strain modulus, related to the Young's modulus, E, and Poisson's ratio, ν, by $\bar{E} = E/(1-\nu^2)$.

3.4 Wrinkle Adhesion Results

The normal adhesion is characterized for a library of wrinkle samples. Figure 3.3 shows the effect of wavelength on the force versus displacement history for typical contact adhesion measurements of wrinkled surfaces.[55] Here, the aspect ratio is held fixed while wrinkle wavelengths are changed, allowing a direct comparison of wrinkles which are geometrically similar. From these tests, specific information about the sample stiffness, G_c, and P_c can be determined. In this study, the principle metric employed is the separation force. For the tests in Figure 3.3, all samples are created using the same processing velocity (V) to yield wrinkles that have the same aspect ratio with various wavelengths.

Figure 3.6a shows the adhesive behavior of samples created with the same film on the same PDMS substrate but cast at different velocities. Thus, all three samples have the same wavelength but varied amplitudes. The lowest amplitude wrinkles have the highest separation force. The contact images captured for each of the samples can be seen in Figure 3.6b and provide some insight into the changes. As the amplitude increases, the contact and separation mechanism of the wrinkles changes. For the low amplitude wrinkles, the crests of each wrinkle come into contact and many of the troughs also contact the probe surface. Upon separation, these lower aspect ratio wrinkles separate in a more concerted way from the probe resulting in an overall greater P_c value. However, for the two higher amplitude wrinkles, the contact with the probe is formed only with the top of each wrinkle and the width of each individual contact line ($2a$) grows and decreases in a less coupled manner. The higher magnification images in Figure 3.6b for the higher amplitude samples show these narrower contact lines.

In general, the separation force, P_c, decreases with increasing wrinkle wavelength for a set aspect ratio (b/λ) (Figure 3.7a). P_c also scales inversely with wrinkle amplitude for a given wavelength (Figure 3.7b). Changes in both b and λ are shown to have a significant impact on the measured adherence force; however, the controlling balance between wrinkle geometry and materials properties is not evident.
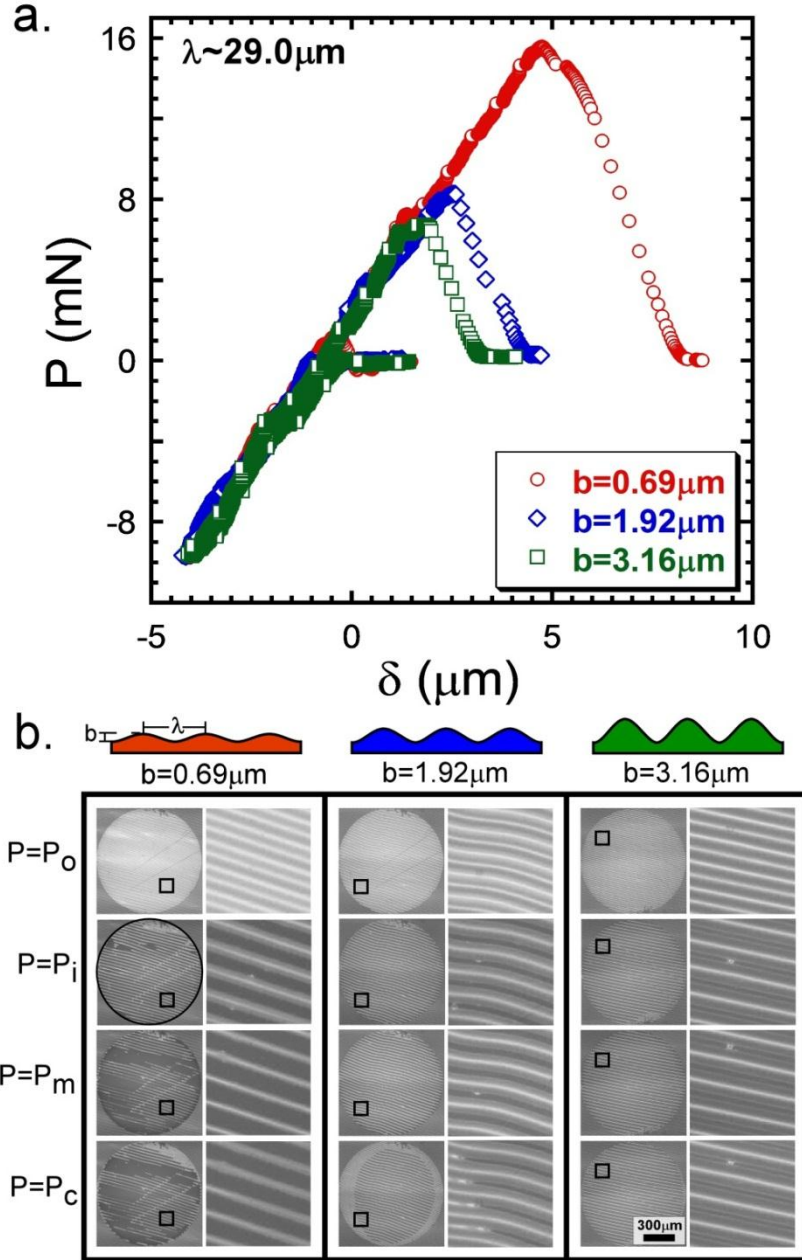
Figure 3.6: Wrinkle adhesion amplitude effects. Varied amplitudes (*b*) at a constant wavelength (λ~29μm).[55] (a) Typical force versus displacement curves for various amplitude wrinkled surfaces during adhesion testing where *P*<0 is compression. (b) Optical micrograph contact images over the course of a test for various amplitude wrinkled surfaces. The circle in each low magnification image is the cylindrical probe face (radius *c*=0.50mm) and the black circle outline in the *P*=P_i image for *b*=0.69μm is added as a guide to the eye. Higher magnification images are 125x125μm. For amplitudes of 1.92μm and 3.16μm only the darkest lines in the insets are areas in contact with the probe. The intermediate gray regions are a result of optical effects of imaging the sides of each wrinkle. Used with permission: Soft Mat. 2011.
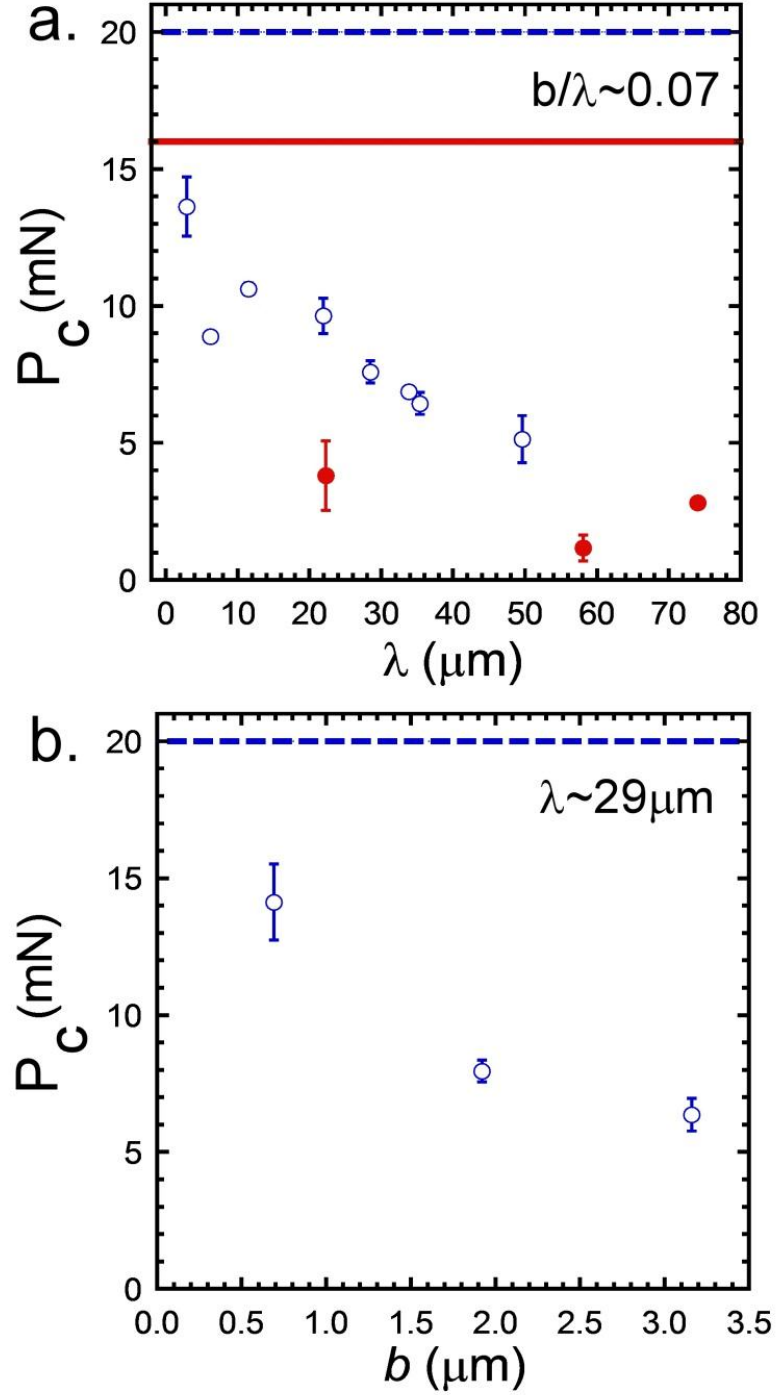
Figure 3.7: Wrinkle adhesion wavelength effects.[55] (a) Separation force as a function of wrinkle wavelength where $\bar{E}_s = 1.25MPa$ (●) and $\bar{E}_s = 2.00MPa$ (○) for a constant aspect ratio of $b/\lambda \sim 0.07$.[55] (b) Separation force as a function of wrinkle amplitude for a fixed wavelength of $\lambda \sim 29\mu m$. The lines represent the separation forces for a flat substrate with a modulus of $\bar{E}_s = 1.25MPa$ (solid line) and $\bar{E}_s = 2.00MPa$ (dashed line). Used with permission: Soft Mat. 2011.

3.4.1 Stiffness Effects

The thickness of the glassy thin film could lead to changes in the effective stiffness (K) of these bilayer systems, possibly changing the separation force for the flat probe contact adhesion experiments. To address this possibility, the stiffness of each surface is determined experimentally. Using the force versus displacement results obtained from each adhesion test, the slope of the compressive region is used to measure the stiffness: $K=dP/d\delta$. Figure 3.8a shows the relationship between the film thickness and the measured stiffness. Over the range of thin film thicknesses used in our adhesion measurements, the stiffness is independent of film thickness. Additionally, in Figure 3.8b it can be seen that there is no discernible trend between the stiffness and wavelength of the wrinkled surfaces for a constant wrinkle aspect ratio (b/λ~0.07) meaning that the geometric features are not impacting the measured system stiffness.
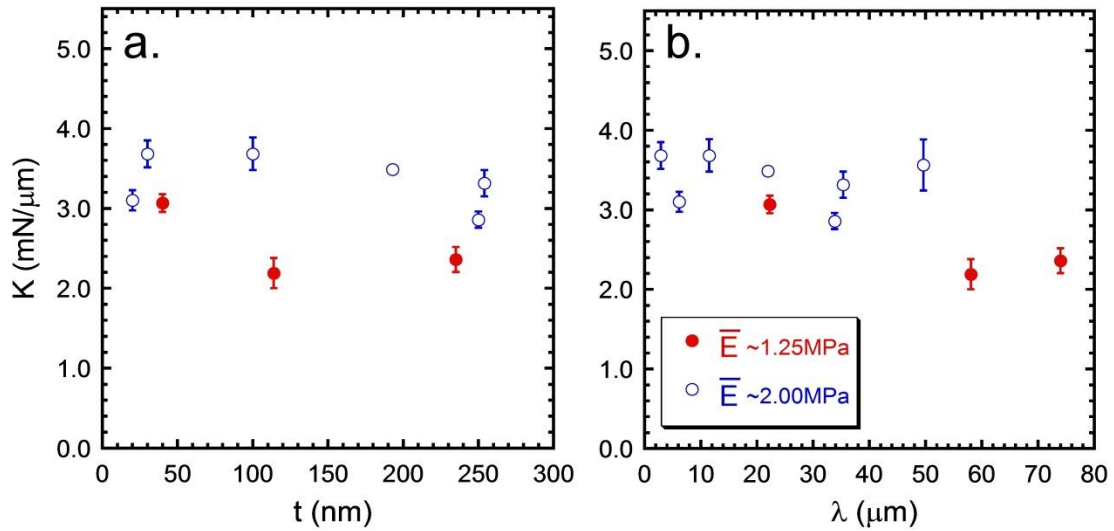
Figure 3.8: Stiffness effects. The stiffness (K) values obtained experimentally through adhesion testing for various wrinkled substrates. Stiffness as a function of (a) thickness (t) and (b) wavelength (λ) for wrinkles with a constant aspect ratio of b/λ~0.07.

The independence of K with the film thickness can be explained by contact mechanics arguments of bilayer or composite systems.[71–73] It has been shown that a stiff, thin layer on top of a soft substrate does not impact the effective modulus of the system if the contact area or probe dimensions are much larger than the stiff layer thickness. For the systems tested here, $10^{-5} < t/c < 10^{-4}$ for all PS films. Therefore, the expected stiffness independence with thickness is verified.

3.5 Discussion

To predict the separation force (P_c) of a wrinkled surface as a function of wrinkle geometry (b and λ) and materials properties ($\bar{E}_s$ and G_c), the surface is considered as an array of aligned cylinders acting simultaneously but independently on the probe face. This total separation force can be modeled as a summation of the individual separation forces per unit length ($\bar{P}_i$) exerted by each wrinkle:

$$P_c \sim \sum_{i=1}^{n} \bar{P}_i l_i \qquad (3.5)$$

where l_i is the length of an individual wrinkle. To determine the appropriate scaling for $\bar{P}_i$, two possible contact separation mechanisms were considered.

First, the contact of a long cylinder with a flat surface is considered in the context of scaling for $\bar{P}_i$. As Barquins proposed[45] and Chaudhury has confirmed experimentally,[47] the separation force per unit length for a long cylinder ($\bar{P}_c^{cyl}$) is:

$$\bar{P}_c^{cyl} = 3 \left(\frac{\pi \bar{E} G_c^2 R}{16} \right)^{\frac{1}{3}} \qquad (3.6)$$

where R is the radius of curvature of the cylinder. For this geometry, the contact persists along the entire length of the cylinder while the contact width decreases as separation

occurs. Equation 3.6 is appropriate when applied to "infinitely" long cylinders contacting "infinitely" laterally extensive probes, where end effects are neglected.

For finite cylinders, end effects play an important role, leading to contact areas that are predominantly elliptical as shown in Chapter 2. Johnson developed a model to describe the separation force of an elliptical contact area through the modification of the well-known relationship for a sphere contacting a flat surface:[44,56]

$$P_c = \left(\frac{\bar{E} G_c A_c^{3/2}}{\sqrt{\pi}} \right)^{\frac{1}{2}} \qquad (3.7)$$

where the contact area of an ellipse at separation is $A_c = \pi a_c c$. In our wrinkle system, the contact width ($2a$) of each wrinkle is consistent with the contact width of a cylinder predicted by Barquins. Therefore, the half contact width of each wrinkle at the point of separation is:[45]

$$a_c = \left(\frac{2 G_c R^2}{\pi \bar{E}} \right)^{\frac{1}{3}} \qquad (3.8)$$

Combining equations 3.7 and 3.8 with the contact area of an ellipsoid at the point of separation (A_c) results in the prediction of the maximum separation force for a finite cylinder:

$$P_c^{ell} = (2\pi \bar{E} G_c^3 R^2)^{\frac{1}{4}} \cdot c^{\frac{3}{4}} \qquad (3.9)$$

To help determine whether the relationships presented as equations 3.6 or 3.9 are more appropriate in the context of a flat circular probe separating from an "infinitely long" cylinder, macro-scale, single cylinder adhesion experiments are conducted. Chapter 2 describes these single short cylinder adhesion experimental results in detail. It is shown that the scaling given in equation 3.9 is consistent with the presented results.

Therefore, utilizing equation 3.9, the separation force of a wrinkled surface can be modeled by considering the surface as an array of independent elliptical contacts acting on the probe. Using the geometry of the wrinkles and testing setup, the P_c for a wrinkled surface can be determined for n wrinkles contacting the probe:

$$P_c \sim n \cdot \frac{P_c^{ell}}{2c} \cdot l_{avg} \qquad (3.10)$$

The value of n is determined by c and λ:

$$n \cong \frac{2c}{\lambda} \qquad (3.11)$$

To account for the variations in length of the wrinkles resulting from the circular face of the flat probe, P_c^{ell} is normalized by the probe diameter and multiplied by the average length of the wrinkles (l_{avg}) contacting the probe:

$$l_{avg} \cong \frac{\pi c^2}{2c} \cong \frac{\pi c}{2} \qquad (3.12)$$

Additionally, the radius of curvature (R) of each wrinkle can be estimated from the measured wavelength (λ) and amplitude (b) of each array of wrinkles, such that:

$$R \approx \frac{\lambda^2}{2\pi^2 b} \qquad (3.13)$$

for small strain surface instabilities ($\epsilon \leq 0.10$). The relationship between R, b and λ has been published previously[30] and confirmed for the wrinkles characterized here by measuring the radius of curvature of several wrinkles using optical profilometry.

Application of these geometric corrections to the scaling presented in equation 3.10 leads to a prediction for the separation force of a wrinkled surface:[55]

$$P_c = \left(\frac{\pi \bar{E} G_c^3 c^7}{2^5 b^2}\right)^{\frac{1}{4}} = \left(\frac{\pi \bar{E} G_c^3 c^7}{2^5 \lambda^2 \epsilon}\right)^{\frac{1}{4}} \qquad (3.14)$$

From this relationship it can be seen that P_c is a function of materials properties (G_c and $\bar{E}$), wrinkle geometry (b and λ), and probe size (c). Equation 3.14 is presented in two ways, recalling the relationship between λ and b through the strain given in equation 3.2.

A summary of the wrinkle adhesion separation force results is presented in Figure 3.9a. The linear fit applied to the data demonstrates that the prediction for P_c shown in equation 3.14 is a good descriptor of the separation force for the wrinkled surfaces tested. The slope of this line yields a G_c value for a PS-PS interface of 131 mN/m, which is close to the reported and measured value of 45 mN/m considering the approximations used to develop the scaling relationship.[70]

Wrinkles or patterns are used to modify the adhesion behavior of a surface compared with a "flat" surface; therefore, it is informative to normalize the wrinkle separation force (P_c) by the separation force of a flat probe on a flat sample (P_f). The separation force relationship for a flat-on-flat contact geometry is:[74]

$$P_f = (8\pi \bar{E} G_c c^3)^{\frac{1}{2}} \qquad (3.15)$$

Combining this relationship with equation 3.14:

$$\frac{P_c}{P_f} \cong \left(\frac{G_c c}{2^{11} \pi \bar{E} b^2}\right)^{\frac{1}{4}} = 0.112 \left(\frac{G_c}{\bar{E} b}\right)^{\frac{1}{4}} \left(\frac{c}{b}\right)^{\frac{1}{4}} \qquad (3.16)$$

The application of this relatively simple scaling to the wrinkled systems measured here can be seen in Figure 3.9b. When plotted in this manner, the data falls onto a line, indicating good agreement between the measured values and our scaling relationship. It can also be seen that achieving enhancement of adhesion ($P_c/P_f > 1$) is dependent on the probe size relative to the wrinkle dimensions as well as the materials-defined length scale
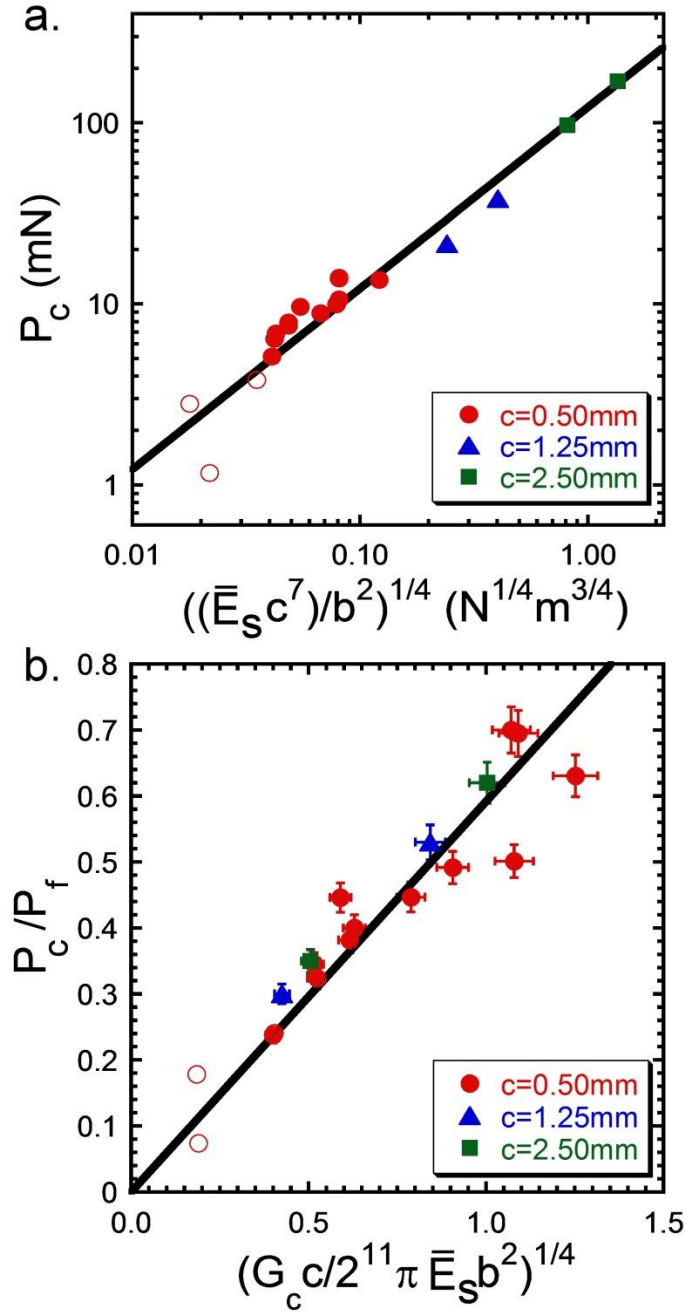
Figure 3.9: Wrinkle adhesion scaling relationships. (a) Separation force as a function of materials properties and geometry.[55] The line is a linear fit to the data. (b) Relationship of normalized adhesion force with the scaling relationship for various probe radii (*c*). The line is added to the figure only as a guide to the eye and is not meant to represent a mathematical fit. For both plots, the open symbols represent substrates with $\bar{E}_s = 1.25 MPa$ while solid symbols are for $\bar{E}_s = 2.00 MPa$. Used with permission: Soft Mat. 2011.

given by $G_c/\bar{E}$. Additionally, a similar dependence on materials properties and amplitude has recently been shown to work for randomly oriented wrinkles tested with a spherical indenter. The only differences in this case arise from the testing geometry.[40]

3.6 **Conclusions**

In this chapter, we demonstrate that both the wavelength and amplitude of a wrinkled surface impact the adhesive properties, specifically the separation force. To investigate the two parameters independently, a novel sample preparation technique is employed. This same technique allows for the removal of residual stress stored in the elastically buckled surfaces of our samples by crosslinking the substrate after wrinkle formation. Furthermore, materials with well-characterized surface and bulk properties are used to create model examples for understanding the contact adhesion of interfaces between flat surfaces and surfaces with aligned wrinkles.

The single cylinder tests with finite flat probes presented in Chapter 2 and the resulting model for the adhesion of finite length cylinders have been utilized in the development of the separation force equation 3.14 in this chapter. The significance of the work presented in this chapter lies in the development of a model wrinkle system that allows contact mechanics and adhesion theory to be applied to a wrinkled surface. By understanding the impact of wrinkle geometry on the separation mechanisms, new material systems can be engineered with specifically-tuned adhesive properties. The relationships developed here for a model system will be applied to a much more realistic system in Chapter 4. Wrinkle adhesion effects on confined viscoelastic films will be explored. Additionally, the analysis presented here could enable natural adhesive systems to be more easily studied and compared.

CHAPTER 4

WRINKLE ADHESION IN ELASTIC AND VISCOELASTIC FILMS

4.1 Abstract

The adhesive properties of a surface can be greatly affected simply by wrinkling its surface. Here, we show the importance of selecting the wrinkle geometry length scales (amplitude and wavelength) that complement the materials-determined length scale related to the adhesion energy and modulus (G_c/E). A rigid cylindrical probe patterned with aligned wrinkles ranging in amplitude from 0.5 to 5.0μm with a fixed aspect ratio of 0.1 is used to characterize the adhesion of soft films of varying crosslink densities fabricated from smooth polydimethyl siloxane (PDMS). The soft films have an average thickness of 240μm while the average probe radius is 1mm, making finite size effects significant for our contact geometry. The crosslinker concentration used to form the PDMS layers is varied to determine the impact of viscoelastic character on wrinkled surface adhesion. Separation strength and work of adhesion are presented for each crosslinker concentration with testing rates ranging over three orders of magnitude. A scaling relationship derived from contact mechanics theory is a fairly good fit to our wrinkle adhesion results for well crosslinked films. However, there is no discernible impact of wrinkled surface topography on the adhesion of more viscoelastic films.

4.2 Introduction

In the adhesion of tapes and reusable adhesives, surface roughness plays an important role in dictating the force and energy required to separate an interface bound by intermolecular forces.[75–78] To develop materials with reusable, reliable adhesive

properties, wrinkles offer an attractive option for producing well-defined surface roughness. This concept has been demonstrated for wrinkled elastic surfaces, allowing the role of periodic surface roughness to be determined. However, the role of viscoelasticity on the adhesion of a thin, soft layer to a rigid surface in the presence of wrinkle topography has yet to be determined and must be further investigated.

Reversible adhesives function by two distinct separation phenomena: (1) intermolecular forces acting between the two contacting surfaces (i.e. Van der Waals) and (2) viscous dissipation[79] that takes advantage of geometric confinement. A surface's overall adhesive strength or force required to separate an interface is closely related to the strength of intermolecular interactions[80] while the work of adhesion or energy required for separation generally scales with the viscoelastic character of the two contacting materials.[81,82] The balance and optimization of these two parameters will be further investigated here to determine contact scenarios which allow for an increase in both of these critical adhesion metrics.

Wrinkles, a spontaneously forming periodic surface roughness, are a facile way to control both separation force and energy. This control is attributed to the ability to dictate λ and b. The mechanics governing the formation of wrinkles is well understood.[11,22] Several wrinkling techniques allow independently tuned wavelengths and aspect ratios as well as the ability to rapidly pattern large areas.[19,23] Taking advantage of this elastic surface buckling instability, surface topography can easily be applied to various materials through wrinkling techniques and subsequent molding steps.

Surface topography alters the separation mechanism of an interface by introducing defects from which cracks initiate.[35] By altering the number and shapes of

these crack nucleation sites, the amount of energy required to separate the interface can be affected.[83] The contributions of viscoelasticity and surface roughness acting in concert to impact adhesion are investigated. Topography may control local separation rates, thus altering the energy of adhesion by changing the viscoelastic response of the soft material near the crack tip. The degree to which surface topography affects adhesion (whether increasing or decreasing separation strength and adhesion energy relative to those of smooth analogs) is a function of materials properties as well as the size of the surface features.[52,84]

In this chapter, the objective is to understand the impact on adhesion of surface roughness of various elastic and viscoelastic materials in confined geometries. The viscoelastic properties and surface roughness length scales that contribute to enhanced and decreased adhesion of a rigid, wrinkled surface contacting a soft adhesive layer are identified.

4.3 **Experimental Approach**

We investigate the impact of wrinkle feature size and viscoelasticity on the adhesion of a compliant layer to a rigid material. Specifically, the adhesive impact of rigid surface wrinkles with amplitudes ranging from 0.5 to 5.0μm and a constant aspect ratio of approximately 0.1 contacting a smooth, thin adhesive layer is measured. The modulus and viscoelastic properties of the thin adhesive substrate are varied by changing the degree of crosslinking through different crosslinker to prepolymer ratios (2 to 10wt%). Controlling the crosslinker percentage adjusts the film modulus from 0.02 to 2.00 MPa and impacts the viscoelastic nature of the film. For all adhesion tests the force,

displacement and contact area are recorded simultaneously as the surfaces are brought into contact and subsequently separated.

4.3.1 Fabrication of Probes

Master wrinkle surfaces are formed utilizing previously reported methods that allow the wavelength to be tuned independently of the wrinkle aspect ratio.[26,55] To eliminate concerns of residual stresses stored in the buckled surfaces affecting the mechanics of separation, master wrinkle surfaces are replicated with a rigid epoxy. This molding step also allows multiple rigid probes to be fabricated with identical surface features. The topography of these wrinkled surfaces is measured using an optical profilometer (Zygo NewView 7300 and Veeco Wyko NT3300).

Rigid cylindrical probes with a wrinkled surface on one end are formed utilizing a novel capillary bridge technique that allows the height and radius of each probe to be controlled. Probes are fabricated from a UV-curable adhesive (Norland Optical Adhesive, NOA).
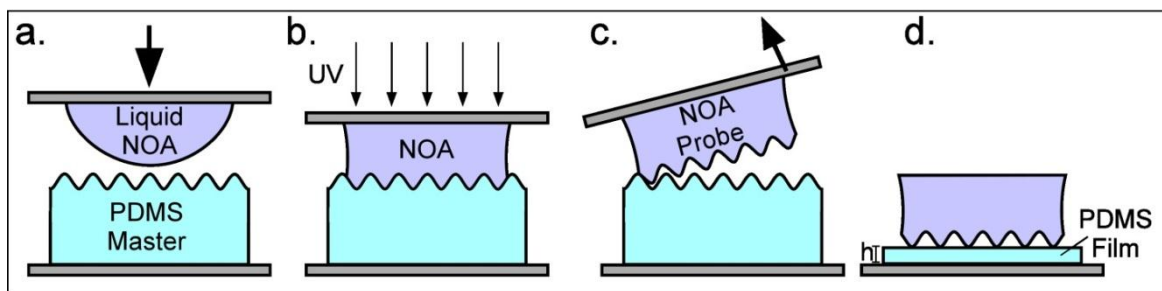
Figure 4.1: Schematic of rigid wrinkled probe fabrication process.

Figure 4.1 contains a schematic of the process used to fabricate rigid cylindrical probes. An uncured drop of liquid NOA with an approximate volume of 0.3 mL is placed on a 1cm^2 glass slide and suspended dropside-down over the master wrinkle surface to be replicated. Using a custom-built vice, the drop is lowered towards the master until contact

between the drop and the surface occurs and a cylindrical capillary bridge of liquid NOA is formed.[85] The height of the glass slide is adjusted until the desired probe radius is achieved (c~1mm).

The NOA is then exposed to ultraviolet (UV) light (Jelight, 30mW/mm^2) for 4 minutes to crosslink the epoxy. The interface between the crosslinked NOA probe and the wrinkled master is separated at a velocity of approximately 1mm/s at a 30° peel angle and
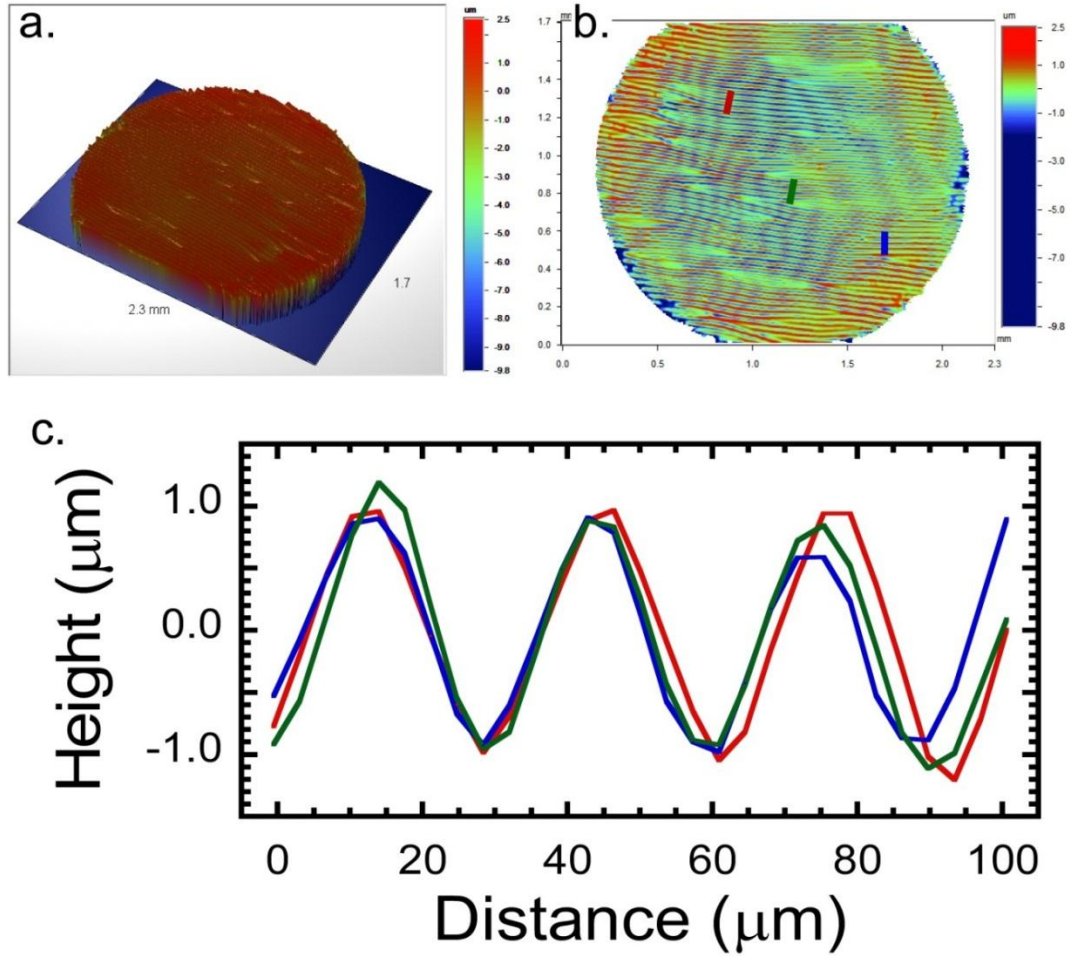
Figure 4.2: Representative NOA wrinkled probe characterized with optical profilometry. (a) Three dimensional plot of probe surface. (b) Two dimensional representation of same probe as in (a). Dark blue regions are imaging artifacts rather than true defects on probe surface. Lateral dimensions of both scans are 1.7x2.3mm and the z-scale is -9.8 to 2.5μm. (c) Surface profiles of wrinkles corresponding to colored lines marked in (b). illustrating uniformity of wrinkles over entire probe face.

the probe is exposed to UV for an additional 2-4 minutes to ensure completion of the epoxy crosslinking process. This amount of UV exposure far exceeds the exposure time suggested by the manufacturer but is necessary to ensure perfect replication of the micron and submicron surface features and eliminate small scale surface roughness. The fidelity of the replicated rigid wrinkle probes to the wrinkled master is verified with optical profilometry (Veeco Wyko NT3300) and the profile of the wrinkles measured directly as shown in Figures 4.2 and 4.3c.
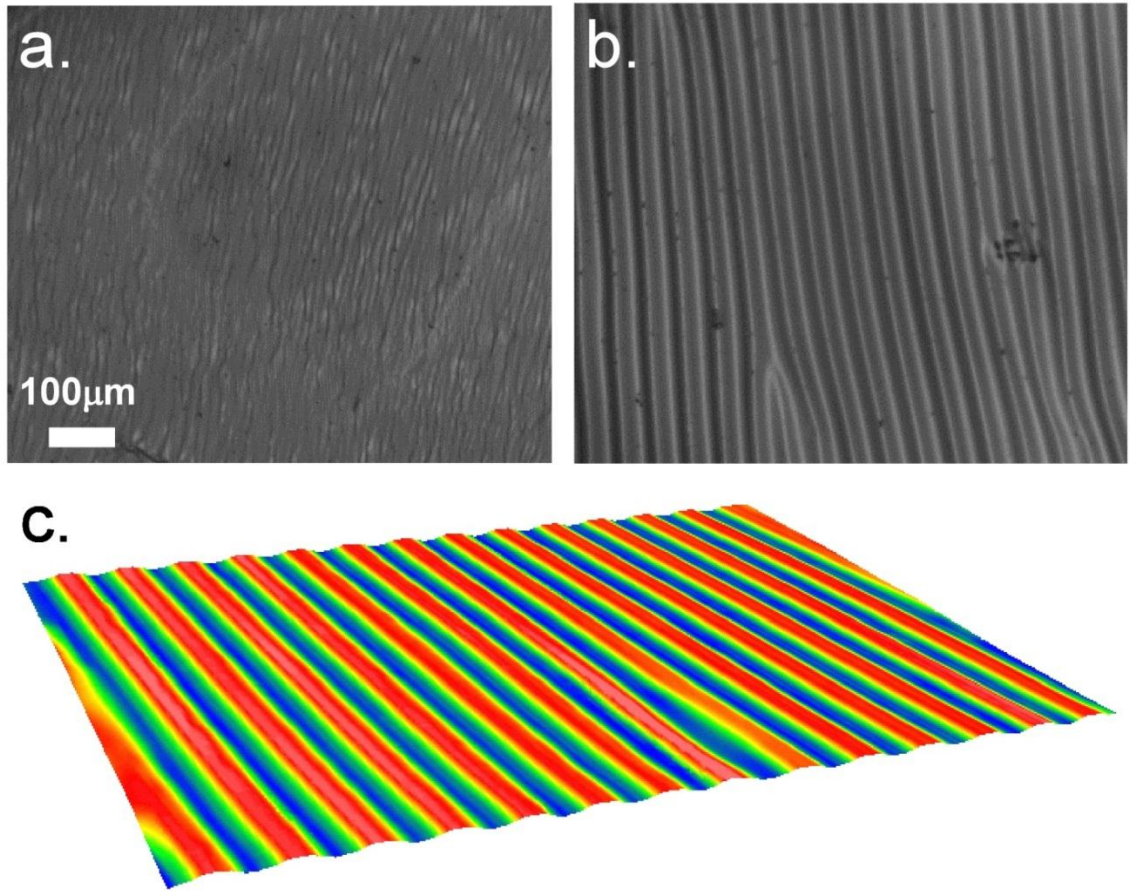
Figure 4.3: Wrinkle pattern topography. (a-b) Optical micrographs of rigid wrinkle surfaces for b=0.5μm (a) and b=5.0μm (b). Scale bar refers to a. and b. (c) Optical profilometer scan of surface from a. illustrating the aspect ratio (b/λ~0.1) of the wrinkles. The lateral dimensions are 53 x 71μm and the peak to trough amplitude is 0.48μm.

4.3.2 Fabrication of PDMS Films

The viscoelasticity of the soft, "adhesive" layer is controlled by varying the concentration of crosslinker added to a two part rubber system. By changing the amount of crosslinking agent available during the curing of the rubber, the molecular weight between crosslinks is altered, affecting the viscoelasticity and modulus of each film. Previous works have thoroughly characterized the rheological properties[86] of the elastomers used in these adhesion experiments as shown in Figure 4.4.
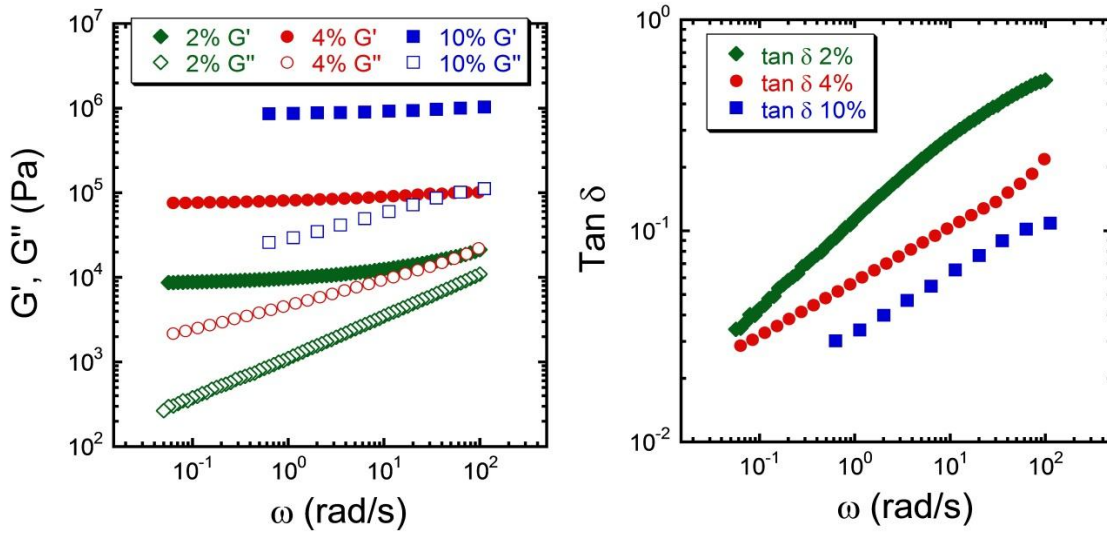
Figure 4.4: Rheological response of Dow Sylgard PDMS with various concentrations of crosslinker. Storage, G', loss, G", moduli , and tan δ with angular frequency, ω for 2 and 4% data is gathered with a cone and plate rheometer while 10% data is measured using dynamic mechanical analysis (DMA) techniques.[86] Reproduced with permission: J. Nase, Ph.D. Dissertation, UPMC, 2009.

Smooth, soft films of polydimethyl siloxane (PDMS) (Dow Corning Sylgard 184) are formed on glass slides and contacted with rigid wrinkled probes. Three compositions of PDMS (2, 4, and 10wt% crosslinker in prepolymer) are mixed and degassed in a reduced pressure environment for 15 minutes. Films are cast by applying the uncured PDMS to a clean glass slide using a doctor blade and a 400μm spacer to ensure uniform

film thickness. Cast films are immediately placed in an oven under vacuum for 5 hours at 70°C.

Upon removal from the oven, the films cool for several hours before the film thickness is characterized with a pneumatic thickness measurement device. The final cured films range in thickness from 170 to 357μm with an average thickness of 240μm. To provide a smooth, clean surface for adhesion experiments, the PDMS films are removed from the slide on which they are cast and inverted onto a freshly cleaned glass slide just prior to testing.

4.3.3   Adhesion Experiments

The normal adhesion of rigid wrinkled surfaces in contact with soft, smooth adhesive films is characterized using a custom-built contact adhesion testing apparatus.[74,87] A schematic of the experimental setup is shown in Figure 4.5.
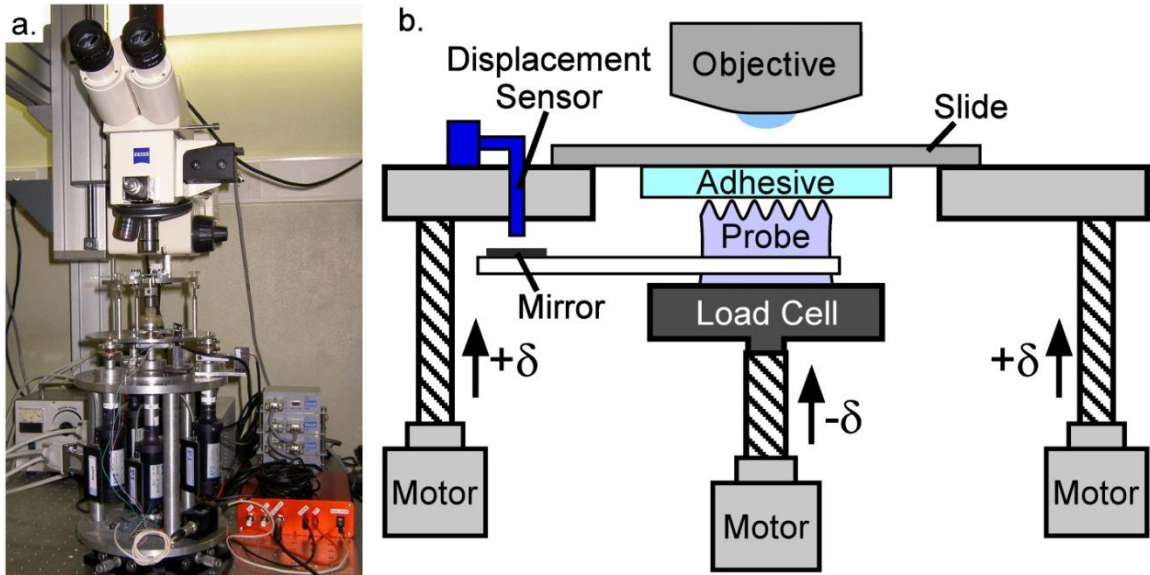
Figure.4.5: Contact adhesion setup at ESPCI used for experiments described here. (a) Image of actual adhesion testing device (Image courtesy David Martina). (b) Schematic of adhesion testing device.

Over the course of a test, a rigid cylindrical probe is brought into contact with a soft film at a fixed displacement rate, V (central motor displacement) until full contact of wrinkle peaks and troughs is achieved with the flat film. This maximum compressive force is held for a 1 second dwell time. The displacement direction is then reversed until full separation occurs (coordinated motion of outer motors). A fiber optic displacement sensor monitors the vertical displacement of the probe while a load cell attached to the probe records normal forces applied to the interface. Throughout the test, the contact area is imaged by an optical microscope (Zeiss Axio Vario). For our experiments, the wrinkle feature size, adhesive layer crosslinker concentration, and displacement rate are varied systematically.

The compliance (displacement per unit force, $C = \partial\delta/\partial P$) of the experimental setup impacts normal contact adhesion experimental results.[88] Therefore, prior to each set of experiments, control tests are conducted to correct for instrument compliance. A smooth rigid probe (c~1.0mm) is brought into contact with a clean glass slide and the force and displacement are measured. On average, for the experimental setup C=0.8 μm/N, which is extremely low relative to the compliance values observed for our material system. Though low, this machine compliance is accounted for in the analysis of the data obtained for each adhesion test using a custom macro (Igor Pro 5.0).

An additional set of calibration tests is performed by measuring the adhesion of the same smooth, rigid probe in contact with each smooth PDMS film (2, 4, and 10wt% crosslinker) to establish the adhesive properties of a smooth interface for each film. The values measured on the smooth probes are used to analyze the wrinkle adhesion results and determine whether or not the wrinkled topography of the rigid surface has an effect

on adhesion. The separation stress, σ_s and work of adhesion, w_{adh} of these smooth, adhesive interfaces are provided in Figure 4.6 for 4% and 10% crosslinker films as a function of displacement rate.
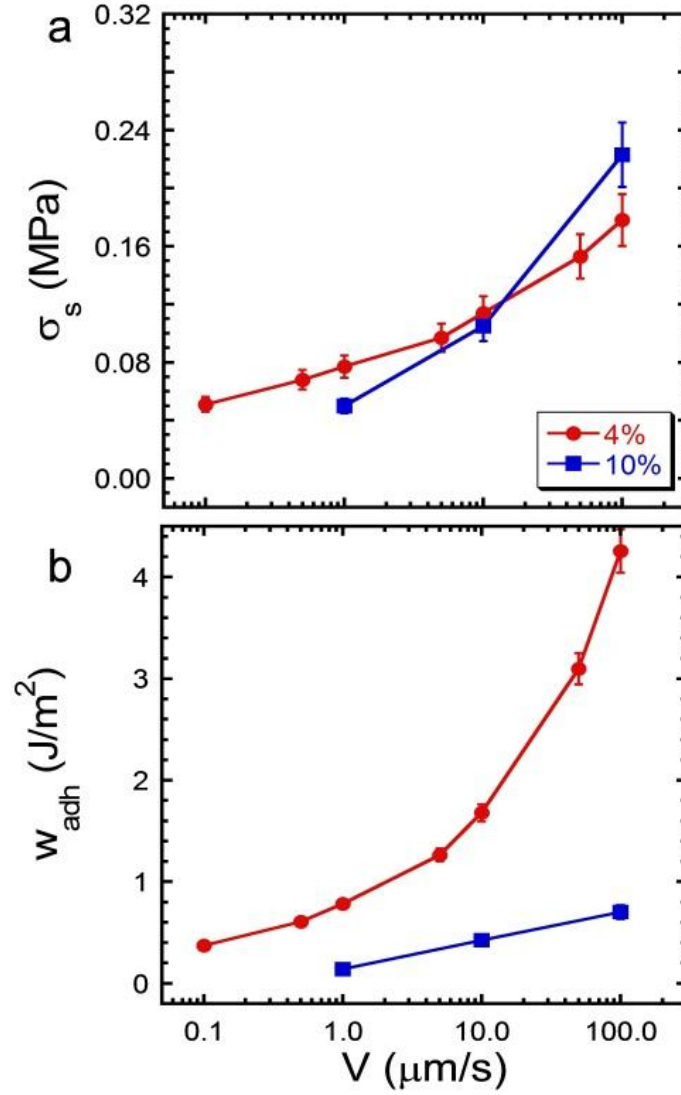
Figure 4.6: Separation stress and work of adhesion as a function of testing rate for smooth interface. Tests performed with rigid probes on smooth adhesive films for 4 and 10wt% PDMS.

A summary of the experimental parameters and their ranges is provided in Table 4.1:

Characteristic	Minimum	Maximum
Wavelength (λ, μm)	5.0	48.0
Amplitude (b, μm)	0.47	4.20
Aspect ratio (b/λ)	0.08	0.13
Probe radius (c, mm)	0.96	1.18
Substrate thickness (h, μm)	170	357
Substrate modulus ($\bar{E}$, MPa)	0.02	2.20
Crosslinker percentages (x, %)	2	10
Testing velocity (V, μm/s)	0.1	100.0

Table 4.1: Range of experimental variables.

4.3.3.1 Plane Strain Modulus Determination

Contact mechanics is a method which can be used to measure the materials properties of soft polymers. The plane strain modulus ($\bar{E}$) for thick materials can be determined directly through contact adhesion measurements. $\bar{E}$ is calculated from the stiffness ($K=dP/d\delta$) of the elastomer according to classical contact mechanics:

$$\bar{E} = \left(\frac{1}{2c}\right)\frac{\partial P}{\partial \delta}$$

(4.1)

where $\bar{E}$ is related to the Young's modulus, E, and Poisson's ratio, ν, by $\bar{E} = E/(1 - \nu^2)$. Practically, the slope of the compressive portion of the force versus displacement curve obtained during an adhesion test yields this stiffness.

Equation 4.1 is an effective way to measure the modulus of thick samples. However, as the thickness of the soft layer (h) decreases so that $c/h \geq 0.1$, the stiffness of the rigid substrate supporting the soft film must be considered. These "finite size corrections" have been determined,[74,89] allowing the moduli of thin films to be calculated. The c/h ratio for the adhesion experiments presented here range from 3.10 to 5.94, well

within the regime where finite size effects are significant. Compliance, C, is the inverse of stiffness, and can be related to the modulus, *E*, by the bulk compliance of the adhesive layer, C_o, which can be determined by:[52]

$$C_0 = C\left(1 + \left[\frac{0.75}{\left(^C/_h + (^C/_h)^3\right)} + \frac{2.8(1-2v)}{^C/_h}\right]^{-1}\right)$$

(4.2)

where C is the measured compliance.

4.4 Adhesion Results

Normal contact adhesion experiments are conducted with rigid, aligned wrinkles as seen in Figure 4.6 on soft films of varying viscoelasticity. These normal forces as a function of vertical displacement are illustrated in Figure 4.7a for three different wrinkle amplitudes. Negative force values are compressive, while positive force values are tensile or adhesive. The same data is provided in Figure 4.7c with the compressive portion of the curve omitted to magnify the region of interest, specifically the adhesive regime of each test, so that the stark contrast in the adhesive response of the two extreme wrinkle amplitudes can be more easily observed. The peak separation force, P_c, for the smaller amplitude sample is much greater than that of the larger wrinkle feature size.

Similarly, Figure 4.7b shows the relationship between the normal force and displacement measured on adhesive films with varying crosslinker concentrations. All three of these tests are conducted at a fixed displacement rate of $V=1\,\mu m/s$ using the same rigid wrinkled probe (b=0.5μm). For the most highly crosslinked adhesive layer (10%), the peak separation force is higher than for the two more lightly crosslinked materials (2 and 4%).

Figure 4.8 contains a comprehensive summary of the results obtained in this study. As a function of testing displacement rate (V), Figures 4.8a-c show the impact of wrinkle amplitude on the separation strength ($\sigma_s = P_c/\pi c^2$) for the three crosslinker
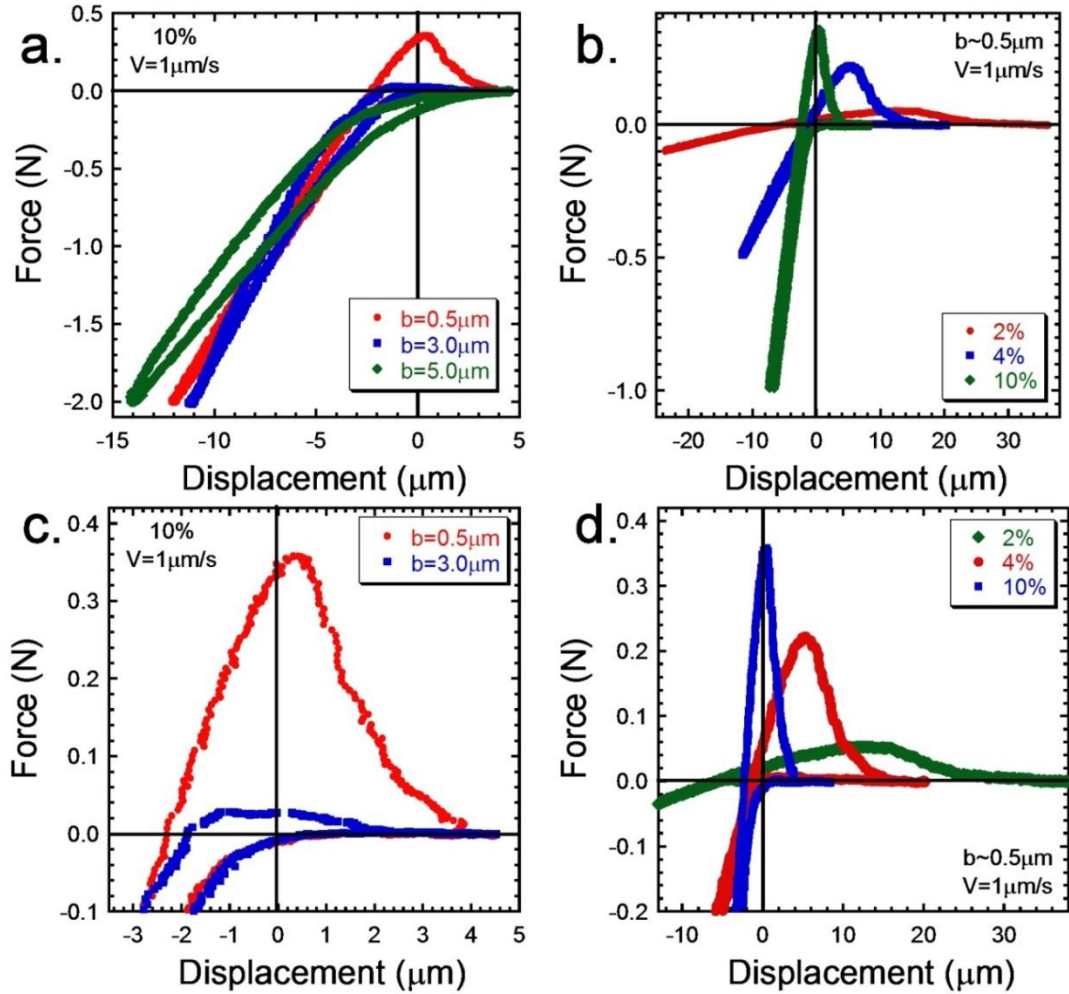
Figure 4.7: Viscoelastic wrinkle adhesion results. (a) Representative force versus displacement curves for three wrinkle amplitudes (b=0.5, 3.0, 5.0μm). Tests are conducted on a 10wt% crosslinker PDMS film with a controlled displacement rate of 1μm/s. (b) Force versus displacement curves for the three crosslinker concentrations studied. Tests are conducted on the same wrinkled surface (b=0.5μm) at a controlled displacement rate of 1μm/s. (c-d) Tensile portions from curves a. and b. showing the adhesive response of various wrinkle amplitudes (c) and various crosslinker ratios (d).

compositions tested. Wrinkle amplitude does not affect the adhesion of the two viscoelastic layers (2% and 4%) but has a dramatic impact on the separation strength of

the most highly crosslinked materials. As shown in previous wrinkle adhesion studies,[30,40,41,55] for the 10% films, wrinkles with small amplitudes require more force to separate the interface than larger amplitude wrinkles.
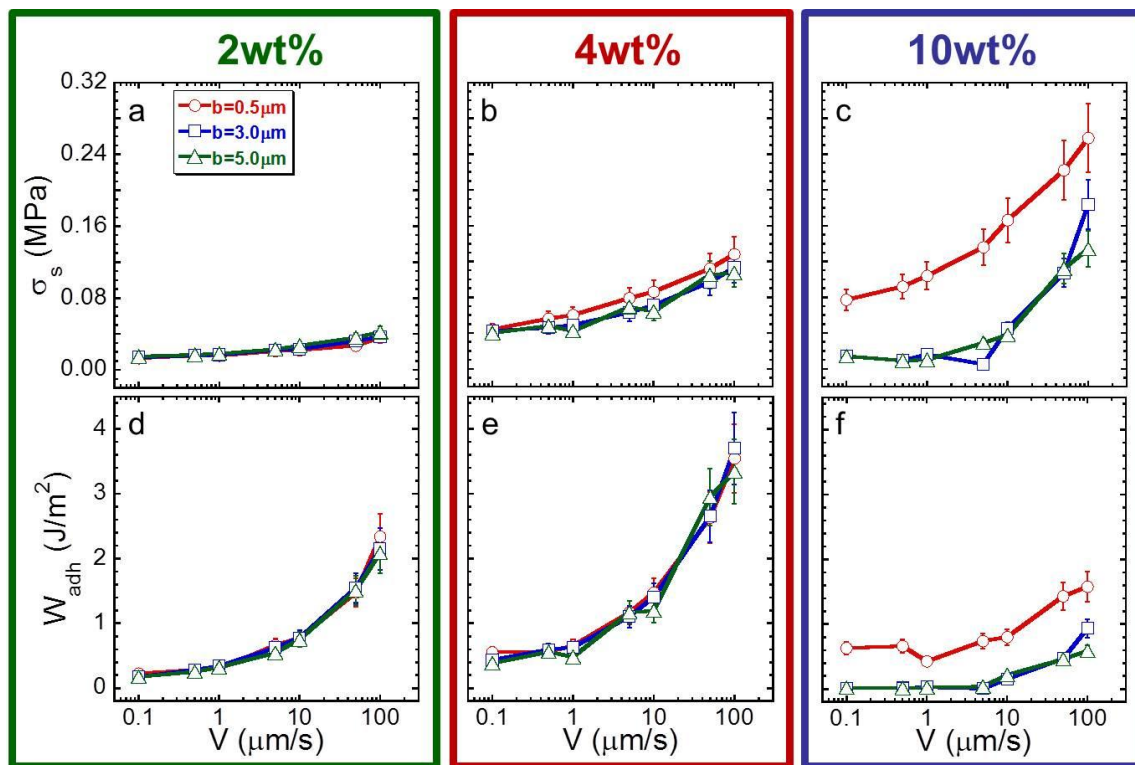
Figure 4.8: Adhesion results as a function of testing velocity. Separation stress, σ_s (a-c) and work of adhesion, w_{adh} (d-f) as a function of velocity for three wrinkle amplitudes (see legend in (a)) for amplitude values). The green and red outlines contain the results for the two more viscoelastic (2 and 4%) adhesives. For these two more lightly crosslinked materials, there is no significant difference in the adhesion metrics for the different wrinkle sizes. The blue outline encompasses the plots for the films with the highest crosslinker concentration (10%) showing a significant difference in the separation stress and work of adhesion for the smallest wrinkles and the two larger size wrinkles.

Through integration of the area under the tensile portion of the force versus displacement curves, a measure of the energy required to separate the interface; the energy of adhesion, U_{adh} is obtained:

$$U_{adh} = \int_0^\delta P \, \partial\delta \qquad (4.3)$$

While the separation force is higher for the most highly crosslinked adhesive film (10%), the more viscoelastic films are more dissipative and require more energy to separate the interface though less force is required as shown in Figures 4.8d-f as a function of normal displacement rate where $w_{adh} = U_{adh}/\pi c^2$. Both the separation force and adhesion energy descriptors are normalized by the projected area of the probe to account for small variations in the size of the rigid probes due to the probe fabrication method described in Section 4.3.1.

As for the separation strength data, w_{adh} is independent of the size of the wrinkled surface features for the two most viscoelastic films. For the more highly crosslinked PDMS film, the work of adhesion is dependent on wrinkle amplitude and is greater for the smallest wrinkles. w_{adh} increases dramatically with increasing testing rate, especially for the more lightly crosslinked layers. However, this phenomenon is independent of surface roughness and due to the viscoelastic response of the material.[34,82]

4.5 Discussion

The two main findings of this work are that (1) wrinkles or surface roughness on the length scales tested here do not significantly impact the adhesive properties for the 2 and 4% crosslinker compositions and (2) for more highly crosslinked systems (10% crosslinker), small wrinkles enhance adhesion while larger wrinkles decrease adhesion as previously reported.[40,55]

4.5.1 Materials Length Scale Relationships

A materials-defined length scale incorporating both the critical strain energy release rate, G_c and modulus, E can be used to describe the distance over which adhesive

forces act between two contacting surfaces.[52] Table 4.2 contains a summary of these materials properties and the length scale, G_c/E for the three PDMS crosslinker ratios tested in this study. This ratio or length scale can be considered the critical displacement needed to separate an interface.

Crosslinker (wt%)	G_c (N/m)	G' (Pa)	G_c/G' (μm)
2	0.195	16156	12.07
4	0.815	96852	8.41
10	0.142	1000000	0.14

Table 4.2: G_c/G' values indicating the materials length scale over which adhesion dominates. The various PDMS crosslinker compositions are given with their respective shear storage modulus, G' values (obtained from rheological experiments).[86]

The G_c values are determined by averaging the results of three adhesion tests performed by contacting a flat, rigid cylindrical punch with a soft, smooth film. These tests are performed at $\partial\delta/\partial t = 0.1\mu m/s$ to approximate thermodynamic equilibrium at which $G_c = w_{adh}$. The most appropriate modulus value to consider for this work is the storage modulus at a testing frequency similar to the normal adhesion testing velocities employed. Thus, the shear storage modulus, G' is obtained from previously reported cone and plate rheology (2 and 4%) and dynamic mechanical testing experiments (10%).[86] To determine the angular frequency, ω which corresponds to the contact adhesion testing velocities employed in this study, the relationship between frequency and strain rate, $\dot{\epsilon}$ is used:[90]

$$\omega \sim \dot{\epsilon} = \frac{\partial\delta/\partial t}{l_o} \qquad (4.4)$$

where l_o is the original length over which the strain is applied. In our case, we have used a vertical displacement in the compressive regime of our test which averaged $l_o \sim 20\mu m$

75

for most tests. G' values corresponding to an angular frequency of $\omega = 0.05$ are used which correspond to an adhesion testing rate of $\partial\delta/\partial t = 1.0\mu m/s$.

4.5.2 Lightly Crosslinked Film Adhesion

For the lightly crosslinked films, the critical displacement required to separate the film from the rigid probe is greater than the amplitudes of the wrinkles tested here. Thus the wrinkles are too small to have a significant impact on the separation mechanism since the damage zone surrounding the crack tip (considering the separation of the interface as a fracture event) is much larger than the wrinkle feature size.

Once the appropriate materials length scale is determined for each crosslinker percentage, a qualitative explanation of the impact of wrinkle topography on adhesion can be developed. It can be seen from Table 4.2 that for the more lightly crosslinked (2% and 4%) PDMS films, G_c/G' is larger than the wrinkle topography ($G_c/G' > b$). For these two materials, adhesive forces act over long distances, leading to a large viscoelastic displacement of the material and masking the effects of the small wrinkle features. The wrinkle topography at the interface is effectively "smoothed out" so that the separation is similar to that of a smooth interface. The entire surface is brought into contact with very little elastic penalty so that topography does not play a role in the separation mechanism.

Wrinkles (more specifically, wrinkles over the range of amplitudes tested here) have no effect on the adhesive properties of the two most viscoelastic materials tested as shown in Figure 4.8. The separation strength and work of adhesion of these lightly crosslinked wrinkled films is commensurate to that of smooth films. Figure 4.9 illustrates this independence of separation strength on wrinkle amplitude for lightly crosslinked films. This plot shows effective separation strengths ($\bar{\sigma}_s = \sigma_s/\bar{E}$) for large and small

76

wrinkles normalized by the effective separation strength of a smooth probe contacting the same smooth film with respect to testing rate. Regardless of testing velocity or feature size, the normalized adhesion values do not deviate substantially from unity for the 4% PDMS films, indicating that there is no change in adhesive properties due to the wrinkle topography.
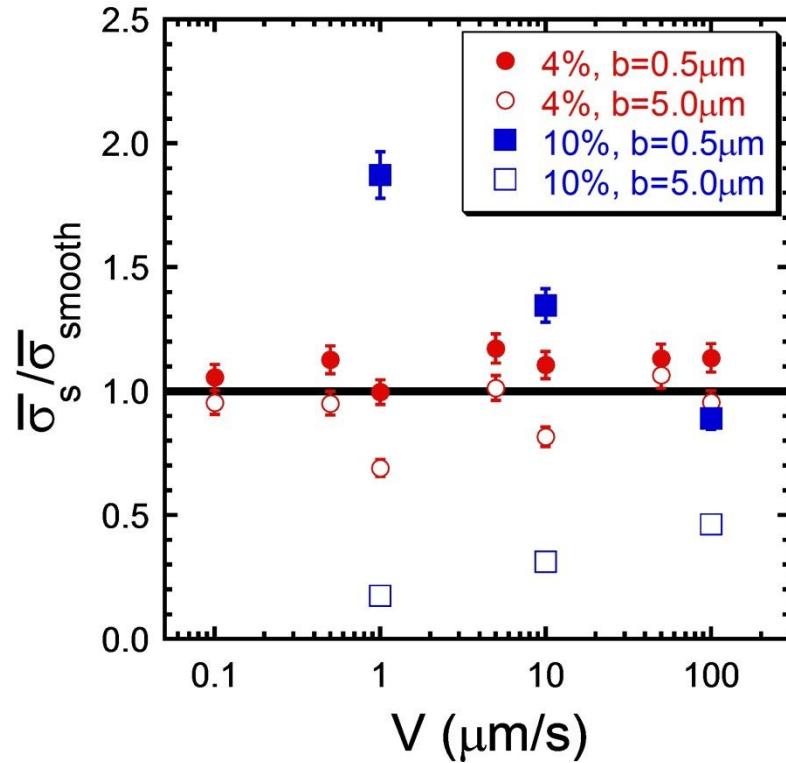
Figure 4.9: Normalized separation stress as a function of testing velocity. The separation stress is normalized by the separation stress of a smooth, non-patterned interface and the effective modulus. The solid black line is drawn at y=1. Values above this line represent adhesion scenarios where the separation stress of the wrinkled interface is greater than that of a smooth interface while values falling below unity indicate a decrease in adhesion relative to smooth. The error bars represent 10% of an average value taken over 5 tests.

The separation mechanism of the lightly crosslinked films is independent of the wrinkled surface roughness. To get a better understanding of the separation process, observations of the contact area over the course of each test are utilized. Figure 4.10 provides contact images that correspond to the maximum separation force. The separation
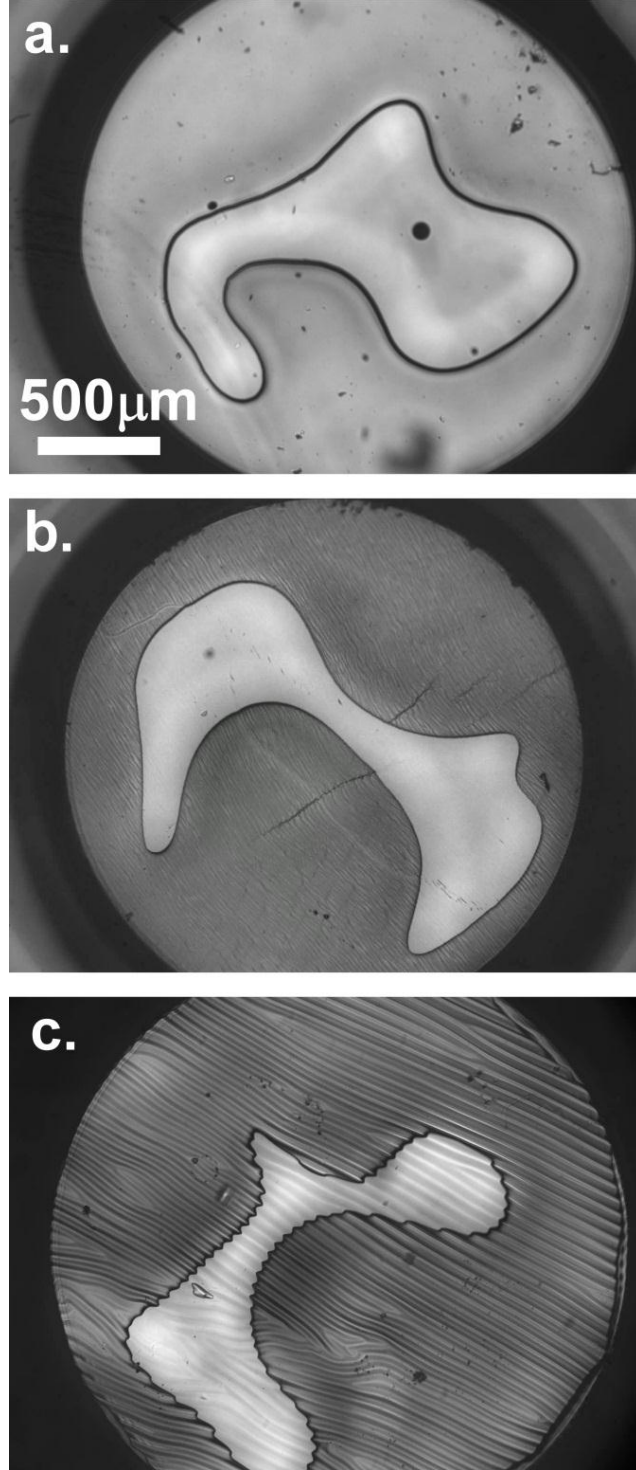
Figure 4.10: Contact images at P_c for 4wt% PDMS films on various rigid probe topographies. Films tested with rigid probes with (a) smooth, (b) b=0.5μm wrinkles, and (c) b=5.0μm wrinkles. All tests are performed at V=1μm/s and the lightest areas in the center of each image correspond to the portion of the probe in contact with the film surface. The scale bar in (a) applies to all three images.

mechanisms are all qualitatively similar for the 4% crosslinker PDMS for smooth (4.10a), small wrinkles (4.10b), and large wrinkles (4.10c). It should be noted that the contact line or perimeter of the contact on the large wrinkles appears jagged, indicating the interface is conforming to the peaks and troughs of the wrinkles. However, this effective increase in the length of the contact line is negligible relative to the bulk separation mechanism of the interface.

4.5.3 Fully Crosslinked Films Adhesion

For the most highly crosslinked (10%) PDMS film, $G_c/G' < b$. Thus, adhesion is not screened or "smoothed out" as for the more lightly crosslinked interfaces and topography alters the separation of the interface. Our results, most clearly seen in Figure 4.13b, lend credence to this assertion and illustrate the inverse dependence of separation strength on wrinkle amplitude.

In direct contrast to the wrinkle-independent adhesive response of lightly crosslinked films shown in Section 4.5.2, the adhesion of the most highly crosslinked film is greatly affected by wrinkled surface topography as shown in Figure 4.9. The normalized separation strength varies as a function of testing displacement rate and wrinkle amplitude. The effect of wrinkle amplitude is more pronounced at very slow displacement rates. The more quickly the interface is separated, the closer the separation stress is to that of a smooth interface.

For the largest wrinkles tested (b=5.0μm), the separation stress is reduced relative to a smooth surface. Alternatively, the smallest wrinkles (b=0.5μm) showed a marked increase in the separation stress relative to that of the smooth interface. More insight into these wrinkle amplitude effects can be obtained by examining the contact images
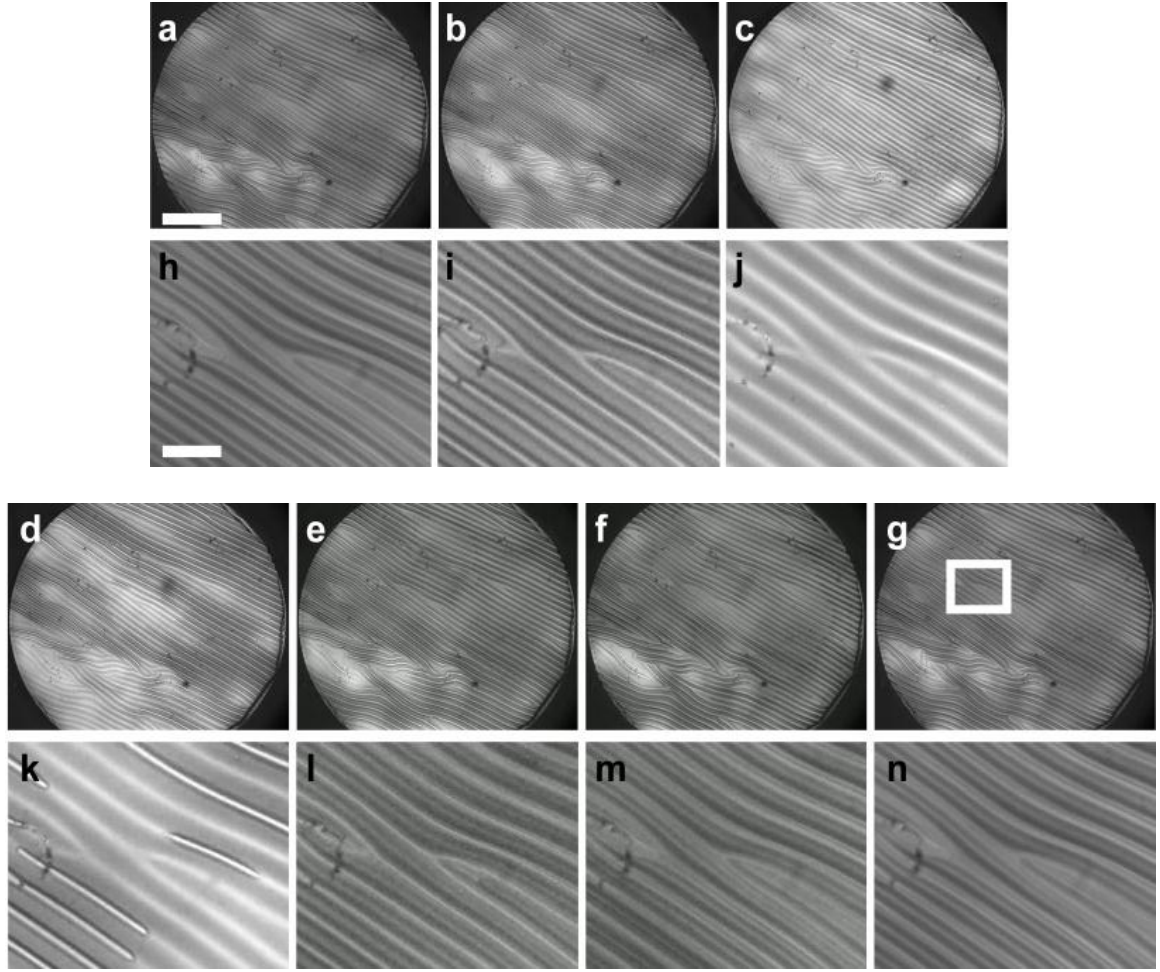
Figure 4.11: Image sequence of contact images for large wrinkles (b=5.0μm). Images obtained by adhesion testing on 10wt% PDMS film run at a displacement rate of 1μm/s. (a-g) show full probe while (h-n) contain magnified views of contact areas (white rectangle in (g) indicates location of insets). Lighter areas show interfacial contact. Time sequence: (a) surfaces are out of contact, (b) interface is forming along wrinkle peaks, (c) maximum compression, (d) wrinkle troughs begin to separate, (e) separation continues in wrinkle troughs with cracks propagating along troughs parallel to aligned wrinkles, (f) peak separation force, (g) surfaces are out of contact. Scale bar in (a) applies to images (a-g) and is 500μm while scale bar in (h) applies to images (h-n) and is 100μm.

captured during adhesion testing. A time sequence of the contact images for the high amplitude wrinkles (Figure 4.11) illustrates a unique separation mechanism. After the application of the full compressive load, the entire wrinkled surface of the probe is in contact with the soft film. The displacement is then reversed and while still in macroscopic compression (P<0), the troughs of the large wrinkles separate from the film.
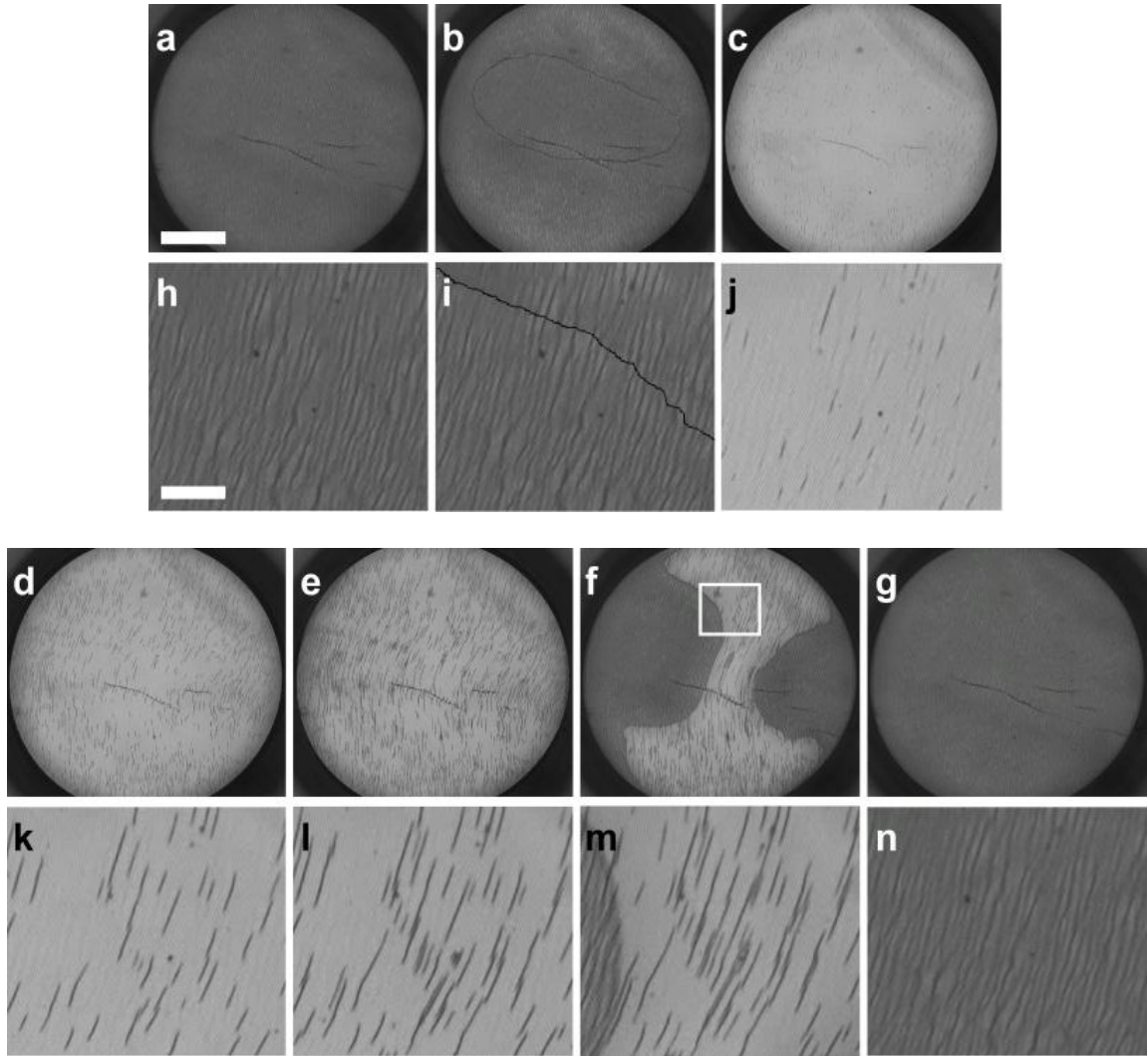
Figure 4.12: Image sequence of contact images for small wrinkles (b=0.5μm). Images obtained by adhesion testing on 10wt% PDMS film run at a displacement rate of 1μm/s. Top row of images show full probe while bottom row contains magnified view of contact areas (white rectangle in f indicates location of insets). Lighter areas (in (c-f) and (j-m)) show interfacial contact. Time sequence: (a) surfaces are out of contact, (b) interface is forming along wrinkle peaks (thin black line illustrates contact line front which is moving radially inward (center of probe is not in contact)), (c) maximum compression, (d) initiation of cracks along wrinkle troughs as surfaces begin to separate, (e) cracks continue to nucleate and propagate, (f) peak separation force, (g) surfaces are out of contact. Scale bar in (a) applies to images (a-g) and is 500μm while scale bar in (h) applies to images (h-n) and is 100μm.

Subsequently, as the surfaces are pulled further apart, the peaks of the wrinkles separate from the film. Only the peaks of the wrinkles exert a tensile or adhesive force on the interface, greatly reducing the adhesion of the rough surface relative to the smooth

separation stress. This two-step separation mechanism is the driving force dictating the reduced adhesive properties of large wrinkles on elastic materials.

The separation mechanism for the fully crosslinked films from rigid probes patterned with small wrinkle features (b=0.5μm) is significantly different relative to the larger wrinkles separating from the same smooth film. Figure 4.12 is a time sequence of the contact images for small wrinkles. The separation of these interfaces occurs in two steps as with the large amplitude, elastic interfaces. However, for small wrinkles, multiple small cracks occur at the interface along small portions of the wrinkle troughs across the entire probe face. These small crack openings require significantly more energy to form, leading to higher adhesion energy measurements. Once a critical portion of the interface separates along the troughs, full interfacial failure occurs in a manner similar to the separation of a smooth interface. Namely, the entire interface fails in a single, unstable crack propagating from the probe edges radially inward toward the center of the probe, independent of wrinkle troughs and peaks.

4.5.4 Wrinkle Scaling Relationships

The differences in adhesion observed for various size wrinkles contacting the most fully crosslinked film can be understood using previously reported wrinkle adhesion scaling relationships.[55] The separation force for an array of aligned wrinkles (P_c) has been calculated based on Johnson's contact mechanics relationship for an ellipsoid separating from a flat surface:[44]

$$P_c \cong \left(\frac{\pi \bar{E} G_c^3 c^7}{2^5 b^2}\right)^{\frac{1}{4}} \qquad (4.5)$$

where $\bar{E}$ is the plane strain modulus and G_c is the critical strain energy release rate. The fabrication technique used to form the rigid probes leads to a slight variation in probe radius. Thus, the separation strength (σ_s) rather than the separation force is used here:

$$\sigma_S \cong \frac{P_c}{\pi c^2} \cong \left(\frac{\bar{E} G_c^3}{2^5 \pi^3 b^2 c}\right)^{\frac{1}{4}} \qquad (4.6)$$

To determine whether adhesion increases or decreases relative to that of a smooth surface, we consider the separation strength of a flat punch from a flat surface, σ_{smooth}:[44,52]

$$\sigma_{smooth} \cong \left(\frac{8 \bar{E} G_c}{\pi c}\right)^{\frac{1}{2}} \qquad (4.7)$$

Finally, a normalization of the separation strength of a wrinkled surface by σ_{smooth} provides a relationship which allows comparison of the adhesive strength of wrinkles with that of unpatterned surfaces.

$$\frac{\sigma_S}{\sigma_{smooth}} \cong \left(\frac{G_c c}{2^6 \pi \bar{E} b^2}\right)^{\frac{1}{4}} \cong \left(\frac{G_c}{2^6 \pi}\right)^{\frac{1}{4}} \left(\frac{c}{\bar{E} b^2}\right)^{\frac{1}{4}} \qquad (4.8)$$

For the most crosslinked films tested here, the relationship of separation strength given by equation 4.5 describes our adhesion results fairly well. Figure 4.13b plots the separation strength as a function of the amplitude, illustrating the relationship between these two factors. This scaling relationship is appropriate for the highly crosslinked films (10%) but does not explain the adhesive response of wrinkled viscoelastic (2 and 4%) interfaces (Figure 4.13a).
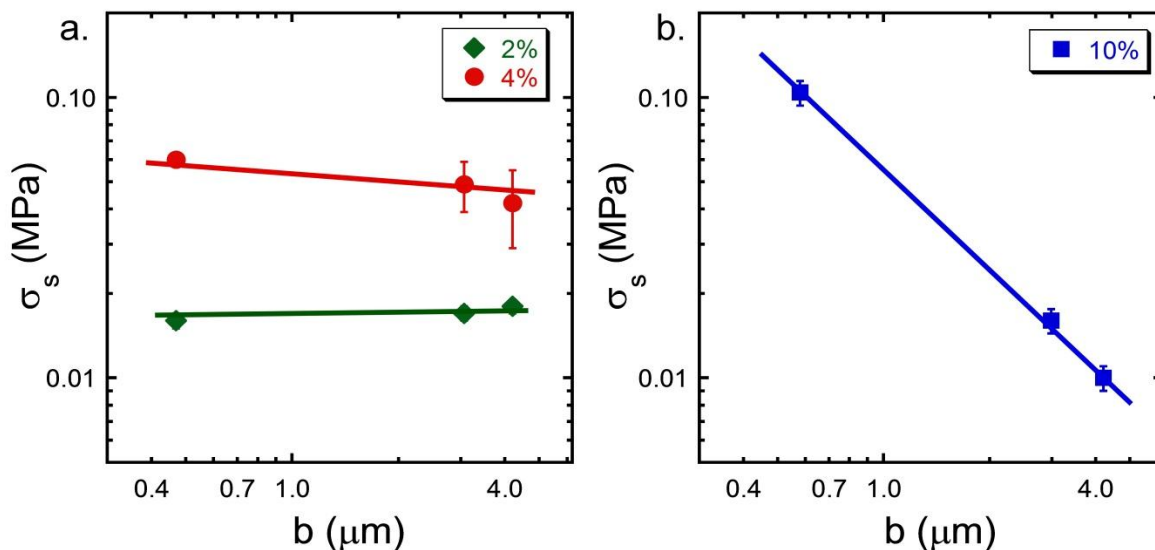
Figure 4.13: Separation stress as a function of the wrinkle amplitude. (a) 2 and 4% crosslinker and (b) 10% crosslinker concentrations. The lines are a guide to the eye and do not represent a numerical fit. The error bars represent 10% of the value.

4.5.5 Soft Wrinkles on Rigid Smooth Surfaces

Due to the unique sample fabrication techniques employed here, soft and rigid surfaces patterned with identical wrinkle topography can easily be formed. This facile molding technique (described in Figure 4.14) allows a direct comparison of surface roughness effects on adhesion with respect to the modulus of the underlying material. For purely elastic materials, the separation mechanisms are expected to be identical whether the surface topography is present on the rigid probe surface or the soft film surface. However, questions arise regarding the effects of modulus asymmetry of the interface on the adhesive properties of more viscoelastic materials.

To test the importance of soft wrinkles versus rigid wrinkles, wrinkled PDMS films of varying crosslinker concentrations are prepared by sequential molding steps as shown in Figure 4.14. This potential difference in the separation mechanisms of soft versus rigid wrinkles was the initial motivating question of the study described here.
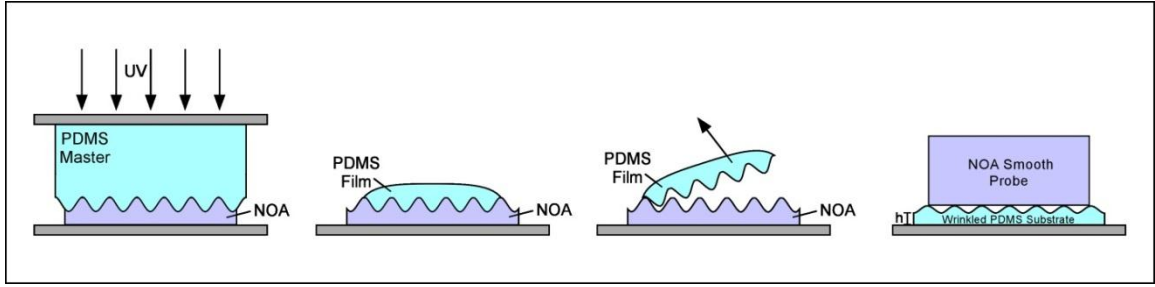
Figure 4.14: Schematic illustrating fabrication process for soft wrinkled films. A wrinkled PDMS master is utilized as a mold for NOA cast on a glass slide and exposed to UV radiation through the wrinkled master. Uncured, degassed PDMS of the desired crosslinker concentration is then cast onto the wrinkled NOA mold using a custom shim to ensure a uniform thickness is achieved. After thermal crosslinking of the film, the wrinkled PDMS is carefully removed from the NOA mold and applied (wrinkled surface up) on a clean glass slide and the normal adhesion tested with a smooth, cylindrical NOA probe (c~1.0mm).
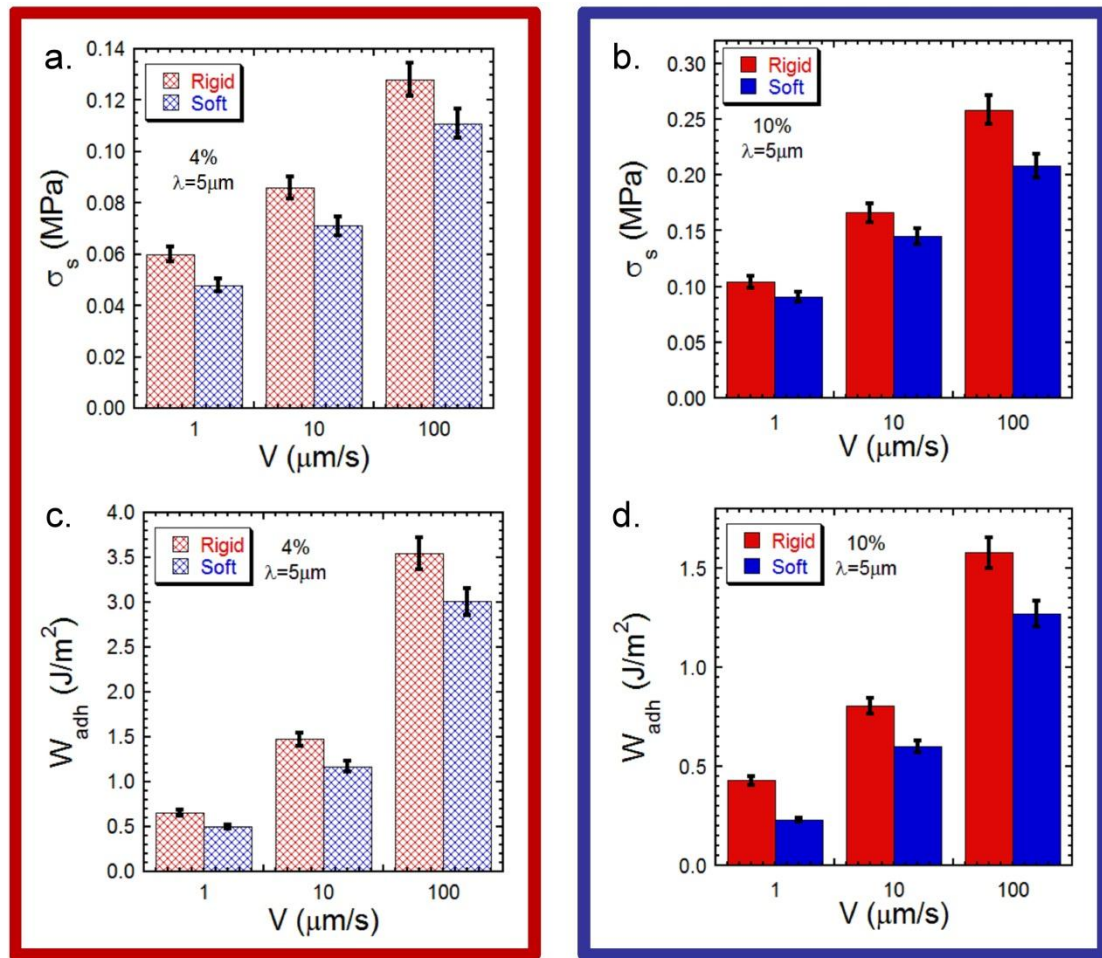
Figure 4.15: Soft versus hard wrinkle adhesion. Data shown for small wrinkles (*b*=0.5μm) on 4 and 10wt% PDMS.

Rigid wrinkles show a slightly larger adhesion force and work of adhesion than the equivalent wrinkle topography molded on a soft PDMS film contacting a flat rigid surface (Figure 4.15). This difference is small but statistically significant regardless of testing rate, crosslinker ratio, and wrinkle feature size for the soft and hard wrinkle interfaces. As a result of this small response, the analysis provided above has focused on the adhesion of rigid wrinkles contacting soft, smooth films.

4.6   Conclusions

The impact of rigid wrinkles on the adhesion of soft, smooth PDMS films with varying crosslinker ratios is presented here. For lightly crosslinked materials, adhesive forces dominate the behavior of the interface over length scales larger than the wrinkle amplitudes tested and wrinkles are subsequently shown to have little to no effect on adhesion. For highly crosslinked materials, adhesive forces affect distances shorter than the wrinkle amplitudes, thus wrinkles greatly impact the adhesion behavior of these surfaces. Large wrinkles decrease the separation strength and adhesion energy relative to smooth surfaces while small wrinkles increase these adhesion metrics nearly 200% over smooth surface adhesion values.

CHAPTER 5

WRINKLE MORPHOLOGIES WITH TWO DISTINCT

WAVELENGTHS

5.1 Introduction

Wrinkling is a phenomenon which results when a bilayer system of a stiff film supported on a soft substrate is compressed beyond a critical limit.[16] Examples of wrinkling can be seen ubiquitously in nature such as in the skin of a dried piece of fruit[91] or on our fingerprints.[3] For the scientific community, wrinkled surface patterns offer many unique attributes that cannot be achieved using conventional techniques (i.e. lithography, etching). Wrinkles form spontaneously,[8,25] cover large surface areas,[15] and they can be reversibly removed due to the elastic nature of the instability.[13,92]

The orientation or patterns of wrinkles can also be affected by the magnitude and direction of the applied strain.[12] For instance, if a uniaxial strain is applied to a laterally extensive sample, aligned wrinkles will form perpendicular to the principle compression direction.[17,19,22] With the application of biaxial compression, more complex patterns can be obtained.[16] Under equibiaxial strain conditions, patterns such as dimples, checkerboards, herringbones, and labyrinthine wrinkles have been observed experimentally[12] and predicted through numerical simulations.[27]

While dimples and herringbone patterns are considered equilibrium equibiaxial structures and are predicted theoretically, they are often difficult to achieve experimentally. In many experimental cases, the kinetics of strain application are too rapid for equilibrium structures to evolve, leading to patterns such as the commonly

observed labyrinth. Alternatively, different kinetic paths can lead to more complex patterns.[19,31] Ohzono and coworkers have studied substrates patterned with aligned wrinkles that were then compressed uniaxially at various angles relative to the primary compressive strain.[33,93] These studies reported the reversible rearrangement of the aligned wrinkles, and depending on the angle between the first and second compressive stress directions, the wrinkles were shown to form herringbones or align perpendicular to the second compressive stress direction.

This sequential application of strain provided beautiful access to a large array of unique patterns; however, for these experiments, only one lateral dimension or wavelength was observed. This characteristic wavelength is dependent upon the stiffness of the film and substrate components of the compressed bilayer system.[16] In this work, we report unique wrinkle morphologies comprised of two distinct wavelengths. Taking advantage of the curing kinetics of an elastomeric substrate, we alter the modulus of the substrate between strain applications, yielding a simple, robust fabrication technique for complex, yet systematic long range pattern formation. We observe the formation of several unique two wavelength morphologies, including ellipsoidal surface features which have not been presented through surface buckling or wrinkling to date to the authors' knowledge. Such surfaces may offer potential applications such as drag reduction,[94] self-cleaning,[95] and anti-reflective coatings.[96]

5.1.1 Wrinkling Mechanics

Here, we consider the surface buckling of a bilayer material system, typically, a thin, rigid film bound to a thick, soft substrate, under a lateral compressive strain. The mechanics of wrinkle formation are well understood and have been described

previously.[10,14] The elastic buckling instabilities of layered composite systems under lateral compression was investigated by Allen[14] and later investigated in the context of wrinkled surfaces by Bowden and coworkers in addition to many others.[7,11,15,16] For buckling to occur, a critical buckling strain, ϵ_c, must be exceeded. The critical strain is independent of material geometry and determined only by the modulus mismatch (ratio between film and substrate modulus):

$$\epsilon_c = \frac{1}{4}\left(\frac{3\bar{E}_s}{\bar{E}_f}\right)^{\frac{2}{3}}$$

(5.1)

For the polymer and metal systems most commonly reported in wrinkling experiments, this critical strain is on the order of $0.001 \leq \epsilon_c \leq 0.01$ and can be easily reached through swelling,[25] thermal expansion or contraction,[8,11,16] and mechanical compression techniques.[17] Beyond the critical strain, a periodic out-of-plane surface deformation, or wrinkle, is observed. Two length scales, wavelength and amplitude, can be used to describe these deformations. Importantly, these length scales are defined independently by materials properties/testing geometry and strain respectively.

The thin film has a low bending energy, U_b, relative to its stretching energy, U_s, predisposing it to buckle out-of-plane rather than stretch or compress in-plane when strained laterally. The thick substrate, on the other hand, has $U_s < U_b$ so that simple in-plane deformation is favored over buckling when subjected to a lateral compressive strain. The resulting deformation is a compromise between these two competing deformation modes: periodic surface buckling or wrinkling. The distance between two adjacent buckles is defined as the wavelength, λ, which is dependent on the thickness of the film, t, and plane strain modulus of the film, $\bar{E}_f$, and substrate, $\bar{E}_s$, such that:[14,16]

$$\lambda = 2\pi t \left(\frac{\bar{E}_f}{3\bar{E}_s}\right)^{\frac{1}{3}}$$

(5.2)

where the plane strain modulus of each material is defined as $\bar{E}_i = E_i/(1 - \nu_i^2)$. Assuming the top film is inextensible, the amplitude, b, of wrinkles is dependent on the amount of compressive strain applied to the system:[14,16]

$$b = t\sqrt{\frac{\epsilon}{\epsilon_c} - 1}$$

(5.3)

5.2 Experimental Approach

5.2.1 Overview of Methods

We form biaxially wrinkled surfaces through a two-step application of sequentially-applied uniaxial strains. By controlling the extent of crosslinking of the elastic substrate at each strain application, wrinkle morphologies with two distinct, tunable orthogonal wavelengths on a single surface are observed. Briefly, our biaxial wrinkle surfaces are achieved by 1) forming aligned wrinkles on a partially crosslinked soft substrate, 2) completing the crosslinking reaction of the substrate, and 3) applying a uniaxial strain orthogonal to the initial uniaxial strain direction. The modulus and thickness of the thin film remain constant throughout our process while the modulus of the substrate is varied by more than an order of magnitude between the first and second strain applications.

5.2.2 Materials

For experiments reported here, the thin film is high molecular weight, atactic polystyrene (PS, M_n=1,100kg/mol, PDI=1.15, Polymer Source, Inc.). The film is formed by spincoating from toluene (Fisher Scientific) on ultraviolet/ozone (UVO Jelight 342) treated silicon wafers (University Wafer). Variations in polymer concentration allow the

film thickness to be controlled, and films ranging from t=70 to t=200nm (measured with white light interferometry (Filmetrics)) are produced.

For the elastic substrate, polydimethyl siloxane (PDMS) (Dow Corning Sylgard 184) is prepared, controlling the oligomer to curing agent ratio by weight. The PDMS mixtures are degassed in a reduced pressure environment for 30 minutes, poured into glass molds measuring 2cm x 2cm x 4mm and placed in an oven while the curing time is varied, allowing the crosslinking reaction to proceed to varying degrees of completion as described previously.[55] Substrates are partially-cured at either T=25°C or T=70°C for 20-120 minutes to vary the primary substrate modulus $(\bar{E}_{s,1})$. Two oligomer to curing agent ratios (10:1 and 30:1 by weight) are used to control the secondary substrate modulus $(\bar{E}_{s,2})$. Upon completion of the first curing process, substrates are removed from their glass molds and transferred onto glass slides coated with poly(acrylic acid) (PAA, Mn=1.8kg/mol, Fisher Scientific). The PAA will be used as a lubricating layer to reduce friction between the glass surface and the elastic substrate when the sample is placed in a uniaxial compression state. We take advantage of the hydrophilic nature of the PAA, swelling it with a few drops of water prior to the mechanical strain application.

5.2.3 Characterization of Substrate Modulus

The moduli of the PDMS substrates (partially and fully cured) are characterized using contact mechanics measurement techniques. A custom-built contact adhesion testing device that has been thoroughly described in prior work is utilized.[23,55,83] A rigid silica spherical indenter is pressed into each substrate at a fixed displacement rate while the normal force and contact area between the PDMS elastomer and the indenter are monitored. The modulus is determined by fitting a curve to the experimental force versus

displacement data. Utilizing the theory of Johnson, Kendall, and Roberts (JKR),[56] the experimental data is fitted to determine $\bar{E}_{s,i}$.[52]

5.2.4 Application of Mechanical Compressive Strain

After formation of the primary set of wrinkles, secondary wrinkles are achieved through the application of a uniaxial compressive strain applied to each sample (orthogonal to the primary wrinkle direction). A custom-built mechanical strain stage (Newport) is mounted under the objective of an optical microscope (Zeiss Axiotech Vario) or optical profilometer (Zygo NewView 7300), allowing the morphology of the wrinkles to be monitored while strain is applied. Compressive strain is applied manually in small increments ($\epsilon \sim 0.0025$). After each strain application, a period of 5 minutes elapsed before image capture. To ensure full-slip boundary conditions along the bottoms and compressed sides of each sample and to maintain uniformity of applied strains, the PAA between the substrate and the supporting glass slide is swollen with water and the side walls of the strain stage are coated with a silicone release layer.

5.3 Results

5.3.1 Primary Wrinkle Morphology

The primary surface wrinkles are formed on a partially-cured substrate utilizing a previously reported technique.[26,55] Taking advantage of the instability formed due to local strain at the three point contact line between a glassy film floating on water and an elastic substrate, aligned wrinkles are produced one at a time, resulting in surfaces of parallel wrinkles with very few defects. Figure 5.1a illustrates the wrinkling process schematically.
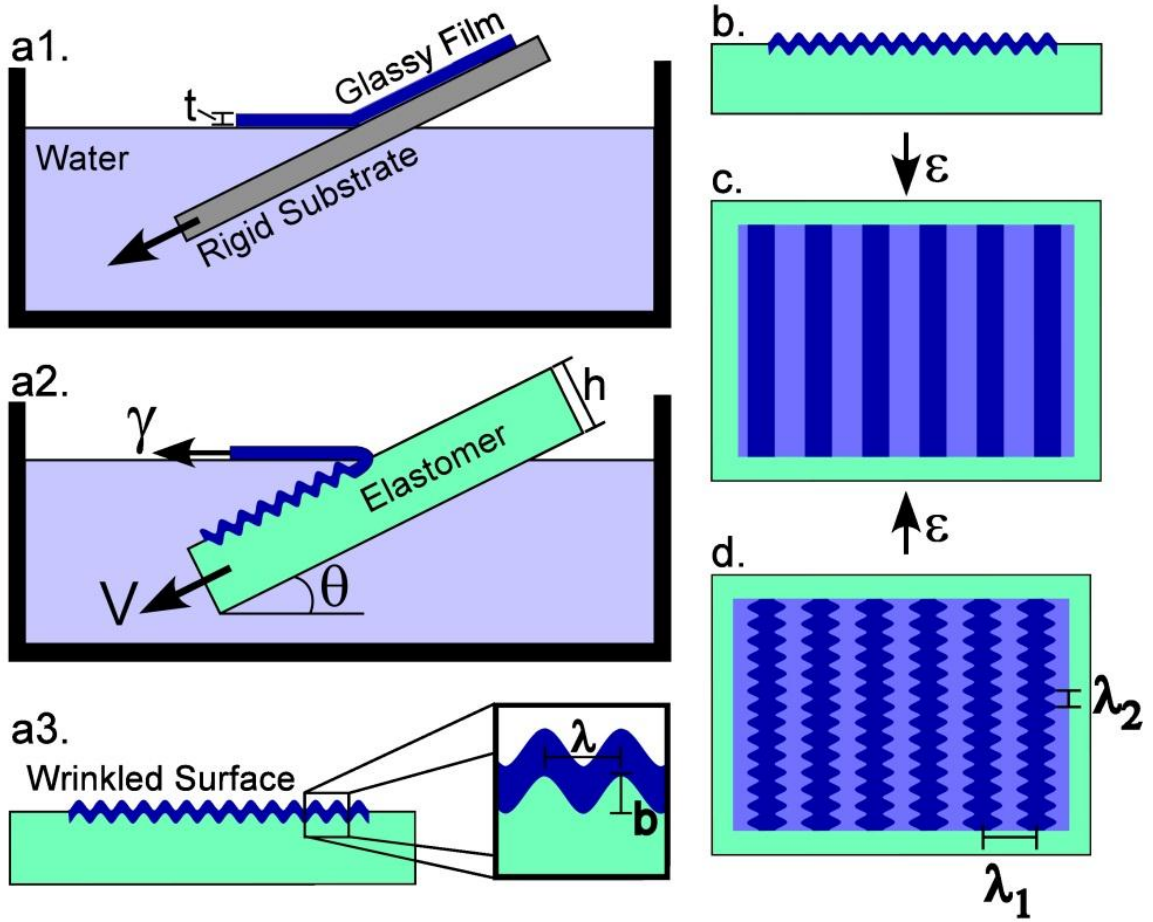
Figure 5.1: Schematic of sequentially-strained biaxial wrinkle fabrication technique. (a1-a3) Contact line wrinkling process to develop uniaxially aligned wrinkles adapted from Miquelard-Garnier et al.[26] Glassy thin film is floated off of a rigid substrate onto the surface of a water bath. (a2) Elastomeric substrate is partially submerged in the water bath at an angle and one edge of the film is attached to the substrate at the solid-liquid-vapor contact line. The elastomer is then moved into the water bath at a controlled velocity (V) and wrinkles form one at a time at the contact line resulting in a surface of aligned wrinkles (a3). (b) schematic of aligned wrinkle cross-section prior to secondary strain application. (c) Topview illustrating direction of secondary compressive strain applied orthogonal to casting direction utilized for initial wrinkle formation. Dark and light stripes represent peaks and troughs of initial wrinkles. (d) Upon secondary compression, biaxial wrinkled structures with two distinct wavelengths (λ_1 and λ_2) are formed.

In brief, to form the initial aligned wrinkles the PS film ($A=1cm^2$) is floated onto the surface of a water bath, and the partially-cured PDMS substrate is partly submerged in the water bath with an edge of the film attached to the substrate. The substrate is driven

deeper into the water bath at a fixed velocity (V=100μm/s) using a linear actuator (Burleigh Inchworm Nanopositioner). As the substrate is moved into the water bath, adhesion between the film and substrate combined with surface tension on the film deforms the surface of the substrate locally at the contact line, causing wrinkles to form one at a time. Adhesion forces attach the two layers permanently, leading to stable wrinkles that do not relax over time. This method of wrinkling leads to parallel wrinkles with very few defects. For more details on this wrinkling process, the reader is referred to Miquelard-Garnier and coworkers work on contact line wrinkle formation.[26]
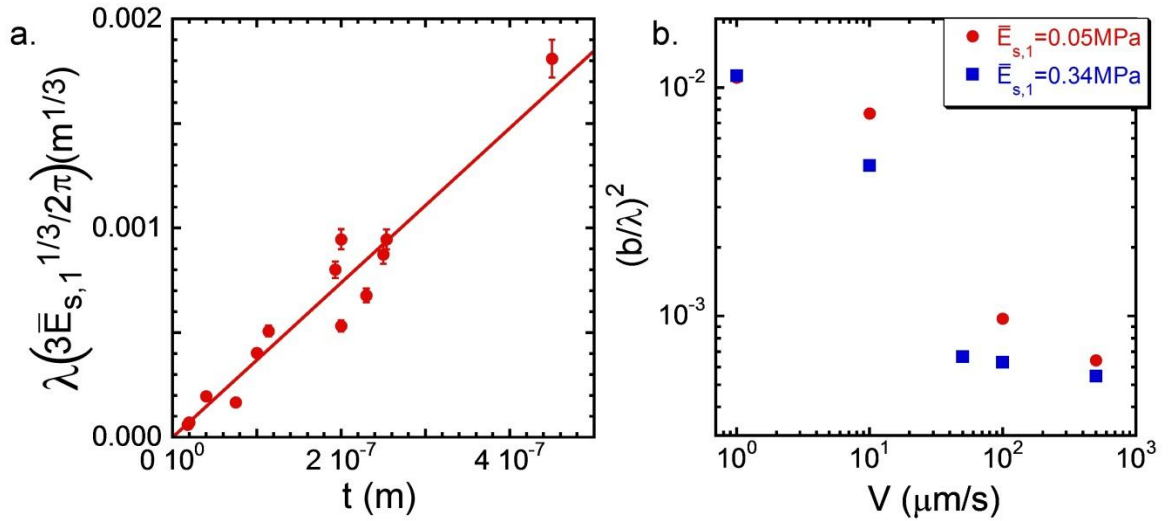
Figure 5.2: Primary wrinkle geometry as a function of sample geometry and processing conditions. (a) Normalized wavelength (utilizing characteristic wavelength equation (Equation 5.2) as a function of film thickness. Data represent several partially cured substrate moduli. Only wrinkles produced at a substrate velocity of $V=10$μm/s are included. (b) Primary wrinkle calculated strain ($\epsilon \sim (b/\lambda)^2$) as a function of substrate velocity during processing for two primary substrate moduli.

After wrinkles are formed on the partially-cured substrate, the samples are returned to the oven (T=25°C or T=70°C) for an additional 24 hours. Both of these curing temperatures are below the glass transition temperature, T_g, of PS ($T_g \sim 105°C$)[28] so the film is assumed to remain rigid during the substrate curing process. The wrinkled film

94

acts as an in situ mold, holding the surface of the rubber in the strained, wrinkled shape until crosslinking is completed. Figure 5.3c presents the wavelengths and amplitudes of two wrinkled samples before and after the second curing step.
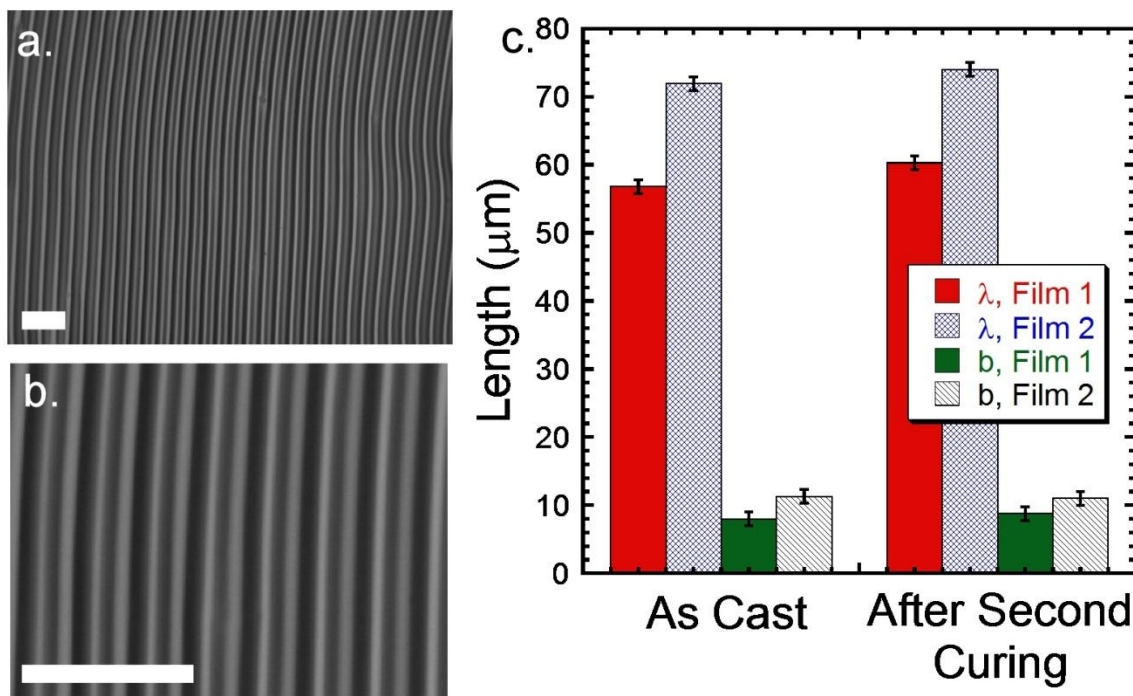
Figure 5.3: Effects of secondary curing. (a-b) Optical micrographs of wrinkles after secondary curing demonstrating well aligned wrinkle morphology. Scale bar = 50μm. (c) Wavelength and amplitudes of two wrinkle samples before and after the secondary curing. Both PS films were cast on the same PDMS substrate (t_1=110nm, t_2=230nm).

5.3.2   Secondary Wrinkle Morphology

After the primary set of aligned wrinkles are formed and the second curing step is completed, a uniaxial, mechanical compressive strain is applied to the wrinkled substrates orthogonal to the wrinkle direction, as shown in Figure 5.1c. The primary and secondary wavelengths (λ_1 and λ_2) of the resulting wrinkles are measured from optical micrographs. ImageJ (NIH) is used for image analysis. In brief, a Fast Fourier Transform (FFT) is applied to each image and the distance between adjacent intensity peaks is used to obtain an average value of λ_1 and λ_2 for each sample. The primary wavelength is quantified in

this manner before and after the application of the secondary strain and does not vary as a result of this wrinkling step as shown in Figure 5.3c.

The amplitudes of the primary and secondary wrinkles (b_1 and b_2) are measured using optical profilometry. Analysis of scans show that the wrinkles have sinusoidal profiles, further supporting the statement that primary and secondary wrinkles, rather than folds,[97,98] are observed (Figure 5.4d).
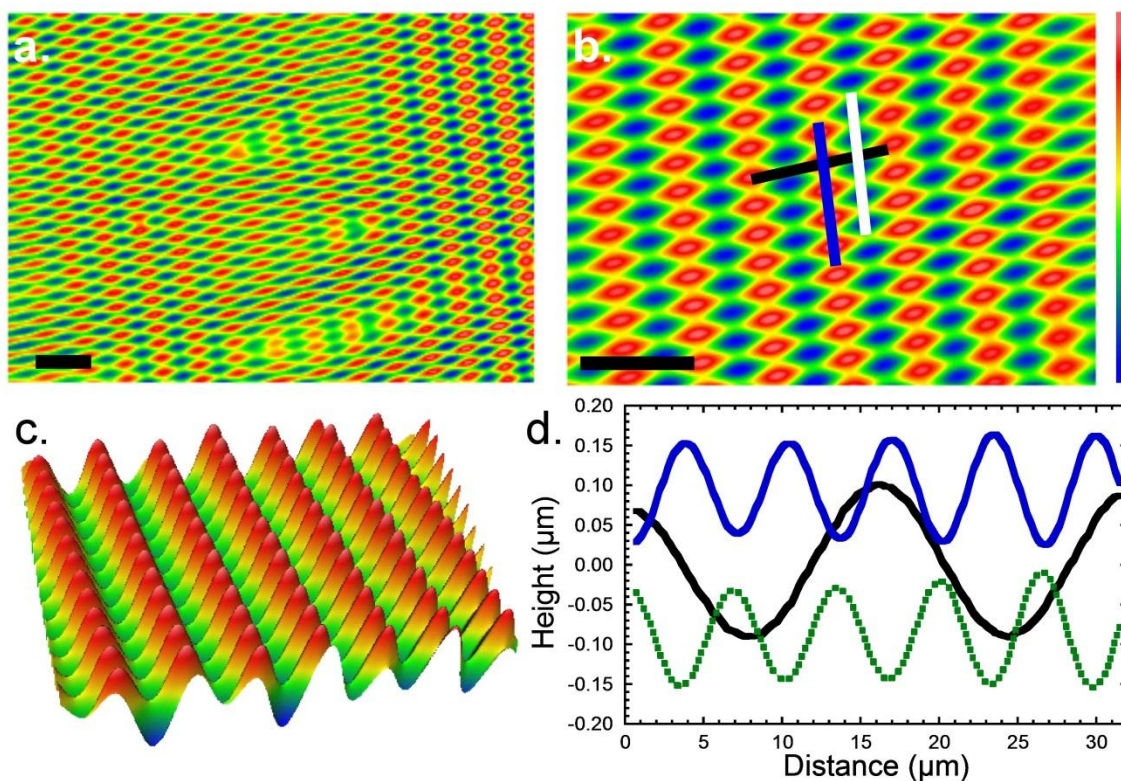
Figure 5.4: Unique biaxial wrinkle morphologies. (a-b) Optical profilometry surface scans illustrating topography and long range order of sequentially-strained biaxial wrinkles. Scale bar= 25μm. (c) 3D topography map corresponding to (b) (lateral dimensions 118x83μm). Note that the aspect ratio of the features is greatly exaggerated in the 3D plot. Z-axis scale (right of (b)) is -0.18 to 0.18μm for (a-c). (d) Surface profiles of primary wrinkles ((b and d) black line) and secondary wrinkles measured along both the peaks ((b and d) blue line) and the troughs ((b and d) white/green dotted line) of the primary wrinkles.

Utilizing this two-step sequential strain technique to develop biaxially wrinkled surfaces, unique arrays of elliptical lenses are formed on the surface of the PS/PDMS

bilayers as seen in Figure 5.4. Large (λ_1=10.0 − 21.4µm) wrinkles are formed through wrinkle dipcasting on low modulus, partially-cured substrates. After formation of this primary set of wrinkles, the substrates are completely crosslinked, causing up to a 15 fold increase in the substrate modulus. Mechanical strain is then applied orthogonal to the substrate direction to induce the formation of a second set of smaller (λ_2=5.7 − 19.2µm) wrinkles superimposed on top of the primary wrinkles. Optical profilometry allows the wavelength and amplitudes of both the primary (λ_1, b_1) and secondary (λ_2, b_2) wrinkles to be monitored while mechanical strain is applied to the system. Profile traces drawn parallel to the primary and secondary strain directions (see Figure 5.4b and 5.4d) show the sinusoidal profile of both the first and second sets of wrinkles on a sequentially-strained surface. From these wrinkle profiles, it is clearly seen that λ_1 and λ_2 are quantitatively different. The second set of wrinkles (those resulting from the mechanical strain after fully crosslinking the substrate) has a smaller wavelength and amplitude which can be seen along the peaks and the troughs of the primary wrinkles.

5.4 Discussion

As seen in Figure 5.5a, the mismatch between the moduli of the partially-cured and fully-cured PDMS substrates can be used to control the ratio of λ_1 and λ_2. This ratio can be easily understood using equation 1.5 to obtain:

$$\frac{\lambda_2}{\lambda_1} = \left(\frac{\bar{E}_{s,1}}{\bar{E}_{s,2}}\right)^{\frac{1}{3}} \tag{5.4}$$

Figure 5.5a plots this relationship for data obtained at low mechanical strains for PS/PDMS samples representing several film thicknesses (λ_1 and λ_2), oligomer : curing agent ratios ($\bar{E}_{s,2}$), and degree of partial crosslinking prior to primary wrinkle formation

$\left(\bar{E}_{s,1}/\bar{E}_{s,2}\right)$. The black solid line is $y = x$ and describes the data well, demonstrating that the modulus mismatch achieved through the two step substrate crosslinking process allows control of the mismatch between the primary and secondary wavelengths.
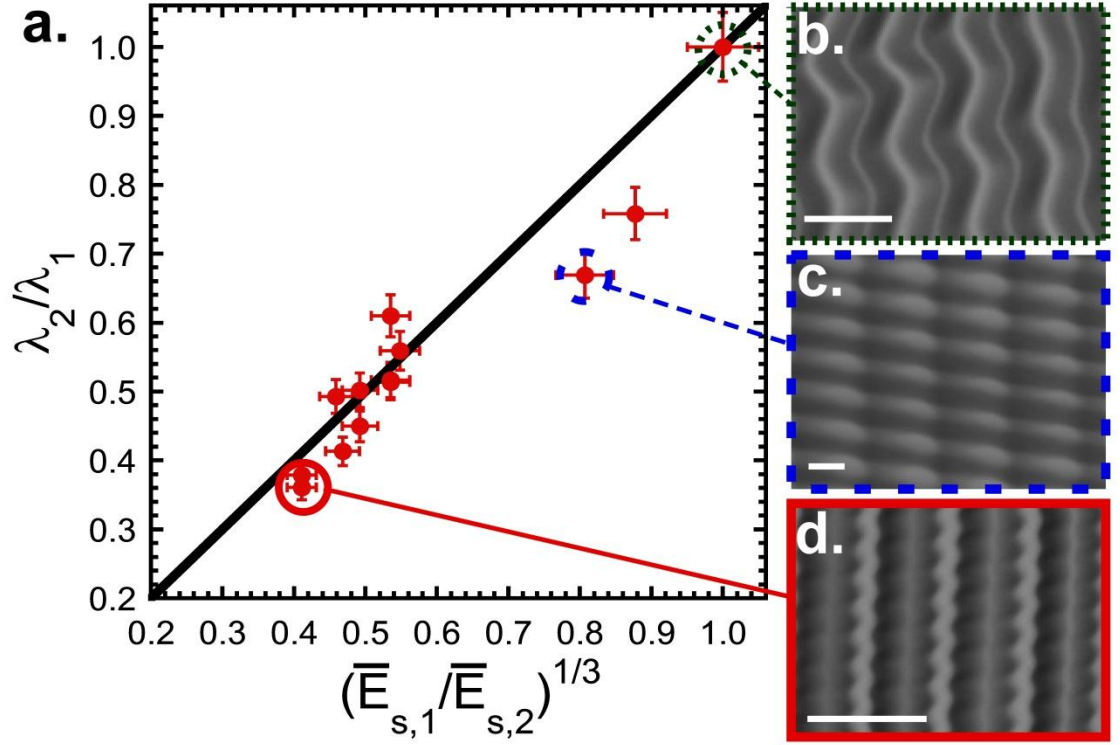
Figure 5.5: Wavelength as a function of modulus mismatch. (a) Relationship between substrate modulus and wavelength mismatch. The solid line represents y=x and the error bars represent 10% error. The circled data points on the plot correspond to images (b-d) with the pairings illustrated with line dashes and color. (b-d) Optical micrographs of biaxially wrinkled surfaces with primary wrinkles aligned vertically and secondary compressive strain applied orthogonal to initial strain (vertically). Scale bars=25μm.

When $\bar{E}_{s,1}/\bar{E}_{s,2} < 1$, a host of unique morphologies are observed upon the application of a secondary strain. As seen in the optical profilometry results of Figure 5.4 as well as Figure 5.5b-c, secondary wrinkles oriented roughly perpendicular to the wrinkling direction of the primary wrinkles develop when strained. This secondary wrinkling process is fairly tolerant to off-angle strain applications; it was observed at angles of up to ±10° away from perpendicular. At large modulus mismatch values, the

secondary wrinkles appeared as small zigzags along the ridges of the large, primary aligned wrinkles.

For intermediate modulus mismatches, "corn-on-the-cob" morphologies were observed. A secondary wrinkle formed on the peak of a primary wrinkle and another secondary wrinkle formed next to it on the adjacent primary peak. Thus the secondary wrinkle morphology appears to be strongly affected by the orientation of the primary wrinkles. Figure 5.5c illustrates the well-ordered array of tightly packed elliptical bumps or lenses formed upon secondary compression of the sample. When the secondary strain is applied exactly orthogonal to the primary wrinkle direction, these elliptical bumps are arranged or packed so that they form the "egg crate" morphology, shown in Figure 5.4. Qualitative observations of the optical micrographs (Figure 5.5b-d) corresponding to points on the graph highlight the morphological changes associated with various values of $\bar{E}_{s,1}/\bar{E}_{s,2}$.

For $\bar{E}_{s,1}/\bar{E}_{s,2} = 1$, the primary and secondary wrinkles are formed with strains applied to substrates with equal moduli. Here, the secondary strain does not lead to the formation of secondary wrinkles as for a modulus mismatch less than unity. Rather, the application of a mechanical compressive strain orthogonal to the primary wrinkles leads to rearrangement of the wrinkles so that they form herringbone morphologies as predicted by Chen et al.[18] and observed previously by Ohzono et al.[33]

The above wrinkling morphologies are all observed at low secondary strains ($0.05 \leq \epsilon \leq 0.06$). With the application of additional strain after the onset of secondary buckling, strain localizations are observed ($\epsilon \geq 0.06$). Figure 5.5b is an optical micrograph which was captured at the onset of buckling. The secondary ridge

morphology forms simultaneously over the entire surface of the PS film. Then, localizations propagate in a hopping fashion as more strain is applied. While these localizations lead to large amplitude buckled features, they are nearly reversible, as observed in Figure 5.6f. It is interesting to note that these localizations recover the herringbone morphology predicted for an equibiaxially strained, wrinkled surface and observed in other sequential strain wrinkling studies.
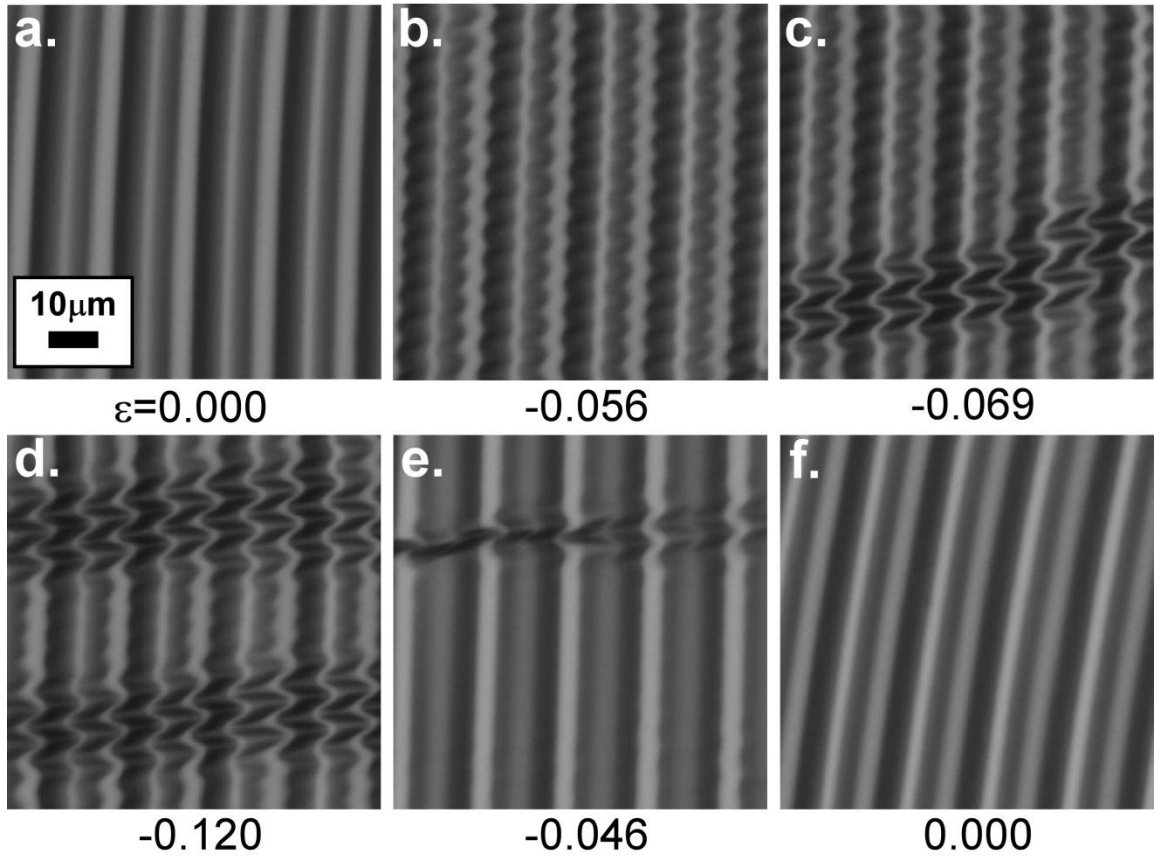
Figure 5.6: Optical micrographs capturing strain sequence as uniaxial compressive strain is applied and released orthogonal to primary wrinkle direction. Scale bar applies to all images.

The wrinkling process described here is fairly robust, allowing some off-angle mechanical compression but still resulting in the smaller orthogonal wrinkles superimposed on the large primary wrinkles. Application of the mechanical strain in the

same direction as the primary strain initially leads to a slight increase in the amplitude of the wrinkles but for the majority of the samples tested here, the final substrate modulus $(\bar{E}_{s,2})$ is too high to allow further wrinkling and delamination occurs at higher strains. Hierarchical wrinkles comprised of two superimposed parallel wrinkle arrays like those reported by Efimenko and coworkers are not observed for this technique.[99]

5.5   Conclusions

Wrinkles with two distinct wavelengths formed sequentially on the same surface are investigated here. A series of aligned wrinkles formed through local strain application at the three-phase contact line during wrinkle dipcasting are patterned onto a partially crosslinked elastomer. After the formation of these primary wrinkles, the elastomer is fully crosslinked and a mechanical compressive strain is applied to the sample orthogonal to the primary wrinkles. This mechanical strain results in smaller secondary wrinkles, which are superimposed on the larger primary aligned wrinkles in morphologies that suggest the primary pattern directs the formation of the smaller wrinkles.

We show that the ratio between the moduli of the substrate at the times of primary and secondary wrinkle formation respectively dictates the ratio of the two observed wavelengths. This relationship is in agreement with the characteristic wavelength equation frequently employed in wrinkling mechanics experiments. Unique biaxial wrinkle morphologies are reported here. Depending on the mismatch between the primary and secondary substrate moduli, a library of new morphologies ranging from zigzag ridges to ellipsoidal bumps or corn-on-the-cob structures to the classic herringbone are demonstrated. The sequential strain wrinkling process introduced in this

work has the potential to be used on an industrial scale for the facile formation of surface

topography with two discrete, tunable lateral dimensions over large surface areas.

CHAPTER 6

CONCLUSIONS

Wrinkled surfaces form spontaneously as a result of an imposed compressive stress on a bilayer system. The method in which the compressive stress is delivered and the materials used to comprise the bilayer composite can be varied significantly. Further, due to their spontaneous formation, wrinkles can cover large areas and by tuning materials geometry and the amount of strain applied, wrinkle wavelength and amplitude can be controlled easily. In the work presented here, we focus on utilizing wrinkles to control adhesion. By developing a more comprehensive understanding of the key parameters impacting wrinkled surface adhesion, the ability to engineer wrinkled surfaces to obtain desired adhesive properties can be achieved.

A series of experiments has been carefully designed to allow wrinkle adhesion and identification of key variables and parameters to be explored. We first examine the contact of a single wrinkle or cylinder with a finite flat probe. An elliptical separation mechanism rather than a long cylinder relationship is employed to model the separation force of these finite contact areas on cylinders. As a result, it is discovered that the separation force of a short cylinder scales as $P_c^{ell} \sim c^{\frac{3}{4}} R^{\frac{1}{2}}$ rather than $P_c^{cyl} \sim c R^{\frac{1}{3}}$ as predicted for a long cylinder. While these two relationships appear similar, the differences in the exponential scaling with probe radius and cylinder radius propagate significantly when applied to an array of wrinkles. The identification and understanding of the appropriate separation mechanism for a short cylinder represents a significant advance in experimental contact mechanics.

Building upon knowledge gained through these single cylinder adhesion experiments, the separation force of a model system of aligned wrinkles is explored and the significant parameters governing the adhesion are identified. Several keys strategies are employed in the preparation of the wrinkle surfaces to ensure the adhesion results are as close to theoretical values as possible. A fabrication technique that forms well aligned wrinkles with very few defects, carefully controlled surface chemistry, and a two-step substrate curing process are employed to ensure a "model" wrinkled surface is achieved. By systematically varying the wrinkle wavelength and amplitude, probe radius, and substrate modulus, a comprehensive scaling relationship is tested and verified against our experimental results. These experiments demonstrate and explain the decrease in separation force as a function of these parameters.

After developing a relationship for the adhesion of well-controlled, "model" wrinkles, additional complexity in the form of viscoelasticity and geometric confinement was introduced to the wrinkle adhesion study. Elastomeric substrate crosslinker concentration and wrinkle amplitude were varied systematically here. The materials defined length scale $G_c/\bar{E}$ dictated the parameter space in which wrinkled surface features impact adhesion. Ultimately, the wrinkles used in this study were too small to alter the adhesion of the two most lightly crosslinked films while for the highly crosslinked films, significant changes in adhesive properties were observed. Large amplitude wrinkles dramatically reduced the adhesion energy and separation force relative to a smooth interface while small wrinkles increased adhesion relative to smooth surfaces two-fold.

Finally, having formed a fairly complete knowledge of the wrinkle geometry parameters that govern adhesion, the development of more complex wrinkle patterns allowing the adhesive response of a surface to be engineered seems a logical next step. Capitalizing on the knowledge gained by fabrication of wrinkled surfaces in a host of different materials and utilizing multiple processing techniques, a process was devised to develop wrinkled surfaces patterned with two distinct lateral dimensions. Aligned wrinkles were initially formed on partially cured substrates, the crosslinking reaction was allowed to run to completion, and then a mechanical compressive strain was applied orthogonal to the primary wrinkle direction. The resulting wrinkled surfaces were characterized by two distinct wavelengths measured orthogonal to one another. These novel wrinkle morphology have not been observed previously and the ratio between the primary and secondary wavelengths is explained as a ratio of the characteristic wavelength equation or more simply $\lambda_2/\lambda_1 = \left(\bar{E}_{s,1}/\bar{E}_{s,2}\right)^{\frac{1}{3}}$.

Overall, this work yields a more complete understanding of many parameters that can impact wrinkle adhesion. A working knowledge of the influence of materials properties, wrinkle geometry, sample and testing geometry and experimental testing conditions has been obtained and presented here. Utilizing the methods and relationships presented in this work, wrinkled surfaces with precisely controlled adhesive properties can be engineered.

As with all scientific research, open questions still remain. The impact of biaxially compressed wrinkles on normal adhesion still has yet to be addressed in a careful, model study as the aligned wrinkle surfaces were treated here. Not only should the adhesion of simple biaxial wrinkle morphologies such as the labyrinth or herringbone be investigated

but also the adhesion of the more complex, dual wavelength wrinkles developed here. In these biaxial wrinkle adhesion studies, the influence of the persistence length or average length over which a wrinkle is ordered or aligned[20] is expected to play a significant role in the scaling of the separation force. Additionally, adhesion testing geometries not explored in this work such as shear adhesion or peel testing will yield valuable insight into the adhesion of wrinkled surfaces.

The results and conclusions presented in this thesis are technologically significant. We can now control surface adhesion and engineer specific separation stresses and adhesion energies onto a surface by tuning one of the many parameters now at our disposal.

APPENDIX

POLYDIMETHYL SILOXANE PROPERTIES AND CHEMISTRY

Polydimethyl siloxane or PDMS is a polymer which is frequently employed in microfluidics device development as well as fundamental and practical contact mechanics experiments.[100] The most commonly utilized PDMS is Sylgard 184, available from Dow Corning as a two part kit. This kit contains a base (a viscous liquid comprised of polydisperse, vinyl-terminated oligomers and long chain polymers of PDMS, silica filler, platinum based catalyst) and a curing agent (a low viscosity fluid containing PDMS oligomers and Si-H functionalized crosslinking molecules).[86,101] The exact formulation of Sylgard is unknown since it is a commercial product. However, the most popularly accepted reaction mechanism is presented in Figure A.1.
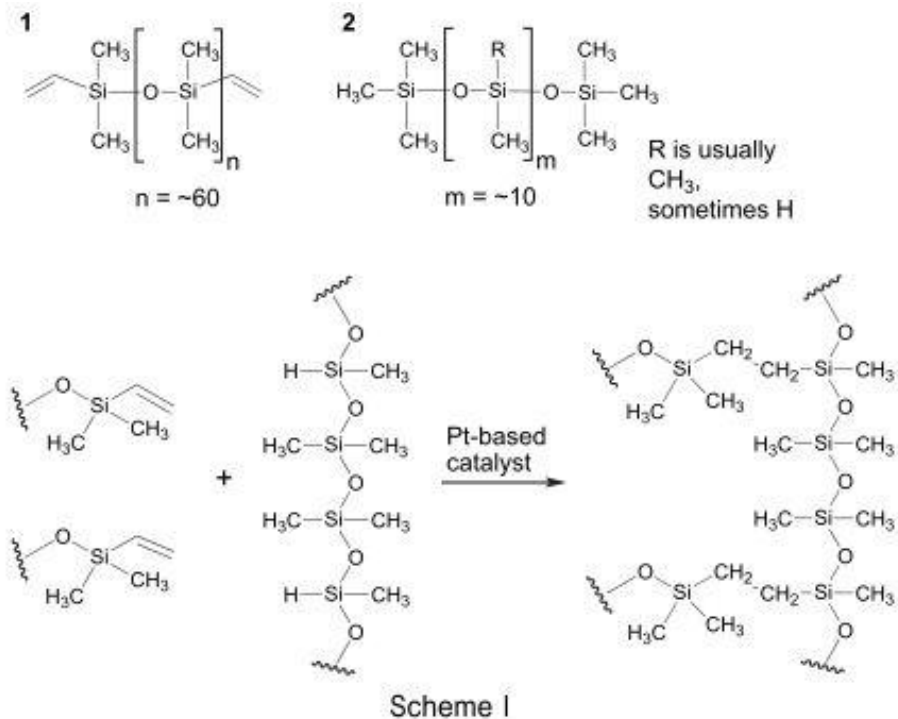
Figure A.1: Proposed reaction scheme for Sylgard 184.[102] Used with permission J. Chem. Edu. 1999.

The platinum catalyst facilitates crosslinking between the vinyl groups of the multifunctional crosslinker or ends of the PDMS oligomers and polymers and the Si-H groups on the main -Si-O- chains. While the details of the PDMS crosslinking reaction are still debated, a likely mechanism for the formation of crosslinks is the Chalk-Harrod hydrosilylation mechanism presented below.[103–105]
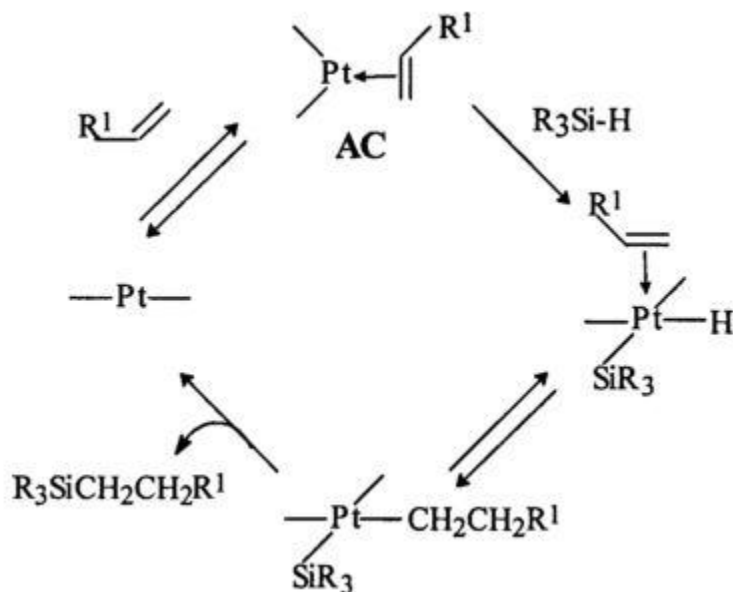
Figure A.2: Chalk-Harrod hydrosilylation mechanism.[104,105] Used with permission: J. Poly. Sci. A. 2007.

PDMS is a material commonly used in engineering and fundamental material science explorations due to several beneficial properties. Its transparency enables microscopic experiments and facilitates microfabrication techniques. As a stable dielectric with high reversion resistance, PDMS is an ideal choice in microelectronic and microfluidic devices. Additionally, the low toxicity and reparability (ability to be healed with the application of a small amount of uncured PDMS) add to its appeal. In the field of materials science, the material properties of PDMS such as high tensile elongation, nearly

perfect elasticity ($v \approx 0.5$), and high thermal stability (working temperature between -55°C and 150°C) are desirable as well.[101]

The modulus and viscoelastic properties of PDMS can be tuned by varying the amount of crosslinker or curing agent added to the base prior to thermal curing. According to the material data sheet provided by Dow Corning,[101] the stoichiometric formulation that results in a fully crosslinked elastomer is 10 parts base to 1 part (10:1) curing agent by weight. Reducing the amount of curing agent in the mixture, as shown in Chapter 4 as well as by several others,[82,86,106] results in a higher molecular weight between crosslinks and the presence of unreacted chains of oligomeric and polymeric PDMS. The more lightly crosslinked material has lower elastic and shear storage moduli than the 10:1 formulation and a more viscoelastic response to deformation due to the free chains and relatively long distance between crosslinks.

Figure A.3: PDMS modulus dependence on curing agent concentration and curing time.[106] (a) E of PDMS cured at 85°C for 100 minutes measured by tensile testing. X-axis units reflect 9:1 − 16:1 base to curing agent ratios by weight. (b) E of PDMS as a function of curing time for two different base to curing agent ratios. Samples were held at 100°C for the number of days indicated.
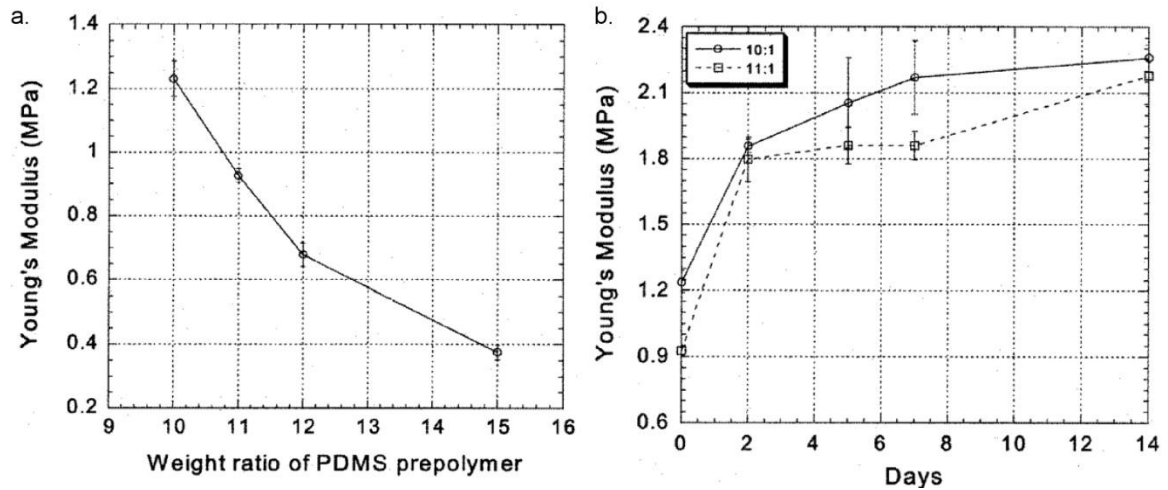
Alternatively, adding more curing agent to the base in the Sylgard kit results in a stiffer network, as seen in Figure A.3. The presence of more crosslinker molecules in the PDMS formulation during curing leads to a lower molecular weight between crosslinks and an overall higher Young's modulus. Additionally, tuning the curing temperature impacts the final modulus (lower curing temperatures lead to lower moduli). While Dow Corning indicates that PDMS cures quickly (minutes to hours, depending on curing temperature), the crosslinking reaction is a kinetic process which slows but continues for a number of days (Figure A.3). The final modulus can be nearly twice that of the soft-cured material, leading to varying performance and properties if the same material is used experimentally over the course of several days.

Finally, it is important to note the limitations of the Dow Sylgard 184 system. While ubiquitous in materials science experiments, Sylgard is a commercial product produced at the industrial scale. Debris and other artifacts inherent to the production of the base and curing agent can always be present. Another result of being a commercial product is that the exact nature of the chemistry is proprietary and therefore unknown. Also, as with most crosslinking reactions, the mobility of chain ends decreases as crosslinking increases, resulting in free chains that are not chemically connected to the PDMS network.[107] These unreacted free chains are mobile within the network and have been shown to "bloom" or migrate to the surface of the elastomer, which can significantly impact surface property studies of friction and adhesion.[67,108,109] Extractions of the crosslinked network through swelling in a good solvent can remove much of these oils or free chains. Sylgard has also been reported to contain a large quantity of silica

particles.[42] The size, shape, and surface properties of these particles are unknown but their presence should be noted.

BIBLIOGRAPHY

1. Al Bitar L, Voigt D, Zebitz CPW, Gorb SN. Tarsal morphology and attachment ability of the codling moth Cydia pomonella L. (Lepidoptera, Tortricidae) to smooth surfaces. *Journal of insect physiology*. 2009;55(11):1029-38.

2. Haas F, Gorb SN. Evolution of locomotory attachment pads in the Dermaptera (Insecta). *Arthropod structure & development*. 2004;33(1):45-66.

3. Kücken M, Newell A. Fingerprint formation. *Journal of Theoretical Biology*. 2005;235:71-83.

4. Warman PH, Ennos a R. Fingerprints are unlikely to increase the friction of primate fingerpads. *The Journal of experimental biology*. 2009;212(Pt 13):2016-22.

5. André T, Lefèvre P, Thonnard J-L. Fingertip moisture is optimally modulated during object manipulation. *Journal of neurophysiology*. 2010;103(1):402-8.

6. André T, Lévesque V, Hayward V, Lefèvre P, Thonnard J-L. Effect of skin hydration on the dynamics of fingertip gripping contact. *Journal of the Royal Society, Interface*. 2011.

7. Genzer J, Groenewold J. Soft matter with hard skin: From skin wrinkles to templating and material characterization. *Soft Matter*. 2006;2(4):310–323.

8. Huck WTS, Bowden N, Onck P, et al. Ordering of spontaneously formed buckles on planar surfaces. *Langmuir*. 2000;16(7):3497–3501.

9. Vandeparre H, Damman P. Wrinkling of stimuloresponsive surfaces: mechanical instability coupled to diffusion. *Physical Review Letters*. 2008;101(12):1-4.

10. Timoshenko S. *Theory of Plates and Shells*. McGraw-Hill; 1964.

11. Bowden N, Huck WTS, Whitesides GM, Paul KE. The controlled formation of ordered, sinusoidal structures by plasma oxidation of an elastomeric polymer. *Applied Physics Letters*. 2001;75(17):2557-2559.

12. Breid D, Crosby AJ. Effect of stress state on wrinkle morphology. *Soft Matter*. 2011;7(9):4490.

13. Breid D, Crosby AJ. Surface wrinkling behavior of finite circular plates. *Soft Matter*. 2009;5(2):425.

14. Allen HG. *Analysis and design of structural sandwich panels*. Pergamon press Oxford; 1969.

15. Groenewold J. Wrinkling of plates coupled with soft elastic media. *Physica A: Statistical Mechanics and its Applications*. 2001;298(1-2):32-45.

16. Bowden N, Brittain S, Evans A, Hutchinson JW, Whitesides GM. Spontaneous formation of ordered structures in thin films of metals supported on an elastomeric polymer. *Nature*. 1998;393:146-149.

17. Stafford CM, Harrison C, Beers KL, et al. A buckling-based metrology for measuring the elastic moduli of polymeric thin films. *Nature materials*. 2004;3(8):545550.

18. Chen X, Hutchinson JW. Herringbone Buckling Patterns of Compressed Thin Films on Compliant Substrates. *Journal of Applied Mechanics*. 2004;71(5):597.

19. Yang S, Khare K, Lin P-C. Harnessing surface wrinkle patterns in soft matter. *Advanced Functional Materials*. 2010;20(16):2550-2564.

20. Rand CJ, Sweeney R, Morrissey M, Hazel L, Crosby AJ. Fracture-induced alignment of surface wrinkles. *Soft Matter*. 2008;4(9):1805.

21. Lee J-Y, Crosby AJ. Crazing in Glassy Block Copolymer Thin Films. *Macromolecules*. 2005;38(23):9711-9717.

22. Harrison C, Stafford CM, Zhang W, Karim A. Sinusoidal phase grating created by a tunably buckled surface. *Applied Physics Letters*. 2004;85(18):4016–4018.

23. Chan EP, Smith EJ, Hayward RC, Crosby AJ. Surface wrinkles for smart adhesion. *Advanced Materials*. 2008;20(4):711-716.

24. Tanaka T, Sun S, Hirokawa Y, et al. Mechanical instability of gels at the phase transition. *Nature*. 1987;325(26):796-798.

25. Chan EP, Crosby AJ. Spontaneous formation of stable aligned wrinkling patterns. *Soft Matter*. 2006;2(4):324.

26. Miquelard-Garnier G, Croll AB, Davis CS, Crosby AJ. Contact-line mechanics for pattern control. *Soft Matter*. 2010;6(22):5789-5794.

27. Cai S, Breid D, Crosby AJ, Suo Z, Hutchinson JW. Periodic patterns and energy states of buckled films on compliant substrates. *Journal of the Mechanics and Physics of Solids*. 2011;59(5):1094-1114.

28. Chan EP, Kundu S, Lin Q, Stafford CM. Quantifying the stress relaxation modulus of polymer thin films via thermal wrinkling. *ACS applied materials & interfaces*. 2011;3(2):331-8.

29. Chan EP, Page K a., Im SH, et al. Viscoelastic properties of confined polymer films measured via thermal wrinkling. *Soft Matter*. 2009;5(23):4638.

30. Lin P-C, Vajpayee S, Jagota A, Hui C-Y, Yang S. Mechanically tunable dry adhesive from wrinkled elastomers. *Soft Matter*. 2008;4(9):1830.

31. Ohzono T, Shimomura M. Geometry-dependent stripe rearrangement processes induced by strain on preordered microwrinkle patterns. *Langmuir*. 2005;21(16):7230-7.

32. Chiche A, Stafford CM, Cabral JT. Complex micropatterning of periodic structures on elastomeric surfaces. *Soft Matter*. 2008;4(12):2360.

33. Ohzono T, Shimomura M. Defect-mediated stripe reordering in wrinkles upon gradual changes in compression direction. *Physical Review E*. 2006;73(4):2-5.

34. Hui C-Y, Lin YY, Creton C. Bonding of a viscoelastic periodic rough surface to a rigid layer. *Journal of Polymer Science Part B: Polymer Physics*. 2002;40(6):545-561.

35. Hui C-Y, Lin YY, Baney J, Kramer EJ. The mechanics of contact and adhesion of periodically rough surfaces. *Journal of Polymer Science Part B: Polymer Physics*. 2001;39(11):11951214.

36. Johnson K. The adhesion of two elastic bodies with slightly wavy surfaces. *International Journal of Solids and Structures*. 1995;32(3):423430.

37. Johnson K, Greenwood J, Higginson J. The contact of elastic regular wavy surfaces. *International Journal of Mechanical Sciences*. 1985;27(6):383–396.

38. Westergaard H. Bearing pressures and cracks. *SPIE Milestone Series MS*. 1939;137:18–22.

39. Waters J, Lee S, Guduru P. Mechanics of axisymmetric wavy surface adhesion: JKR–DMT transition solution. *International Journal of Solids and Structures*. 2009;46(5):1033-1042.

40. Kundu S, Davis CS, Long T, Sharma R, Crosby AJ. Adhesion of nonplanar wrinkled surfaces. *Journal of Polymer Science Part B: Polymer Physics*. 2011;49(3):179-185.

41. Jin C, Khare K, Vajpayee S, et al. Adhesive contact between a rippled elastic surface and a rigid spherical indenter: from partial to full contact. *Soft Matter*. 2011.

42. Efimenko K, Wallace WE, Genzer J. Surface modifcation of Sylgard-184 poly(dimethyl siloxane) networks by ultraviolet and ultraviolet/ozone treatment. *Journal of Colloid and Interface Science*. 2002;254:306-315.

43. Hertz H. *The Principles of Mechanics*. New York, NY: Macmillan and Co., Ltd. 1896.

44. Johnson K. *Contact Mechanics*. 1st ed. Cambridge University Press; 1987.

45. Barquins M. Adherence and rolling kinetics of a rigid cylinder in contact with a natural-rubber surface. *Journal of Adhesion*. 1988;26(1):1-12.

46. Barquins M, Charmet J-C, Robbe-Valloire F. Adhesive contact and kinetics of adherence between a rigid cylinder and a soft elastomeric solid. *Comptes Rendus de l'Académie des Sciences - Series IV - Physics*. 1998;326(2):575-585.

47. Chaudhury MK, Weaver T, Ito S, Kramer EJ. Adhesive contact of cylindrical lens and a flat sheet. *Journal of Applied Physics*. 1996;80(1):30.

48. She H, Malotky D, Chaudhury MK. Estimation of adhesion hysteresis at polymer/oxide interfaces using rolling contact mechanics. *Langmuir*. 1998;14(11):3090-3100.

49. Takahashi Y. Adhesional bonding of fine gold wires to metal substrates. *Journal of Adhesion Science and Technology*. 2003;17(3):435-451.

50. Xie H, Lambert P, Régnier S. Analysis of nanoscale mechanical grasping under ambient conditions. *Journal of Micromechanics and Microengineering*. 2011;21(4):045009.

51. Ong Y-L, Razatos A, Georgiou G, Sharma MM. Adhesion forces between E. coli bacteria and biomaterial surfaces. *Langmuir*. 1999;(15):2719-2725.

52. Shull KR. Contact mechanics and the adhesion of soft solids. *Materials Science and Engineering: R: Reports*. 2002;36(1):1-45.

53. Maugis D, Barquins M. Fracture mechanics and the adherence of viscoelastic bodies. *Journal of Physics D: Applied Physics*. 1978;11:1989–2023.

54. Deruelle M, Léger L, Tirrell M. Adhesion at the solid-elastomer interface: influence of the interfacial chains. *Macromolecules*. 1995;28(22):7419-7428.

55. Davis CS, Crosby AJ. Mechanics of wrinkled surface adhesion. *Soft Matter*. 2011;7:5373-5381.

56. Johnson K, Kendall K, Roberts A. Surface energy and the contact of elastic solids. *Proceedings of the Royal Society of London. Series A, Mathematical and Physical Sciences*. 1971;324(1558):301-313.

57. Sümer B, Onal CD, Aksak B, Sitti M. An experimental analysis of elliptical adhesive contact. *Journal of Applied Physics*. 2010;107(11):113512.

58. Sundaram N, Chandrasekar S. Shape and eccentricity effects in adhesive contacts of rodlike particles. *Langmuir*. 2011;27(20):12405-10.

59. Autumn K, Liang Y a, Hsieh ST, et al. Adhesive force of a single gecko foot-hair. *Nature*. 2000;405(6787):681-5.

60. Arzt E, Gorb SN, Spolenak R. From micro to nano contacts in biological attachment devices. *Proceedings of the National Academy of Sciences*. 2003;100(19):10603-10606.

61. Barthlott W, Neinhuis C. Purity of the sacred lotus, or escape from contamination in biological surfaces. *Planta*. 1997;202(1):1-8.

62. Reddy S, Arzt E, Campo A del. Bioinspired Surfaces with Switchable Adhesion. *Advanced Materials*. 2007;19(22):3833-3837.

63. Aksak B, Murphy MP, Sitti M. Adhesion of biologically inspired vertical and angled polymer microfiber arrays. *Langmuir*. 2007;23(6):3322-32.

64. Aksak B, Sitti M, Cassell A, et al. Friction of partially embedded vertically aligned carbon nanofibers inside elastomers. *Applied Physics Letters*. 2007;91(6):061906.

65. Qu L, Dai L. Gecko-foot-mimetic aligned single-walled carbon nanotube dry adhesives with unique electrical and thermal properties. *Advanced Materials*. 2007;19(22):3844-3849.

66. Jeong HE, Kwak MK, Suh K-Y. Stretchable, adhesion-tunable dry adhesive by surface wrinkling. *Langmuir*. 2010;26(4):2223-6.

67. Rand CJ, Crosby AJ. Friction of soft elastomeric wrinkled surfaces. *Journal of Applied Physics*. 2009;106(6):064913.

68. Tirrell M. Measurement of interfacial energy at solid polymer surfaces. *Langmuir*. 1996;12(19):4548-4551.

69. Maugis D. *Contact, Adhesion and Rupture of Elastic Solids*. Berlin: Springer-Verlag; 2000.

70. Mangipudi VS, Huang E, Tirrell M. Measurement of interfacial adhesion between glassy polymers using the JKR method. *Macromolecular Symposia*. 1996;102:131-143.

71. McGuiggan PM, Wallace JS, Smith DT, et al. Contact mechanics of layered elastic materials: experiment and theory. *Journal of Physics D: Applied Physics*. 2007;40(19):5984-5994.

72. Perriot A, Barthel E. Elastic contact to a coated half-space-Effective elastic modulus and real penetration. *Journal of Materials Research*. 2004;19:600–608.

73. Johnson K, Sridhar I. Adhesion between a spherical indenter and an elastic solid with a compliant elastic coating. *Journal of Physics D: Applied Physics*. 2001;34:683-689.

74. Crosby AJ, Shull KR, Lakrout H, Creton C. Deformation and failure modes of adhesively bonded elastic layers. *Journal of Applied Physics*. 2000;88(5):2956.

75. Briggs G, Briscoe B. Effect of surface roughness on rolling friction and adhesion between elastic solids. *Nature*. 1976;260:313-315.

76. Fuller KNG, Tabor D. The effect of surface roughness on the adhesion of elastic solids. *Proceedings of the Royal Society of London. Series A, Mathematical and Physical Sciences*. 1975;345(1642):327-342.

77. Persson BNJ, Tosatti E. The effect of surface roughness on the adhesion of elastic solids. *The Journal of Chemical Physics*. 2001;115(12):5597.

78. Hui C-Y, Lin YY, Baney J. The mechanics of tack: Viscoelastic contact on a rough surface. *Journal of Polymer Science Part B: Polymer Physics*. 2000;38(11):1485-1495.

79. Lakrout H, Sergot P, Creton C. Direct observation of cavitation and fibrillation in a probe tack experiment on model acrylic pressure-sensitive-adhesives. *Journal of Adhesion*. 1999;69:307-359.

80. Bartlett MD, Croll AB, King DR, et al. Looking beyond fibrillar features to scale Gecko-like adhesion. *Advanced Materials*. 2012.

81. Hui C-Y, Baney J, Kramer EJ. Contact mechanics and adhesion of viscoelastic spheres. *Langmuir*. 1998;14(22):6570-6578.

82. Nase J, Creton C, Ramos O, et al. Measurement of the receding contact angle at the interface between a viscoelastic material and a rigid surface. *Soft Matter*. 2010;6(12):2685.

83. Crosby AJ, Hageman M, Duncan AJ. Controlling polymer adhesion with "Pancakes." *Langmuir*. 2005;21(25):11738–11743.

84. Chan EP, Arzt E, Greiner C, Crosby AJ. Designing model systems for enhanced adhesion. *MRS Bulletin*. 2007;32:496-503.

85. Souza EJ De, Gao L, McCarthy TJ, Arzt E, Crosby AJ. Effect of contact angle hysteresis on the measurement of capillary forces. *Langmuir*. 2008;24(4):1391-6.

86. Nase J. Debonding of viscoelastic materials : from a viscous liquid to a soft elastic solid. *Dissertation*. 2009.

87. Chiche A, Pareige P, Creton C. Role of surface roughness in controlling the adhesion of a soft adhesive on a hard surface. *Comptes Rendus de l'Académie des Sciences - Series IV - Physics*. 2000;1(9):1197-1204.

88. Shull KR, Creton C. Deformation behavior of thin, compliant layers under tensile loading conditions. *Journal of Polymer Science Part B: Polymer Physics*. 2004;42:4023- 4043.

89. Crosby AJ, Shull KR, Lin YY. Rheological properties and adhesive failure of thin viscoelastic layers. *Journal of Rheology*. 2002:273-294.

90. Fabbroni EF, Shull KR, Hersam MC. Adhesive and mechanical properties of soft nanocomposites: Model studies with blended latex films. *Journal of Polymer Science Part B: Polymer Physics*. 2001;39(24):3090–3102.

91. Yin J, Cao Z, Li C, Sheinman I, Chen X. Stress-driven buckling patterns in spheroidal core/shell structures. *Proceedings of the National Academy of Sciences*. 2008;105(49):19132-5.

92. Kim HS, Crosby AJ. Solvent-responsive surface via wrinkling instability. *Advanced Materials*. 2011;23:4188-4192.

93. Uchida N, Ohzono T. Orientational ordering of buckling-induced microwrinkles on soft substrates. *Soft Matter*. 2010;6(22):5729.

94. Bechert DW, Bruse M, Hage W. Experiments with three-dimensional riblets as an idealized model of shark skin. *Experiments in Fluids*. 2000;28(5):403-412.

95. Cheng Y, Rodak D, Wong C, Hayden C. Effects of micro-and nano-structures on the self-cleaning behaviour of lotus leaves. *Nanotechnology*. 2006;17:1359–1362.

96. Ko D-H, Tumbleston JR, Henderson KJ, et al. Biomimetic microlens array with antireflective "moth-eye" surface. *Soft Matter*. 2011:10-13.

97. Pocivavsek L, Dellsy R, Kern A, et al. Stress and fold localization in thin elastic membranes. *Science*. 2008;320(5878):912-916.

98. Singamaneni S, Mcconney ME, Tsukruk VV. Spontaneous self-folding in confined ultrathin polymer gels. *Advanced Materials*. 2010;22:1263-1268.

99. Efimenko K, Finlay J, Callow ME, Callow JA, Genzer J. Development and testing of hierarchically wrinkled coatings for marine antifouling. *Applied Materials & Interfaces*. 2009;1(5):1031-1040.

100. Whitesides GM. The origins and the future of microfluidics. *Nature*. 2006;442(7101):368-73.

101. Corning D. Information about high technology silicone materials. *Dow Corning Corporation*. 1991.

102. Campbell DJ, Beckman KJ, Calderon CE, et al. Replication and compression of bulk and surface structures with polydimethylsiloxane elastomer. *Journal of Chemical Education*. 1999;75(4):537-541.

103. Sakaki S, Mizoe N, Sugimoto M. Theoretical study of Platinum(0)-catalyzed hydrosilylation of ethylene: Chalk-Harrod mechanism or modified Chalk-Harrod mechanism. *Organometallics*. 1998;17:2510-2523.

104. Antic VV, Antic MP, Govedarica MN, Dvornic PR. Kinetics and mechanism of the formation of poly [(1,1,3,3-tetramethyldisiloxanyl)ethylene] and poly(methyldecylsiloxane) by hydrosilylation. *Journal of Polymer Science Part A: Polymer Chemistry*. 2007;45:2246-2258.

105. Chalk AJ, Harrod JF. Homogeneous catalysis. II. The mechanism of the hydrosilation of olefins catalyzed by group VI11 metal complexes. *Journal of the American Chemical Society*. 1965;87(1):16-21.

106. Eddington DT, Crone WC, Beebe DJ. Development of process protocols to fine tune polydimethylsiloxane material properties. In: *7th International Conference on Miniaturized Chemical and Biochemical Analysis Systems, Squaw Valley, California, USA*.; 2003:1089–1092.

107. Kroner E, Maboudian R, Arzt E. Effect of repeated contact on adhesion measurements involving polydimethylsiloxane structural material. *IOP Conference Series: Materials Science and Engineering*. 2009;5:012004.

108. Rand CJ, Crosby AJ. Friction of soft elastomeric surfaces with a defect. *Applied Physics Letters*. 2007;91(26):261909.

109. Rand CJ, Crosby AJ. Insight into the periodicity of Schallamach waves in soft material friction. *Applied Physics Letters*. 2006;89(26):261907.